Etude de la stabilisation par du PVA de solutions aqueuses de graphène et de graphène oxydé et caractérisation des performances du composite graphène/graphène oxydé - PVA

Ying Huo

Nºd' ordre NNT : 2021LYSEC07

THESE de DOCTOCAT DE L'UNIVERSITE DE LYON
opéréé au sein de l'Ecole centrale de Lyon

Ecole Doctorale Nº 34
Ecole Doctorale Matériaux de Lyon

Spécialité/ Discipline de Doctorat : Matériaux

Soutenue publiquement le 30/03/2021, par :

Ying HUO

Study of the mechanism of graphene and graphene oxide stabilized by PVA in water media and the performance of graphene (and graphene oxide)/PVA composite materials

Étude de la stabilisation par du PVA de solutions aqueuses de graphène et de graphène oxydé et caractérisation des performances du composites graphène/graphène oxydé - PVA

Composition du jury:

Jiang Xuchuan	A. Professor, Department of Chemical Engineering, Monash University	Rapporteur
Zakri Cécile	Professeure, CRPP, Université de Bordeaux	Rapporteure
Brousse Thierry	Professeur, IMN, Université de Nantes	Examinateur
Cloarec Jean-Pierre	Professeur, INL, Ecole Centrale de Lyon	Examinateur President
Benayoun Stéphane	Professeur, LTDS, Ecole Centrale de Lyon	Directeur de thèse
Toury Bérangère	Maître de Conférences-HDR, LMI, Université Claude Bernard Lyon 1	Co-directrice de thèse
Yuan Sheng	Maître de Conférences, MateIS, INSA de Lyon	Co-encadrant de thèse
Normand Bernard	Professeur, MateIS, INSA de Lyon	Invité

To my beloved parents, husband and my friends

Acknowledgement

Contents

General introduction

As an allotrope of carbon consisting of a single layer of atoms arranged in a two-dimensional honeycomb lattice, graphene has generated intense interest thanks to its unprecedented physical properties. In the past decade, graphene has been studied in various application fields from energy storage to biotechnology. Some important application classes such as conductive coating, printed electronics, and composite fillers generally require large-scale and low-cost production of graphene in a processable form. For instance, several electrode materials applied in solar cell, batteries, and electrochemical capacitors can be prepared starting from large quantities of graphene dispersed in liquid media. Thus, liquid-phase exfoliation (LPE) becomes one of the most important techniques to produce graphene for next processing.

LPE involves an exfoliation of atomic layers from its bulk form using ultrasonic treatment or high shear mixing in appropriate solvents. The choice of the solvent closely depends on the interaction between graphene and solvent, which should lead to exfoliated nanosheets at a relatively high concentration while maintaining the colloidal stability. In the literatures, interactions between graphene and solvent are reported to be dependent of their solubility parameters, in particular, the Hildebrand solubility parameters for non-polar solvents and the Hansen solubility parameters for polar solvents like pure water. A higher graphene concentration is obtained by choosing close solubility parameters between graphene and solvent. Based on this principle, appropriate solvents are strictly organic meaning commonly harmful to environment and difficult to be removed. Water is a more viable option, however, direct exfoliation of graphene in pure water is barely possible because of its highly symmetric structure leading to a hydrophobic behavior.

To circumvent this issue, in this thesis, two main routes has been studied: *i*. LPE of raw graphite to produce pristine graphene aqueous dispersion with assistance of a polymer as stabilizer that interact noncovalently with graphene and prevent nanosheets' stacking and *ii*. graphite oxidation followed by LPE to yield graphene oxide that contains oxygen-based functional groups along the basal plane and edges and can be dispersed in water at a high concentration. In addition, incorporating polymer, GO can produce a strong interaction with polymer molecules in solution to avoid undesired nanosheets' agglomeration in next processing. Therefore, by using the obtained stable colloids, a series of GO/ polymer composites have been processed, which were studied in application as electrode materials of electrochemical capacitor.

In this thesis, Polyvinyl Alcohol (PVA) was used as a stabilizer thank to its low-cost, biocompatibility, transparency, flexibility, aqueous solubility, and ease of processing. All the specific contents mentioned above will be discussed through five chapters:

Chapter 1 introduces a bibliographic investigation, highlighting the origin, production, properties, and applications of graphene. Through this review, we have compared the different production techniques of graphene, among which liquid-phase exfoliation is illustrated in detail due to its safety, low cost, and large scale-up potential. In addition, graphene-polymer system applied in electrode materials of electrochemical capacitor is also presented. Finally, several electrochemical characterization means are introduced.

In chapter 2, we have gathered all specific experimental methods that we have carried out within this thesis, including preparation of samples, introduction of materials and equipment, characterization techniques, and electrochemical measurements.

Chapter 3 mainly investigates PVA-assisted pristine graphene dispersion in water. Different concentrations of PVA solution are used to disperse pristine graphene, aiming to obtain the highest concentration of graphene stabilized with the lowest concentration of PVA. The corresponding mechanism of polymer-assisted graphene dispersing via physisorption will be studied carefully.

In Chapter 4, since GO is typically defective, tailoring the oxygen content on graphene is a way to optimize graphene properties and dispersibility. Thus, graphite oxides with different oxidation degree are prepared. Because of hydrogen bonds forming, the effect of different oxidation degree on graphene dispersed in PVA/water solution will be discussed.

In the last chapter, a case based on the use of GO/polymer mixture to realize sample processing is explored. By directly using the GO/PVA/water mixtures obtained in chapter 4, a series of PVA/GO hybrid aerogels with different PVA contents are fabricated using a freeze-drying method. The resultant hybrid aerogels applied as electrode materials of electrochemical capacitor will be investigated.

Chapter 1

Introduction

In this chapter, graphene as the most popular two-dimensional material will be introduced in the basic aspects including its origin, oxidation states, structure, properties and applications. Among conventional production techniques of graphene, liquid-phase exfoliation (LPE) strategies are very interesting and will be carefully illustrated. Moreover, two ways used to increase graphene dispersibility in aqueous solution, including exfoliation of raw graphite with assistance of polymer stabilizers and exfoliation of graphite oxide into graphene oxide, will be highlighted. Furthermore, mechanism of graphene dispersion in two-phase and three-phase systems will be discussed in detail. In addition, we will report fabrication ways of graphene/ polymer nanocomposites, and their application in electrochemical capacitor's electrode material. In the end, three electrochemical characterization methods for electrochemical capacitor, including Cyclic Voltammetry (CV), Galvanostatic Charge/Discharge (GCD), and Electrochemical Impedance Spectroscopy (EIS), will be introduced.

1.1 Introduction of Graphene

1.1.1 From carbon to Graphene

Carbon is widely dispersed in nature. The chemical element with C as symbol has a ground-state electron configuration of $1s^2 2s^2 2p^2$, the four outer electrons are available to form covalent chemical bonds. There are different ways to bond two neighboring C atoms resulting in various allotropic forms, further resulting in different materials. Figure 1.1 shows the best-known allotropes: graphite and diamond.[1]
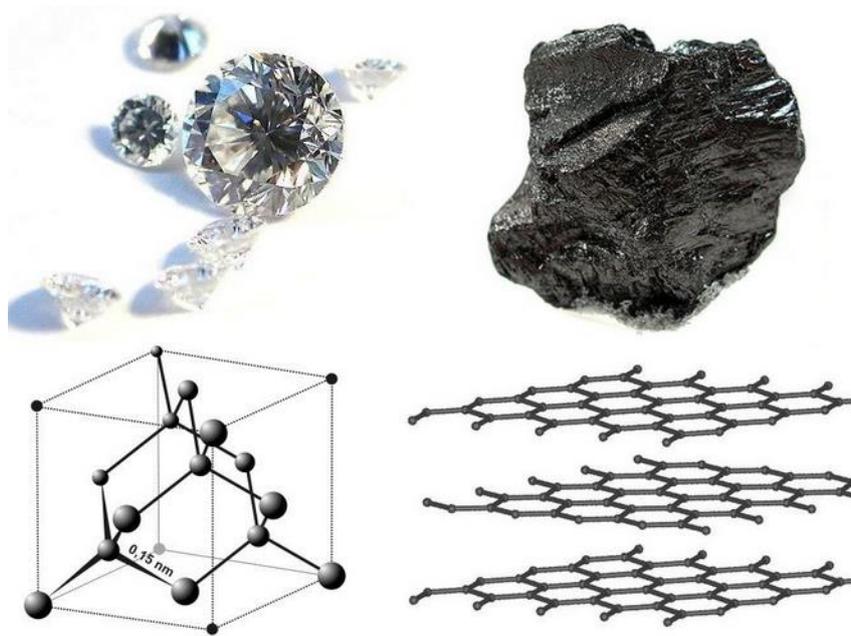
Figure 1.1 | Photograph of diamond and graphite, and their crystalline structures.[2]

In graphite, unlike in diamond which has sp^3 carbon bonding, the carbon bonding involves sp^2 hybridization, and atoms are arranged in a hexagonal pattern which is stretching to the layer structure. (see Figure 1.1) The three of four electrons around C atoms are bonded covalently, and the fourth freely migrates in the plane. Moreover, there are Van der Waals forces between layers that link them to each other. Because, graphite is anisotropic, it displays good electrical and thermal conductivity within the layers that become low perpendicularly to the layers.[3] Similarly, the strength and modulus within the layers are much higher than those in perpendicular due to the different types of bonds in this two directions.[4]

Graphene is a monolayer of graphite. In 1947, a series of theoretical studies reported that an extraordinary electrical conductivity could be exhibited in isolated graphene layers.[5] However, planar graphene always has been considered not to exist stably in the free state.[6–8] In 2004, Andre Geim and co-workers firstly made the graphite sheets with a few atomic layers, including monolayer graphene by using the "scotch-tape" technique (repeated peeling of graphite using tape).[9] It is a revolutionary discovery to trigger a series of new studies in the fields of chemistry, physics, biology and materials. As displayed in Figure 1.2, the number of publications on graphene has dramatically raised from 2000 to 2017.[10] Andre Geim and Konstantin Novoselov were awarded the 2010 Nobel Prize in Physics for this discovery.
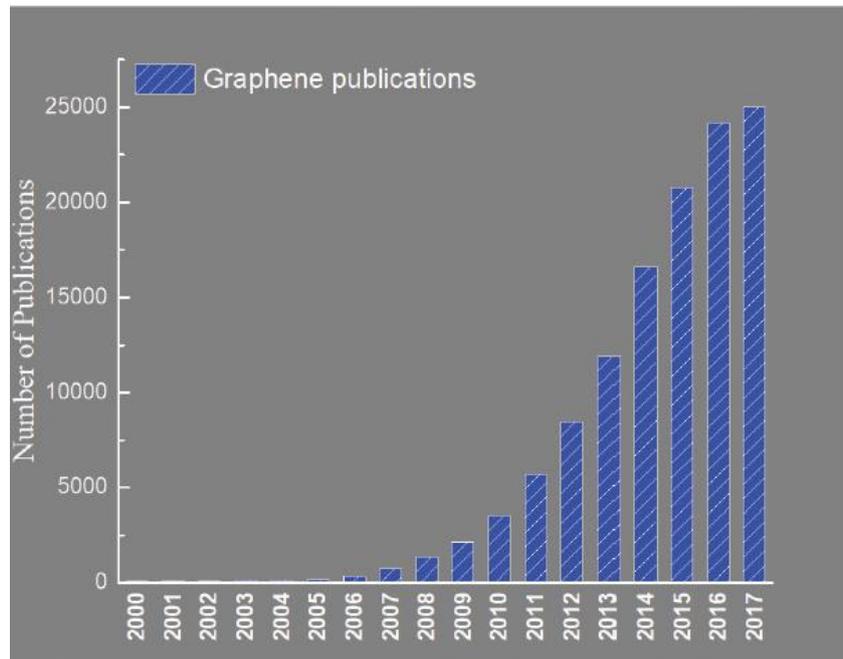
Figure 1.2 | Publications on Graphene from 2000 to 2017. (Source: ISI web of science by searching the topic of Graphene)[10]

Based on the atomic structure features, graphene is considered as a two-dimension (2D) material for the build of zero- dimension (0D) fullerenes, one-dimension (1D) nanotubes and three-dimension (3D) graphite. [11] (see Figure 1.3) To be specific, firstly, Fullerene is obtained by bending a part of graphene into a football shape. It is composed of 60 carbon atoms connected by 20 six-membered rings and 12 five-membered rings. It has 30 carbon-carbon double bonds (C=C). Secondly Carbon Nanotube can be regarded as a part of graphene sheet curled, and both ends are sealed by half of fullerene. In addition to the sp^2 hybridization, the carbon atoms in the carbon nanotubes are partially sp^3 hybridized, so that they can present a curved tubular structure. Finally, as described before, Graphite is made up of multiple layers of graphene, and it has a looser structure between layers.

9
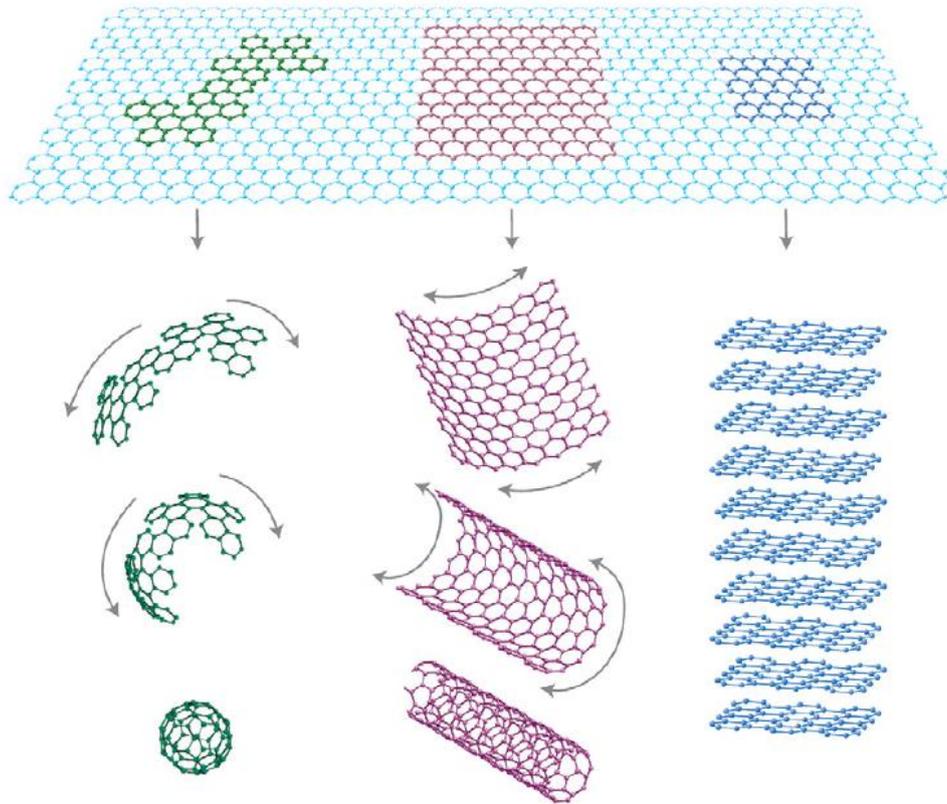
Figure 1.3 | Based on the atomic structure features, graphene is considered as a 2D material for the build of 0D fullerenes, 1D nanotubes and 3D graphite.[11]

1.1.2 Graphene-based nanosheets

Graphene oxide (GO) is a monolayer of graphite oxide that corresponds to a chemical functionalization of graphite. About 150 years ago, graphite oxide was prepared by Brodie, [12,13] then derived methods were proposed by Staudenmaier [13,14] and Hummers [15]. In their methods, $KMnO_4$, $KClO$, and $NaNO_2$ as strong oxidants were used to oxidize graphite in HNO_3 or HNO_3 and H_2SO_4 mixture. So far, modified Hummers methods are widely used to prepare graphite oxide. [16–18] For instance, $KMnO_4$ is used as oxidant agent in H_2SO_4:H_3PO_4 mixture with a ratio of 9:1. Unlike pristine graphite, that is difficult to transform into few- or single-layer graphene, graphite oxide with active functional site can be easily exfoliated to GO and has better solubilities in organic solvent or water. [11] Those functional groups including epoxide groups, carbonyl, hydroxyl, and phenol groups are exposed on the surface and the edges of GO, inducing more sp^3 hybridization on it. [19,20] This loss of sp^2 configuration of the intrinsic

graphene changes its physical and chemical properties. [21] For example, GO has a low electrical conductivity, even becomes an insulator. [22]

By using thermal or chemical reduction of GO, the structure of pristine graphene and its unique properties can be recovered partially. [20,23,24] Thereby, the reduced graphene oxide (rGO) is an intermediate product between ideal graphene and completely oxidized GO. The structures of the graphene-based nanosheets (GNS) involving pristine graphene, graphene oxide and reduced graphene oxide are shown Figure 1.4.
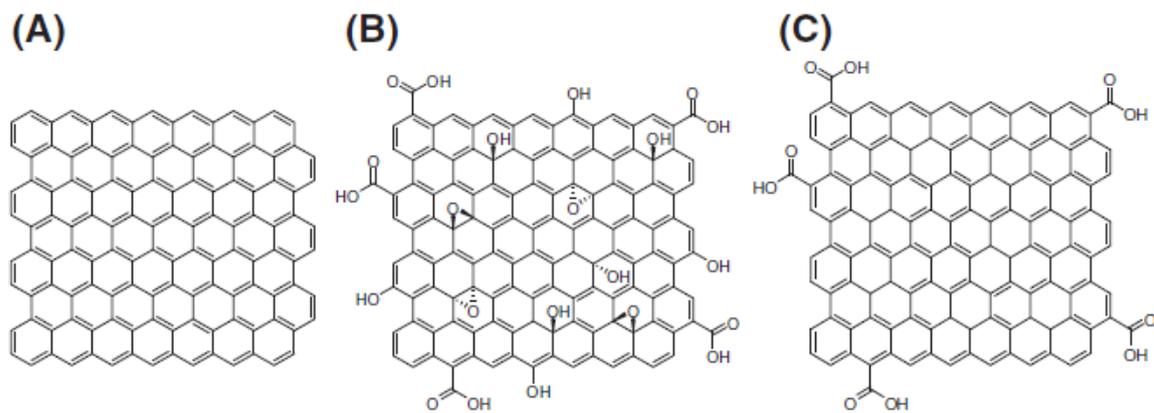
Figure 1.4 | Structure of (**A**) graphene, [25] (**B**) graphene oxide (GO) [26] and (**C**) reduced graphene oxide (rGO) [20,27]

1.1.3 Properties of Graphene-based nanosheets

The honeycomb crystal graphene as a one-atom-thick planar layer composed of sp^2 bonded carbon atoms, presents an unique combination of properties not seen in other carbon allotropes. [28,29] Graphene is the thinnest and strongest materials, actually, the free-standing monolayer graphene exhibits a Young's modulus of 1.0 TPa and a fracture strength of 130 GPa, measured by nanoindentation using Atomic Force Microscope (AFM). [30]

Graphene possesses extraordinary performances because of its high charge carrier mobility (μ). The conductivity of a suspended-graphene (SG) with a single layer has a value of $\mu > 2.30 \times 10^5$ cm^2 V^{-1} s^{-1}, which exceed that of other materials. [31] Furthermore, ultraclean suspended graphene with single layer has an ultrahigh value of μ up to 3.8×10^5 cm^2 V^{-1} s^{-1}. [32] (see Figure 1.5)
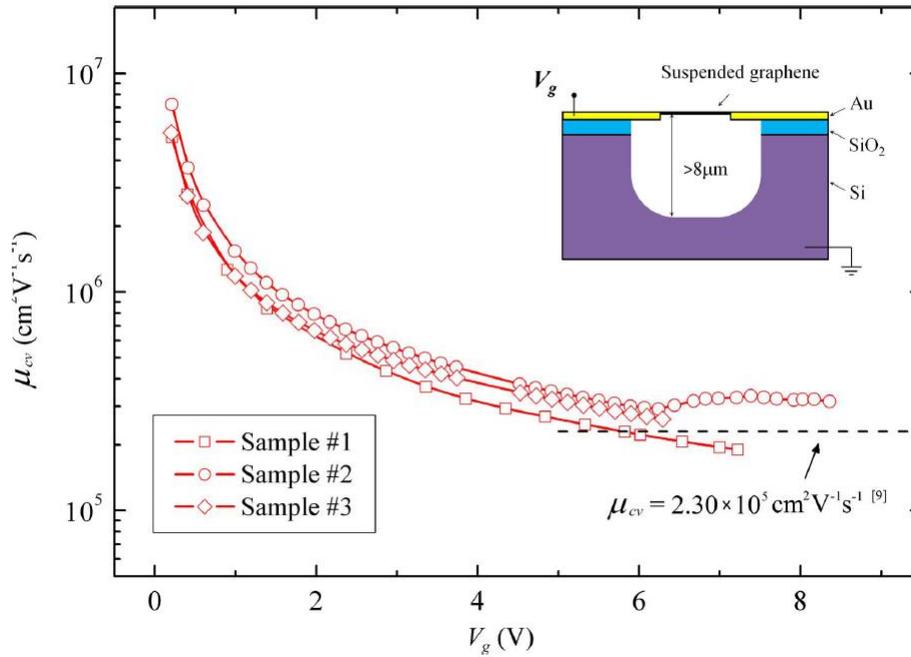
Figure 1.5 | Charge carrier mobility (μ) of the current-cleaned SG with sample as a function of the gate voltage. The dashed black line is a high value of μ of a conventional SG. The symbol lines represent the charge carrier mobility of the current-cleaned SG. Insight image is the side view of device schematic representation for the SG. [32]

Graphene also displays a high thermal conductivity (κ). $\kappa = \sim 6000$ Wm^{-1}K^{-1} for a monolayer graphene at room temperature (RT) was computationally predicted, [33] and $\kappa = \sim 5300$ Wm^{-1}K^{-1} of a suspended monolayer graphene at RT was experimentally measured. [34]

Besides, graphene presents other great properties, such as a high surface area (~ 2630 m^2 g^{-1}) [35] and a good optical absorption of $\pi\alpha = \sim 2.3\%$. [36] Moreover it is impermeable to standard gases. [37]

It should be noticed that some of these extraordinary properties of graphene are only achieved for the high-quality and few-layer samples prepared by mechanical exfoliation or measured after very elaborate handling. For example, graphene's electrical properties extremely depend on the number of graphene layers, thereby, the graphene families are distinguished into monolayer graphene and bilayer or few-layer graphene. Graphene with more than 10 layers exhibit the electrical properties of graphite. [38]

Graphite oxide is obtained by chemical oxidation of graphite, the introduction of oxygen-based functional groups on the graphene surface not only allows to expand the layers, but also permits to render it more hydrophilic and easily exfoliable into single layer or few-layer graphene oxide (GO) by using some polar solvents such as an aqueous solution. [17] In addition, GO has excellent design flexibility. The oxygen-based groups on GO nanosheets can be active sites to react with various functional groups to produce linkages or to form strong molecular interactions like hydrogen bonds with some polymers. [39–41] The functionalization of GO can change its properties, and consequently its application fields. For instance, GO can be applied to remove radioactive ions from water for disposal. [42] The rGO can also be functionalized by a chemical way, which also open new routes for incorporation of layer materials in other matrices to extend their applications.

1.1.4 Applications of Graphene-based nanosheets

As described in the last section, Graphene-based nanosheets possess remarkable properties that can provide infinite possibilities in various application fields such as energy storage, conductivity materials, catalytic reactions, biotechnology and *etc.* [43] Specifically, they can be extensively applied as electroactive materials in electrochemical capacitors' electrodes thanks to their large surface-to-volume ratio and the high content of oxygen-containing functional groups. [44–46] Graphene-based nanosheets are also good candidate to develop different sensors. [47] For instance, GO-based biological sensors can be used to detect tumorous cells through attaching to the surface molecules containing antibodies. [48] In addition, thanks to its layered structure, Graphene-based nanosheets display impermeability and can be used for protective coatings production. [49,50] When Graphene is directly grown on metal, it can act as a passive layer with excellent corrosion resistance. Furthermore, used as fillers charge into polymer matrix, GO or rGO can enhance the anti-corrosion properties of the resulting polymer coating. [51–54] Besides, being conductive and transparent, Graphene-based nanosheets could replace indium-based electrodes used in touchscreens. [55] Figure 1.6 shows more examples of potential applications of Graphene-based nanosheets. [55,56]
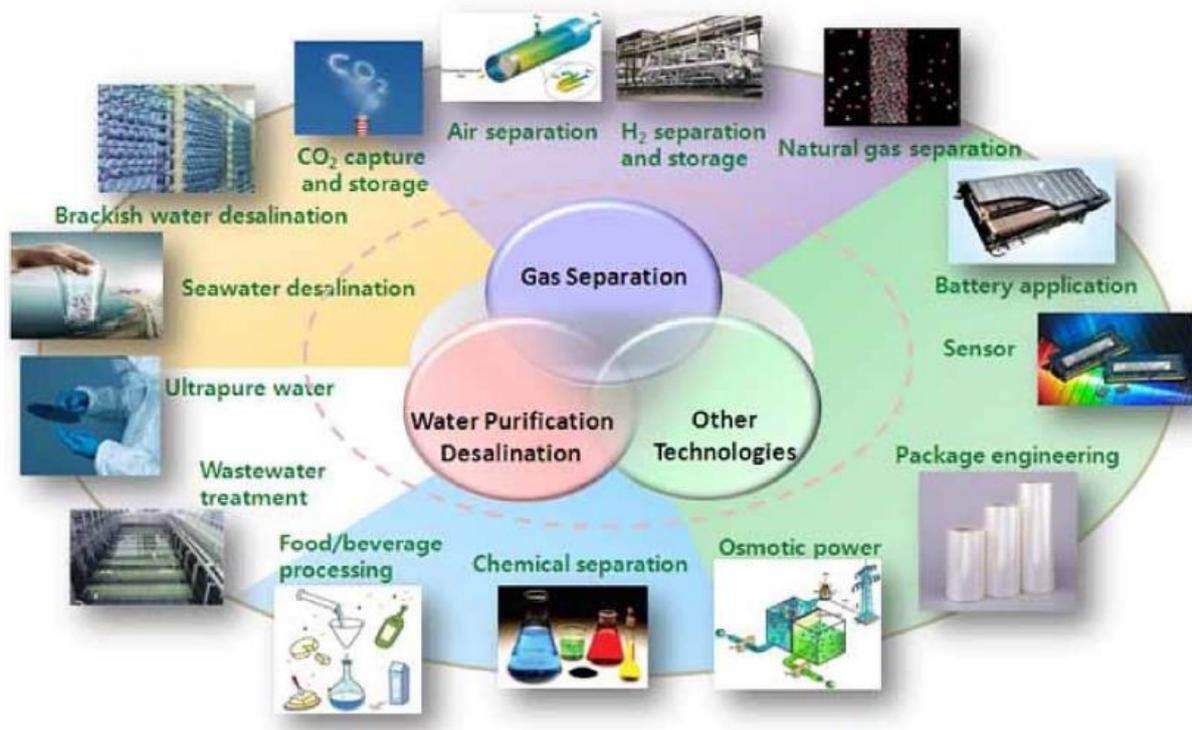
Figure 1.6 | Applications of Graphene-based nanosheets in different fields [55]

1.2   Production techniques of graphene

Nowadays, a lot of production techniques of graphene have been developed. In general, they are classified into two major classes: *i.e.* bottom-up and top-down processes. Concerning bottom-up approaches, the 2D network of graphene is built by forming covalent bonds from chemical reactions of molecules. [57–59] This method, like Chemical Vapor Deposition (CVD) and epitaxial growth, can yield graphene with high quality and large area. However, its disadvantages, small-scale production and high cost, are nonnegligible. [60–66] For the way of top-down routes, graphene is produced by exfoliating raw graphite, which can be accomplished under different environmental conditions, such as mechanical cleavage and liquid-phase exfoliation (LPE). [67,68] Graphene produced by this way has limited size and area, but this is a promising way to realize industrial production at lower cost.

1.2.1 Bottom-up method

CVD and epitaxial growth are both main methods for bottom-up fabrication of graphene. During the CVD process, gas species are fed into the reactor and pass through the hot zone,

where hydrocarbon precursors decompose to carbon radicals at the metal substrate surface and then form single-layer or few-layer graphene. In that case, the metal substrate not only work as a catalyst to lower the energy barrier of the reaction, but also determines the graphene deposition mechanism, which ultimately affects the quality of graphene. [60] Ni and Cu are the two most commonly used metal substrates for graphene CVD. Figure 1.7 displays examples of graphene grown from Ni and Cu substrate respectively.
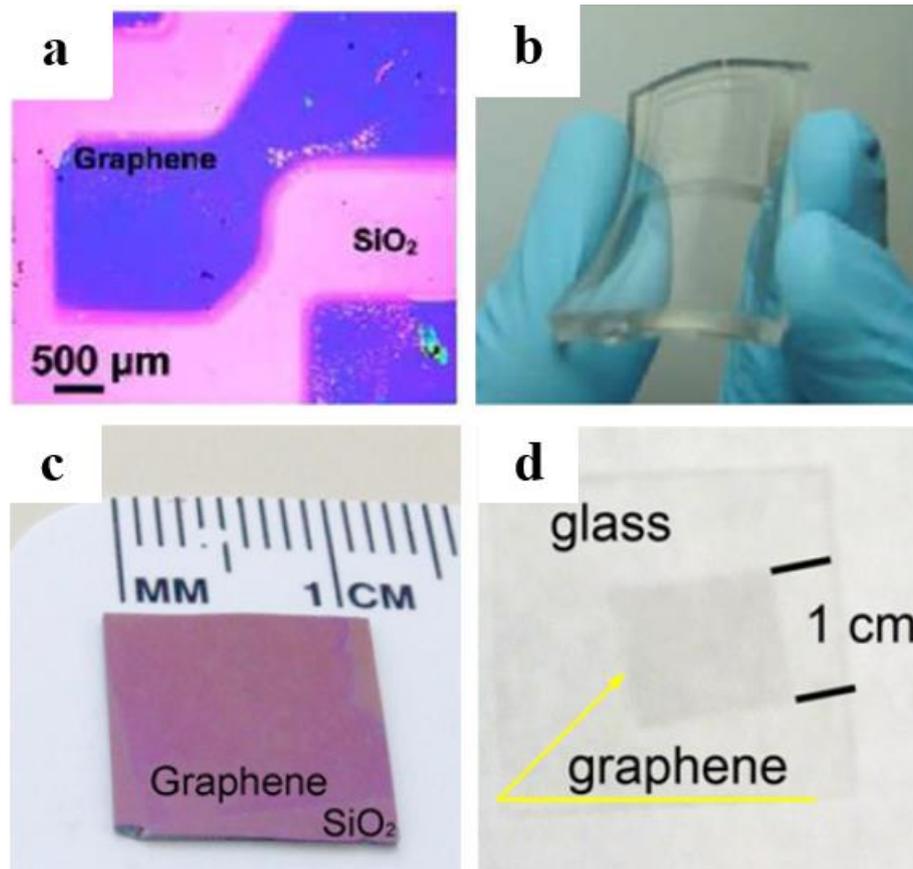
Figure 1.7 | Optical images of graphene transferred from Ni surface to (**a**) SiO$_2$/Si substrate and (**b**) PDMS substrates. Photographs of transferring as-prepared graphene from Cu surface onto (**c**) Si/SiO$_2$ substrate and (**d**) a glass plate [60,61]

The extensive research for epitaxial graphene has focused on growth graphene on SiC substrate (6H and 4H types), and most graphene growth occurred on its hexagonal polytypes. [69–72]. Specifically, graphene is grown on 0001 face (Si-terminated) and 000$\bar{1}$ face (C-terminated) of 4H- and 6H-SiC by annealing at high temperature and in ultrahigh vacuum (UHV) environment. [73] During the annealing process, Si leaves the SiC, letting C behind on the top of the surface to form graphene. Figure 1.8 shows the epitaxial graphene that is grown on SiC at high

temperature (2000 $^\circ$C) sublimation at 1 atm in Ar environment. The as-prepared graphene possesses a large area of 20×20 mm^2 with a control of monolayers number and spatial uniformity. [74,75]
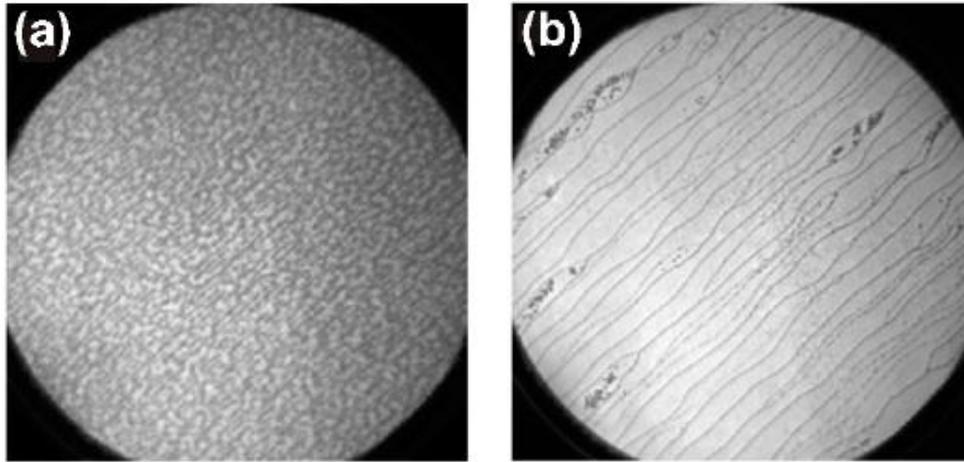
Figure 1.8 | Graphene layers grown in (**a**) vacuum; (**b**) Ar [75]

1.2.2 Top-down method

As mentioned above, within the top-down concept, graphene is produced by exfoliating raw graphite. To overcome the Van der Waals forces in graphite (~61 m eV per carbon atom), it is required an energy input of over 2 eV nm $^{-2}$ of graphene surface (~38 carbon atoms per nm^2) for exfoliation. [76] In general, there are two types of force that can be applied: *i.e.* normal force and lateral force. For example, the micromechanical cleavage using Scotch tape utilizes the normal force to peel graphene from graphite, [9,77] whereas ball milling strategy to exfoliate graphene is achieved by mainly generating shear force. [78] Besides, the fragmentation effect, another auxiliary way, is produced because the bulk graphite or graphene nanosheet can be fragmented into smaller crystals during the exfoliation. Figure 1.9 illustrates those mechanics ways as well the Scotch-tape based micromechanical cleavage and ball milling process. [78]
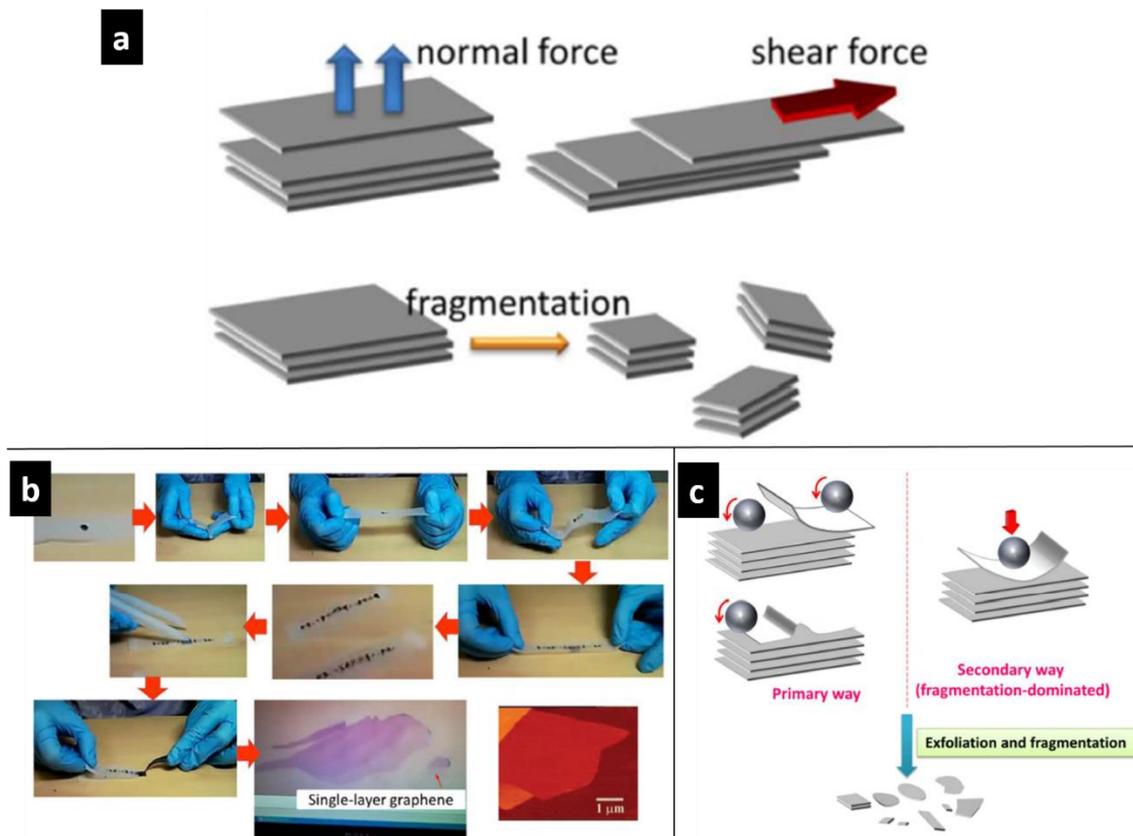
Figure 1.9 | (**a**) Two ways to overcome the Van der Waals force between graphite layers and the auxiliary effect of fragmentation. Illustration of the exfoliation by (**b**) Scotch-tape based micromechanical cleavage of highly ordered pyrolytic graphite and (**c**) ball milling of graphite. [78]

1.3 Liquid-phase exfoliation of graphene dispersing in aqueous media

Within the top-down method, alongside the Scotch-tape based micromechanical cleavage and ball milling strategies, liquid-phase exfoliation (LPE) is the most promising technique to yield graphene on industrial scalability. The resultant nanosheets dispersed in a liquid medium can be further manipulated via various processes, like blending, mixing, casting, spin-coating, impregnation or functionalization for many applications. [76,79,80] During LPE process, ultrasonication is widely used. The ultrasonic waves produce cavitation bubbles in the solvent, these bubbles collapse with pressure increasing to generate high energy micro-jets and shock waves which can exert compressive stress to bulk graphite inducing exfoliation. [78,81] Special mechanism have been demonstrated as: *i*) micro-jets can wedge into the interlayer spacing of

17

graphite and induce exfoliation; *ii*) unbalanced compressive stress in two adjacent graphene layers leads to a shear-induced exfoliation. (see Figure 1.10)
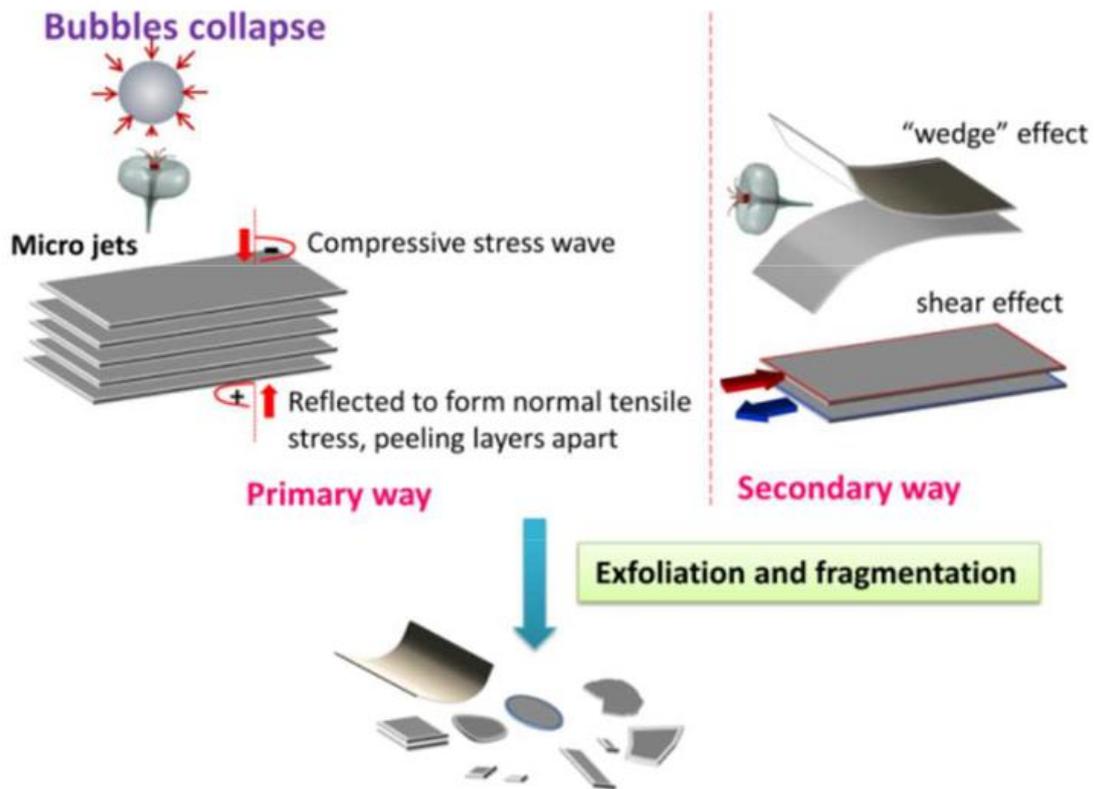
Figure 1.10 | Schematic illustration for exfoliation mechanism via sonication

Graphite can be easily exfoliated into single-layer and few-layer graphene by LPE and dispersed in a range of organic solvents with a high boiling point, such as N-methyl-pyrrolidone (NMP) and N, N-dimethylformamide (DMF). [82] Unfortunately, those solvents pose difficulties to be removed for the next step and their toxicity is harmful to environment. Water is ideal solvent for LPE due to its low-boiling point, low cost, abundance, safety, and environmental protection. However, the symmetrical structure of pristine graphite or graphene is hydrophobic, they can be hardly exfoliated and dispersed in water. To circumvent this issue, there are two main routes: *i*) direct exfoliation of graphite in water with assistance of surfactant or polymer stabilizers to achieve graphene aqueous dispersion; *ii*) oxidation of graphite to produce graphite oxide before its exfoliation in water. [83–87] The main advantage of the first method is to keep the graphene's electrical conductivity, and that of the second is to obtain a higher concentration of GO in the final dispersion solution, actually the oxidized graphene can be well-dispersed into

polymer matrix to form nanocomposites. [13,88,89] Table 1.1 compared the different routes to prepare colloidal dispersions of pristine graphene sheets.

Table 1.1 Comparison of different routes to prepare colloidal dispersions
of pristine graphene sheets

Starting materials	Exfoliation condition	yield	ref
Organic solvent			
Graphite powder (0.1 mg mL^{-1}) + NMP	Bath sonication, 30 min CF: 500 rpm, 90 min	0.01 mg mL^{-1}	[82]
Graphite flakes (50 mg) + organic solvent (10 mL) + NaOH flakes	Bath sonication, 1.5 h CF: 3000 rpm, 60 min	0.05–0.07 mg mL^{-1}	[90]
Graphite fine powder (5 mg) + particular aromatic solvents (1 mL)	Ultrasound bath, 135 W, 1 h left for 5 days	0.05–1 mg mL^{-1}	[84]
Graphite powder (3.3 mg mL^{-1}) + IPA or chloroform or acetone	Bath sonication, 16 W, 48 h CF: 500–5000 rpm, 45 min	0.01–0.5 mg mL^{-1}	[91]
Graphite flakes (0.3 g) + NMP (50 mL)	Sonication, 12 h, thermal treatment, 400–800 ºC sonication, another 3 h CF: 2000–8000 rpm	0.05–1 mg mL^{-1}	[92]
Natural graphite powder (10 mg mL^{-1}) + organic salt (20 mg mL^{-1}) + organic solvent	Bath sonication, 100 W, 2 h CF: 3000 rpm	0.1–1 mg mL^{-1}	[93]
Aqueous			
Graphite (0.1–14 mg mL^{-1}) + SDBS (5–10 mg mL^{-1}) + water (25 mL)	Low power sonic bath, 30 min CF: 500 rpm, 90 min	0.002–0.05 mg mL^{-1}	[94]
Natural graphite powder (100 mg mL_1) + Pluronic P-123 (0.5–1 wt%) or other surfactant	Bath sonication, 2–5 h CF: 5000g, 5 min	0.9–1.5 mg mL^{-1}	[95]
Graphite fine powder (250 mg) + deionized water (50 mL) + PVP (1 g)	Bath sonication, 135 W, 9 h CF: 1500 rpm, 30 min	0.1 mg mL^{-1}	[85]
Graphite powder (0.1 mg mL^{-1}) + Py-NH$_2$ or Py-SO3 (0.4 mg mL^{-1}) + deionized water	Bath sonication, 130 W, 0 ºC, 1 h CF: 4000 rpm, 20 min	—	[96]
Graphite (5 mg mL^{-1}) + NaC (0.1 mg mL^{-1}) + water (400 mL)	Bath sonication, 80 W, 430 h CF: 500–5000 rpm, 30–90 min	0.05–0.3 mg mL^{-1}	[97]
Expandable graphite (2 mg) + RB (0.5 mg) + 10% DMA aqueous solution	Bath sonication, 250 W, 6–10 h CF: 500–9000 rpm, 20–30 min	12 wt%	[98]
Graphite powder (100 mg) + PCA (16.5 mg) + methanol (50 mL) + distilled water (200 mL)	Bath sonication, 45 min + 1 day settle overnight	1 wt%	[99]

1.3.1 Exfoliation of graphite in water with assistance of polymer stabilizers

The pristine graphite can be exfoliated and dispersed into poor solvents using noncovalent surfactants, small ions/ molecules, or polymers as stabilizers. [79,94,100,101] The polymer-assisted method is of interest for polymer matrix composites formation.

Polyvinylpyrrolidone (PVP) is a harmless, inexpensive and biocompatible polymer, which is considered as an efficient polymer stabilizer for graphene dispersion in a variety of solvents. For instance, in 2009, Bourlinos *et al.* exfoliated crystalline graphite to graphene in aqueous solution via the assistance of PVP. [85] Furthermore, authors proposed that the polymer-assisted liquid phase exfoliation approach can be extended to other water-soluble biomacromolecules, including certain proteins and cellulose derivatives. Figure 1.11 A shows a digital photograph of graphene-dispersed aqueous solution with the presence of albumin and a TEM image of the folded graphene and an albumin. Based on this work, Green *et al.* proposed an effective technique for dispersing graphene in a series of solvents with assistance of polymer. [102] Figure 1.11 B demonstrated that PVP-stabilized graphene aqueous solution is processed by freeze-drying to obtain the PVP/graphene powders that can be re-dispersed in water without any sonication. Finally, high-concentration graphene dispersions up to 0.7 mg mL^{-1} are achieved.
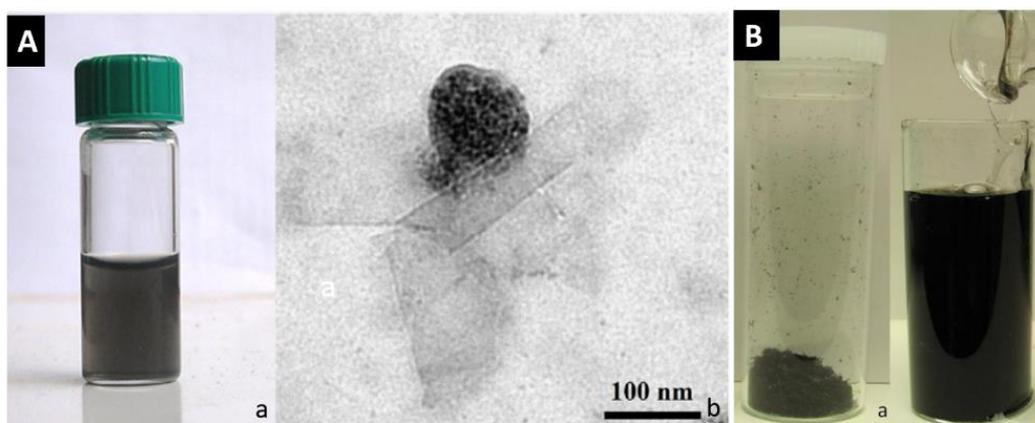
Figure 1.11 | (A) (a) Photograph of graphene-dispersed aqueous solution with the presence of albumin. **(b)** TEM image of the folded graphene and an albumin. [85] **(B)** Digital photographs of **(a)** freeze-dried PVP stabilized graphene and **(b)** re-dispersed PVP stabilized graphene in water. [102]

Besides, cellulose nanocrystals (CNC) are also efficient stabilizers to produce graphene layers in aqueous dispersions.[87] Actually, a stable high-concentration of graphene aqueous dispersion

20

(>1 mg/mL) containing monolayer and few-layer nanosheets is prepared by direct exfoliation of graphite using 2 mg/mL of CNC as stabilizer. By using a lower CNC concentration of 0.2 mg/mL, the as-obtained mixture has a remarkably high graphene/CNC ratio up to 3.8.

1.3.2 Liquid-phase exfoliation of graphite oxide to graphene oxide in water

As remind, oxidation treatment of graphite renders it electrically insulating but leads to a great aqueous dispersion mostly composed of single-layer sheets, which are referred to graphene oxide (GO) sheets. [22,39,103–105] The graphene basal planes are mainly decorated with epoxide and hydroxyl groups, but also with some carboxyl and carbonyl groups that grown at the edges, which renders GO hydrophilic. [22] By leading a study on the surface charge (zeta potential) of as-prepared GO sheets dispersed in water, it is found that the GO sheets are highly negatively charged. Therefore, the formation of stable GO dispersions is more attributed to electrostatic repulsion, rather than just the hydrophilicity feature of GO. [106] (see Figure 1.12)
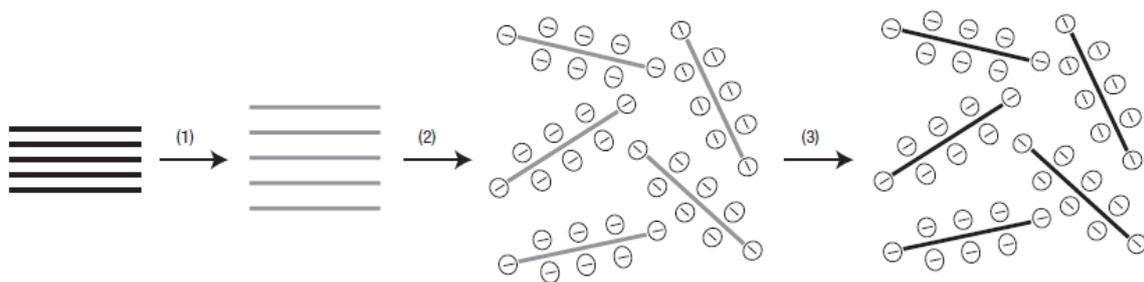
Figure 1.12 | Scheme of graphene dispersion process. (**1**) Oxidation of pristine graphite to graphite oxide; (**2**) Exfoliation of graphite oxide in aqueous solution to produce GO dispersion which is stabilized by electrostatic repulsion; (**3**) Hydrazine reduction of GO dispersion to rGO dispersion. [106]

On the other hand, the heterogeneous oxidation level at GO edge and GO surface suggests that GO dispersibility should be size-dependent. [105,107] A higher edge/area ratio of smaller GO sheets makes GO more hydrophilic and more stable when dispersed in solution because they have a higher charge density from the ionized -COOH groups on the edges. It is also reported that spontaneous size separation phenomenon of GO sheets is happened at the water surface: GO sheets with a size of < 1µm sink whereas ones with a size of > 5 µm float on the surface. [108] (see Figure 1.13a) This phenomenon is also observed at the interface of oil-water system. (see Figure 1.13b) Pickering emulsions can extract the GO sheets with larger size of > 5 µm from

their water dispersion in which smaller size GO sheets remain. There are no larger GO sheets in oil phase after several extraction steps because they are gradually depleted. [108]
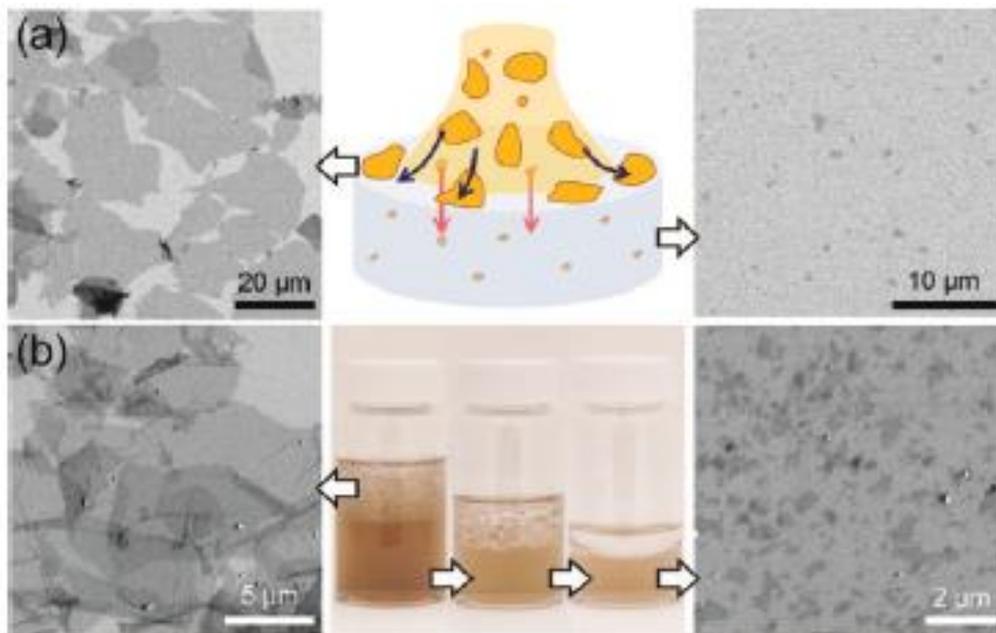
Figure 1.13 | Spontaneous size separation phenomenon of GO sheets at (**a**) water surface, and (**b**) water-oil interface [108]

1.4   Mechanism of graphene dispersion in liquid phase

1.4.1 Mechanism of direct dispersion of graphene in solvents

As mentioned above, pristine graphite or graphene are hydrophobic, thus, they can hardly be exfoliated and dispersed in water. Inspired from studies on carbon nanotubes successfully exfoliated in organic solvents such as N-methyl-pyrrolidone (NMP) [109–111], in 2008, Coleman group first reported exfoliation of graphite into single-layer and few-layer graphene in a range of organic solvents. [82] In that study, authors measured the graphene concentration in different organic solvents to find the optimum ones. Benzyl Benzoate, NMP, γ-Butyrolactone (GBL) and N, N-dimethylformamide (DMF), *etc.* have been found to present the best performances. Figure 1.14 a, b shows TEM images of monolayer graphene and multilayer graphene deposited from NMP. In Figure 1.14 c, the graph presents a statistical study of counting the number of layers per sheet. From a thermodynamic point of view, they further explained that the high dispersed graphene concentration depends on the small net energy cost. This energy balance is

chemically expressed as the enthalpy mixing which can be calculated approximately by equation 1.1:

$$\frac{\Delta H_{mix}}{V_{mix}} \approx \frac{2}{T_{flake}}(\delta_G - \delta_{sol})^2 \Phi \qquad (1.1)$$

Where $\delta_i = \sqrt{E_{sur}^i}$ is the square root of the surface energy of phase i, T_{flake} is the thickness of a graphene sheet, and Φ is the graphene volume fraction. The surface energy of NMP, DMF, and o-DCB are close to that of graphene, ~70 mJ m^{-2} (Figure 1.14 d), so they are able to disperse graphene. The solvent surface energy, E_{sur}^{sol}, has a relationship with surface tension, γ:

$$\gamma = E_{sur}^{sol} - TS_{sur}^{sol} \qquad (1.2)$$

here S_{sur}^{sol} is the solvent surface entropy. The optimum solvent surface tension for graphene exfoliation and dispersion is 40-50 mJ m^{-2}. [82] Moreover, Hildebrand solubility parameter of δ_T ~ 23MPa$^{1/2}$ and Hansen solubility parameters of δ_D ~ 18MPa$^{1/2}$, δ_P~ 9.3MPa$^{1/2}$ and δ_H ~ 7.7MPa$^{1/2}$ are used to characterize good solvents for graphene by measuring the graphene dispersibility in 40 solvents. [112]
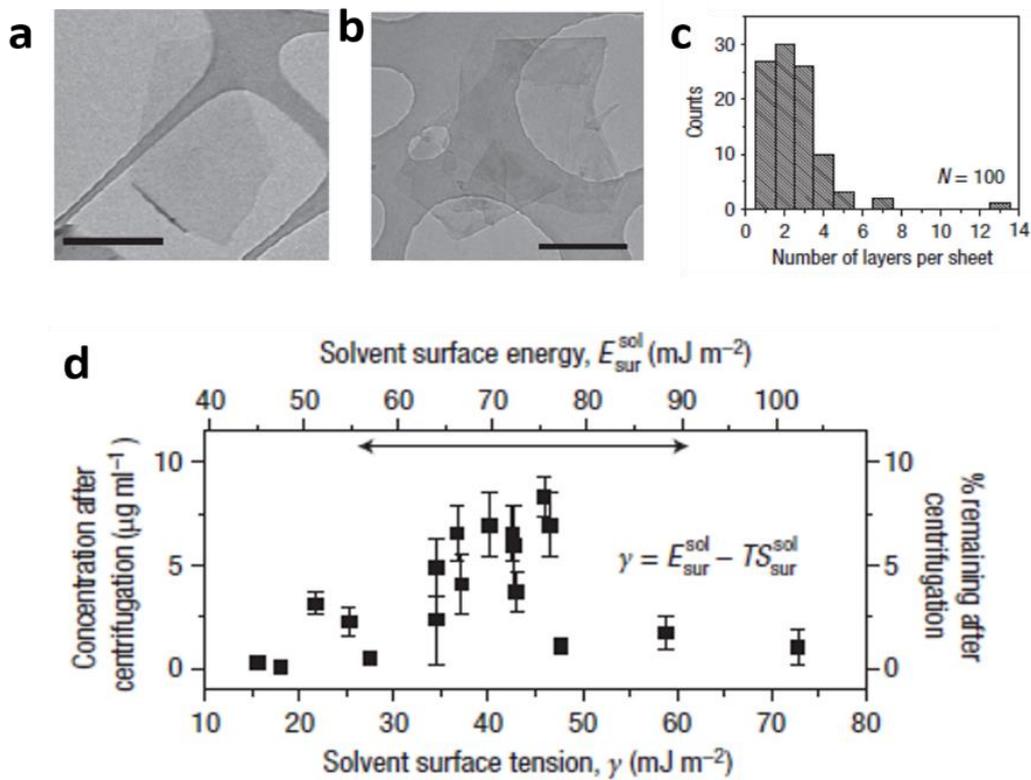
Figure 1.14 | TEM images of graphene nanosheets deposited from NMP with (**a**) a monolayer and (**b**) a multilayer (scale bars: 500 nm). (**c**) Histogram of the number of

graphene flakes as a function of the number of monolayers per flake in NMP. (**d**) Graphene concentration in different solvents plotted versus solvent surface tension.

In addition, increasing exfoliation time can also increase graphene concentration during the liquid-phase exfoliation process. [113] A process relying on low-power sonication for a long time (up to 460 h) is demonstrated to obtain a higher graphene concentration in NMP (up to 1.2 mg mL⁻¹). [113] Figure 1.15 shows that with sonication time from 0.5 h to 270 h, the graphene dispersion concentration rises steadily from 0.06 mg mL⁻¹ to the saturation at 1.2 mg mL⁻¹, respectively. The flake dimensions induced with sonication time as $t^{-1/2}$ indicated that the size of graphene sheets decreases with exfoliation time. As shown in Figure 1.15 b, the mean length and width reduced from ~3 to ~1 µm and from ~1µm to ~300 nm, respectively.
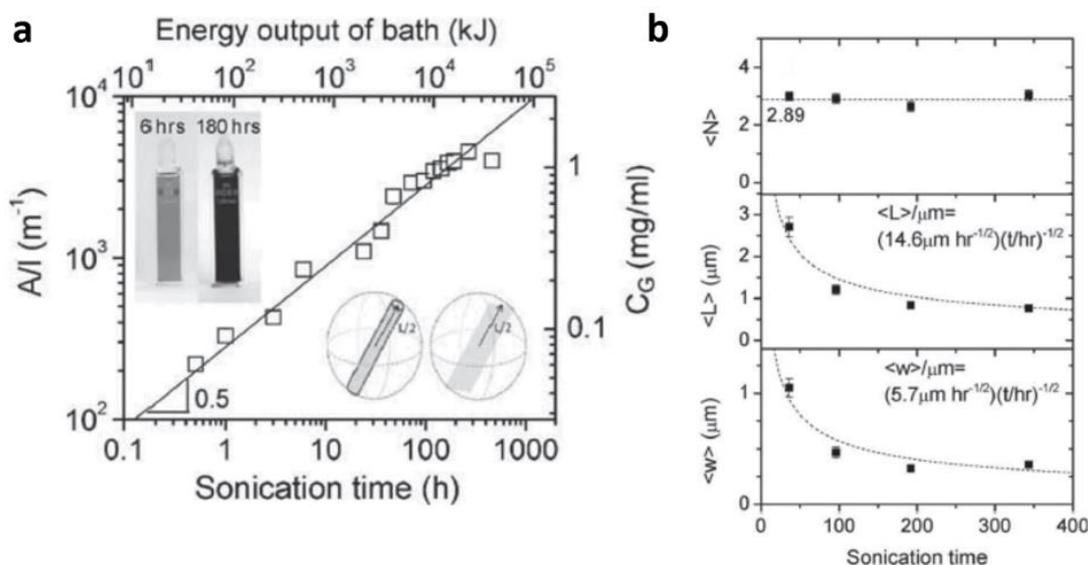
Figure 1.15 | (**a**) Graphene concentration versus sonication time. The inset of top left shows graphene dispersion after 6 h and 180 h sonication time. (**b**) Mean monolayer number per flake, mean length and width of graphene flakes as function of sonication time, respectively. [113]

1.4.2 Mechanism of polymer assisted LPE for pristine graphene dispersion

In general, the polymer stabilization of graphene in solution is explained by the steric force mechanism. Specifically, the polymer is partially adsorbing on graphene surface and it partially protrudes into solvent. Here, the interaction of polymer and surface could be π-π, hydrophobic,

Van der Waals, electrostatic or charge transfer. The protruding parts could provide the steric force between graphene layers, the produced repulsive force prevents the nanosheets agglomeration and stabilizes them in solvent. [114,115] Xu *et al.* demonstrated that noncovalent liquid-phase exfoliation of graphite in THF or Chloroform with hyperbranched polyethylene (HBPE) as stabilizer can increase graphene concentration from 0.045 mg mL^{-1} in THF and 0.18 mg mL^{-1} in chloroform to 3.4 mg mL^{-1} after further concentrated, while remaining stable. [115] The mechanism has been described as noncovalent nonspecific CH-π interactions between HBPE and the graphene surface without any functionalities. The CH-π interactions are generally weak hydrogen bonds. [116] By this way, HBPE adsorbs on surface to sterically stabilize the exfoliated graphene against their reaggregations. (see Figure 1.16)
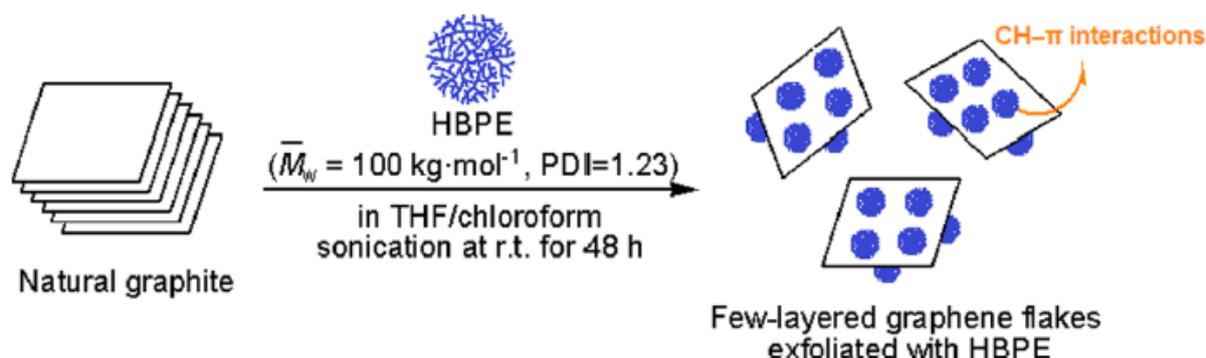
Figure 1.16 | Scheme of Noncovalent liquid-phase Exfoliation of Graphite in THF or Chloroform with HBPE as the stabilizer. [116]

From this perspective, polymer adsorption on layer materials' surface is a key step resulting in the steric force preventing stack of the sheets. Therefore, evaluation of free energy during adsorption process is useful to build an equivalent framework to choose the solvent/ polymer combination for stabilized a given colloid. In general, when a polymer in "dilute" solution closes to a surface, it would like to adsorb on the surface to gain energy. Flory theory assumed that a Kuhn monomer (the length of Kuhn monomer: b) in contact with the surface can gain energy of $-\delta_e kT$, where $0 < \delta_e < 1$ represents week adsorption. [117] In order to gain more adsorption energy, the chain would try to contact with surface in an increase numbers of Kuhn monomer (the total number within one polymer chain: N). At the same time, the chain would have to confine its conformation to a layer which thickness should be smaller than the end-to-end distance (R) of polymer coil, $\xi_{ads} < R$, then losing the conformational entropy. (see Figure

1.17) The total free energy of a weekly adsorbed polymer chain can be calculated by equation 1.3.
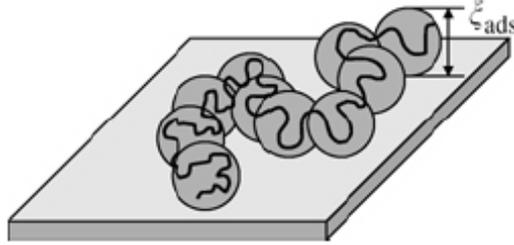
Figure 1.17 | A polymer chain adsorbed weekly on a surface with a thickness ξ_{ads}

$$F = F_{conf} + F_{int} \approx kTN(\frac{b}{\xi_{ads}})^{5/3} - \delta_e kTN\frac{b}{\xi_{ads}} \tag{1.3}$$

The adsorption free energy $F_{int} = -\delta_e kT$ plays important role during polymer adsorption process because it can reduce free energy of the whole system. Combining with quasicrystalline lattice model from A Silberberg, the physical meaning of $F_{int} = -\delta_e kT$ is described as the exchange of a solvent molecule in contact with the surface in a solvent reference by a polymer monomer with equivalent size from the pure reference phase. [118] Therefore, δ_e can be understood as a combination of interactions among graphene, polymer and solvent. Unfortunately, there are less researches found to give more explanations of δ_e.

May *et al.* have explored the free energy of polymer adsorbed on 2D materials to stabilize them in solution. Specifically, they showed that graphite flakes, powdered hexagonal boron nitride (BN) and powdered MoS_2 were exfoliated in tetrahydrofuran (THF) or cyclohexanol (CXO) with a set of polymers like polybutadiene (PBD), polystyrene (PS), poly (vinyl chloride) (PVC), poly (vinyl acetate) (PVAc), poly (methyl methacrylate) (PMMA), cellulose acetate (CA), *etc.* as stabilizers, then the 2D materials' concentration were increased to varying degrees. Through a modeling study, they built a relationship (see equation 1.4) for predicting the favorable energy of stabilization only when the Hildebrand solubility parameters of graphene, polymer and solvent are similar. [114]

$$\Delta F = KTN(\frac{\frac{2v_S}{z}(\delta_S - \delta_P)(\delta_G - \delta_S)}{kT})^2 \tag{1.4}$$

1.5 Graphene/polymer nanocomposites for electrochemical capacitors

1.5.1 Introduction of electrochemical capacitor

Electrochemical capacitor (EC), or the so-called supercapacitor exhibits high power density, high charge/discharge rates, and long cycle life. Therefore, EC is considered as one of the most promising energy storage device to replace batteries, especially in wearable electronic devices, and electric vehicles (EV). [119–121] The mechanism of EC for energy storage is principally based on two types of electrochemical behaviors: electric-double-layer (EDL) capacitance and pseudocapacitance. [122] In general, EDL capacitor uses active carbon (AC) as the electrode material because of its high surface area. The charge accumulation at electrode/electrolyte interface is attributed to the EDL capacitance. By contract, pseudocapacitor contains a metal oxide or a conducting polymer as the electrode material, which storage capacities via reversible Faradic redox reactions. (see Figure 1.18) Generally, pseudocapacitor exhibits high pseudocapacitance, but limited stability during the charge/discharge cycling. EDL capacitors exhibit good stability but unsatisfactory EDL capacitance. [123–125]
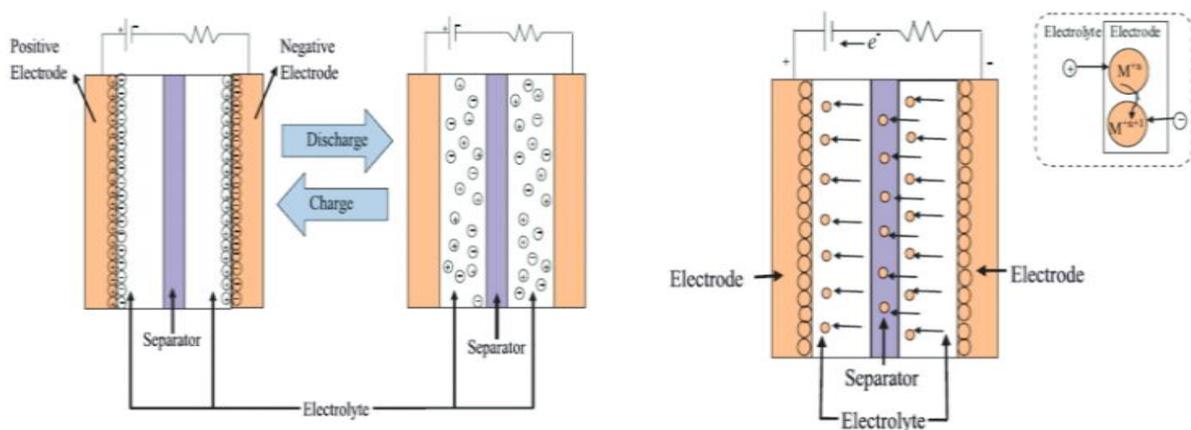
Figure 1.18 | Two mechanisms of EC for energy storage: electric-double-layer (EDL) capacitance and pseudocapacitance [126]

The electrochemical performance of a EC is conventionally evaluated based on the following aspects: *a)* power density considerably higher than that of batteries with > 10 Wh kg^{1}, *b)* fast charge/discharge rate within seconds, *c)* outstanding cycle life more than 100 times of batteries, *d)* low self-discharging rate, and e) safe operation and f) low cost. Besides, the time constant

27

represented as resistance (R) time capacitance (C) is also an important parameter for evaluation of EC's performance. A large time constant value indicates a lower leakage or a self-discharging rate. [127]

1.5.2 Application of Graphene-based nanosheets in electrochemical capacitor

Graphene can be applied to prepare EDL capacitor thanks to its intrinsic properties: lightweight, high surface area, extraordinary electrical conductivity, outstanding mechanical properties and great chemical stability. Theoretically, the specific capacitance of monolayer graphene is ~21 $\mu F.cm^{-1}$, which sets a higher limit of EDL capacitance for all carbon-based electrode. [128] Then corresponding EDL capacitance value of 550 F g^{-1} is asserted as soon as the surface area is entirely used. [129] In addition, GO with enriched oxygen-containing functional groups provides additional pseudocapacitance, its specific capacitance is up to 189 F g^{-1}, as well as it displays great rate performance and outstanding cycle durability. [130]

However, in scalable graphene production, the nanosheets yielded by top-down method normally trend to agglomerate and restack together, rendering the capacitive ability of materials much lower than theoretical value. [127,131–133] Graphene/polymer hybrid composites have a tremendous potential for energy applications, especially applied as EC. [134] This hybrid system can take advantages of both Graphene-based nanosheets and polymer. On one hand, Graphene-based nanosheets can contribute to the EDL capacitance or pseudocapacitance, and their presence in hybrid composites can enhance polymer's electrical conductivity and mechanical properties. On the other hand, polymers can contribute not only to the pseudocapacitance, but also play a stabilizer's role to prevent the nanosheets' agglomeration, resulting in the improvement of nanosheets' dispersibility and stabilization in solvent. Thus, the overall electrochemical properties of graphene/polymer hybrid composites are improved.

1.5.3 Preparation of graphene/polymer hybrid composites

Graphene/polymer hybrid composites generally can be fabricated by noncovalent or covalent approaches, which are classified on basis of the interaction between both specimens. (see Figure 1.19) [135] Noncovalent functionalization of graphene is accomplished via physisorption of polymer molecules on graphene surface through $\pi-\pi$ stacking, hydrophobic interaction or electrostatic interactions. [135,136] Direct mixing of both specimens, or in situ polymerization of

monomers in the presence of graphene are both belonging to noncovalent functionalization. This approach can improve graphene's dispersibility and stability in solvent. On the other hand, covalent functionalization of graphene is realized by chemical reaction with polymers, such as condensation reaction, cycloaddition reaction or radical polymerization. Specifically, polymers with active groups are chemically grafted on graphene, or graphene attached chemically with initiators to initiate polymerization. [137,138] This approach provides relatively more stable composite systems comparable to noncovalent functionalization.
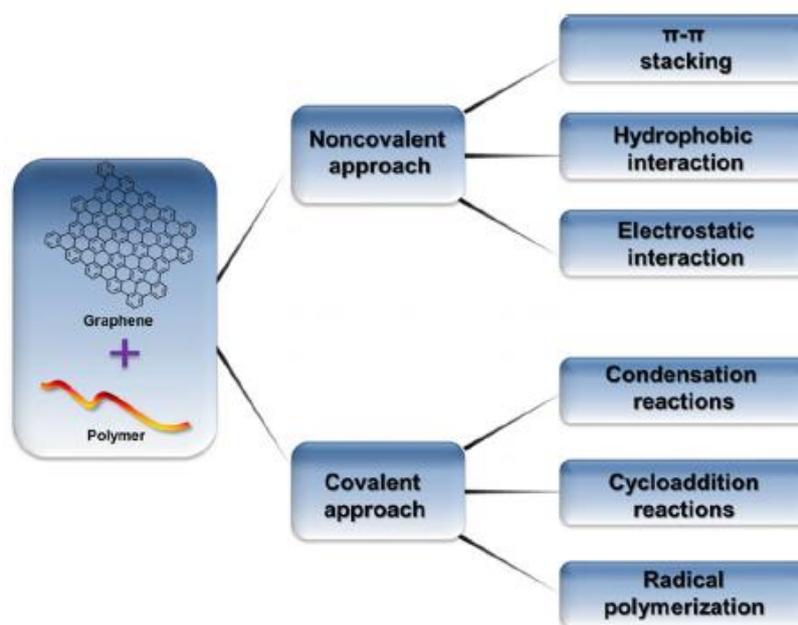
Figure 1.19 | Scheme of functionalization of graphene with polymers by noncovalent approach and covalent approach. [135]

1.5.4 Graphene/polymer hybrid composites for electrochemical capacitors electrode

Conducting polymers, PANI and PPy, are the most commonly used in combination with graphene for hybrid composites that display high electrochemical performance. They have been studied by many groups. [139–147] For example, PANI nanowire arrays are vertically grown on GO nanosheets to produce a hierarchical nanocomposite that exhibit a high specific capacitance reaching up to 555 F g^{-1} at a current density of 0.2 A g^{-1}. This value is higher than 298 F g^{-1} for random connected PANI nanowires prepared by the same way, and the cyclic stabilization is also better than that of pure PANI. [142] (see Figure 1.20) Qu *et al.* reported a 3D porous GO/PPy

foam as a compressible EC. The foam displays durable compression tolerance without structural collapse, and high specific capacitance of 360 F g^{-1} at a current density of 1.5 A g^{-1}. [144]
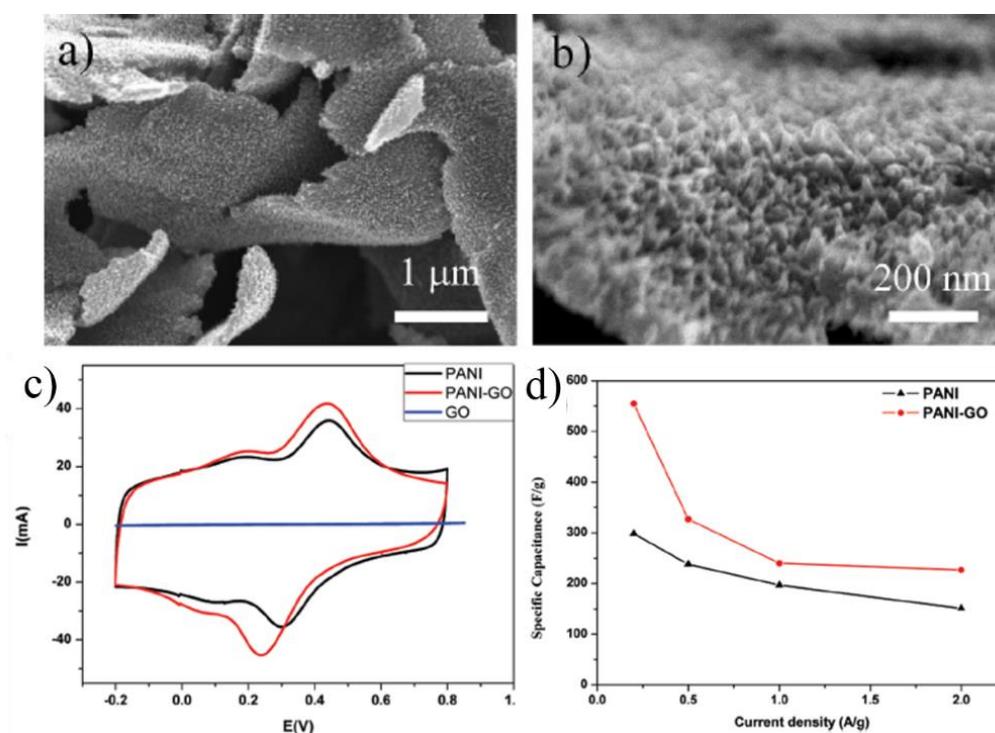
Figure 1.20 | (**a, b**) SEM images of PANI/GO nanocomposites; (**c**) CV curves of pure GO, random connected pure PANI nanowires, and PANI/GO nanocomposites at a potential windows of -0.2-0.8 V at a scan rate of 20 mV s^{-1}; (**d**) the specific capacitance of random connected pure PANI nanowires and PANI/GO nanocomposites with different current densities. [142]

Alongside the above-discussed conducting polymers, other polymers including cellulose, polyselenophene, epoxy, and Polyvinyl alcohol (PVA) have been also used with graphene to prepare ECs' electrode. [148–154] The low-cost PVA is an interesting material due to its excellent properties in transparency, flexibility, aqueous solubility, and ease of processing. [155] With the incorporation of graphene, the properties of PVA have been improved in several aspects such as mechanical properties, optical properties, impermeability, electrical and thermal conductivity. [156–161] Indeed, graphene/PVA hybrid composites can be good candidates to investigate their electrochemical activity. For example, GO/PVA hybrid composites containing 0.5% wt/wt GO exhibit higher specific capacitance of ~400 F g^{-1} at a scan rate of 10 mV/s, which is retained to ~92% after 400 cycles. The specific capacitance of pure GO and pure PVA

are ~244 F g^{-1} and ~ 27 F g^{-1} respectively in the same conditions. [154] (see Figure 1.21) PVA/rGO hybrid fiber with a weight ratio of 10/90 displays a strength of 186 Mpa, a toughness of 11.3 J cm^{-3}, and a best capacitance of 241 F cm^{-3} in 1M H$_2$SO$_4$ electrolyte. Combination with its excellent flexibility and bending stability, PVA/rGO hybrid fiber possesses great potential for wearable electronic devices application. [151]
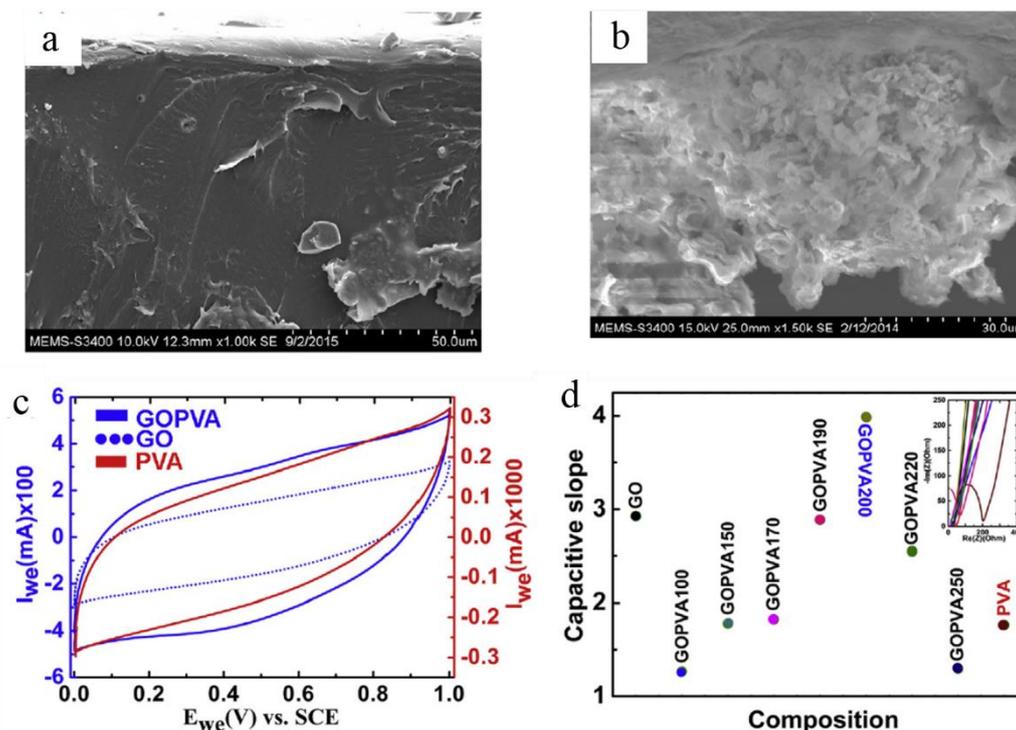
Figure 1.21 | SEM images of cross section in (**a**) GO/PVA and (**b**) GO; (**c**) Cyclic voltammogram of GO/PVA, pure GO, and pure PVA within a potential window range from 0 to 1V. (**d**) Capacitive slope given from the electrochemical impedance spectroscopy (EIS) plots. The color code of the dots is same with in the EIS plot inset. The comparison of capacitive slope suggests that GOPVA200 exhibits the highest slope comparing with other nanocomposite compositions. [154]

1.6 Electrochemical characterization

1.6.1 Cyclic voltammetry

Cyclic voltammetry (CV) is a tool commonly used in the electrochemistry field, which has been applied extensively to characterize the performance of electrical energy storage devices, such as batteries, electrochemical capacitors and full cells. In a CV measurement, the working

electrode potential is ramped linearly against time. By controlling the scan rate as well as the setting potential windows, the potential of samples is cyclically measured between the reference electrode and the working electrode, the corresponding current is measured between the counter electrode and the working electrode. Finally, the obtained data are plotted as a curve of current (*i*) versus applied potential (*E*), the specific capacitance can be evaluated as the total charge divided by the potential window in equation 1.5:

$$C_m = \frac{\int I \, dV}{2 \, m \, v \, \Delta V} \tag{1.5}$$

Where, C_m (F g^{-1}) represents the specific capacitance, I (A) is the current intensity, m is the mass of the active materials, v represents the scan rate, and ΔV represents potential windows.

Generally, for an ideal capacitor, its CV shows a perfect rectangular shape due to the negligible resistance, as shown in Figure 1.22a. However, for the real capacitors, they suffer from power loss during charge and discharge, which is caused by resistances in electrical contacts, electrodes, and electrolyte, the sum of these resistances is called Equivalent Series Resistance (ESR). Therefore, the rectangular shape of CV would deviate, which is shown in Figure 1.22b.
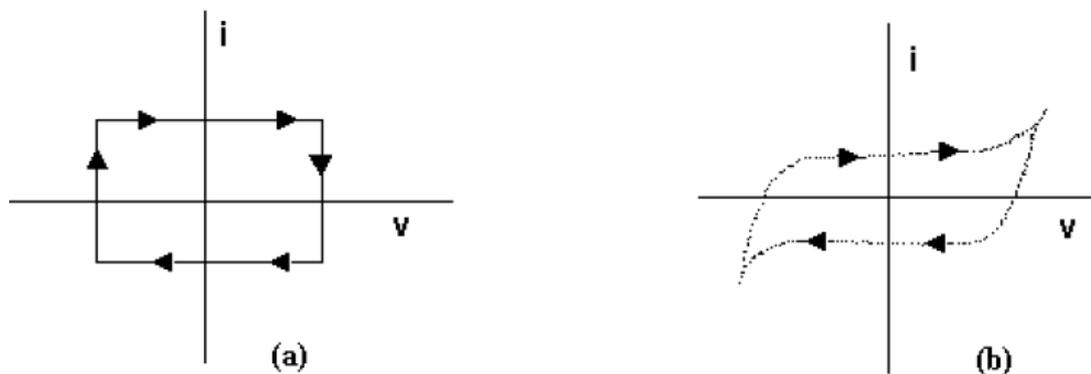
Figure 1.22 | Cyclic voltammetry curves of (**a**) ideal capacitor and (**b**) real capacitor

In the case of electrochemical capacitor, the types of electrolyte can affect the electrochemical behavior of electrode materials. Figure 1.23 compared the voltammetry characteristics of activated carbon AC at 5 mV/s measured in the electrolytes of 1M H_2SO_4 acidic solution, 1M tetraethylammonium tetrafluoroborate (TEABF$_4$) in acetonitrile (AN), and an electrolyte prepared with an ionic liquid, IL1, based on a bulky phosphonium cation. [163] Different performances were observed, for example, the voltage range can be extended using the IL1 solution containing 25% AN.
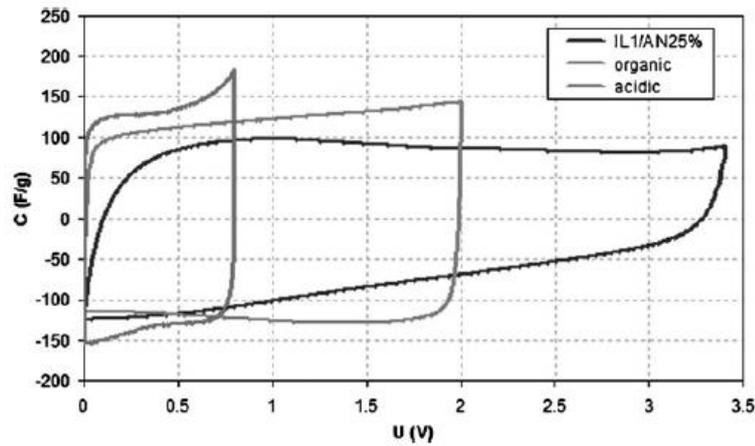
Figure 1.23 | Cyclic voltammetry curves at 5 mV/s scan rate for activated carbon AC in three electrolytic media. [163]

1.6.2 Galvanostatic charge and discharge measurement

The galvanostatic charge discharge (GCD) measurement is one of the most widely applied techniques in electrochemical capacitors field because it is not only used in laboratory environment, but also at industrial scale. GCD is an efficient approach to evaluate the materials' electrochemical capacitance by controlling current conditions to measure the voltage. GCD is also called chronopotentiometry (CP).

In a GCD measurement, a current at the working electrode is defined as a constant, and the resulting potential is measured between the working electrode and the reference electrode versus time. The specific capacitance of the working electrode is estimated by equation 1.6:[162]

$$C_m = \frac{I \times \Delta t}{m \times \Delta V} \tag{1.6}$$

Where, C_m (F g^{-1}) represents the specific capacitance, I (A) represents the discharge current, Δt *(s)* represents the discharge time, m (g) represents the mass of active materials, and ΔV represents potential windows.

1.6.3 Electrochemical impedance spectroscopy

Electrochemical impedance spectroscopy (EIS) is employed to investigate electrochemical system, for instance, explaining the adaption process, the reaction mechanism and capacitance behaviors of EC. EIS is generally performed with a potentiostat and assumes the superposition

of a sinusoidal signal with small amplitude (5-10 mV) over a DC voltage and monitoring the magnitude and phase angle of the resulting ac current. The resulting impedance is represented as:

$$Z(\omega) = Z'(\omega) + jZ''(\omega)$$

EIS data are plotted in the complex plane as so-called Nyquist plots, in which the real axis Z' is as x-axis and the imaginary axis Z'' is as y-axis. Figure 1.24 shows a typical Nyquist graphic of an ideal capacitor and of a EC in series with a resistance.
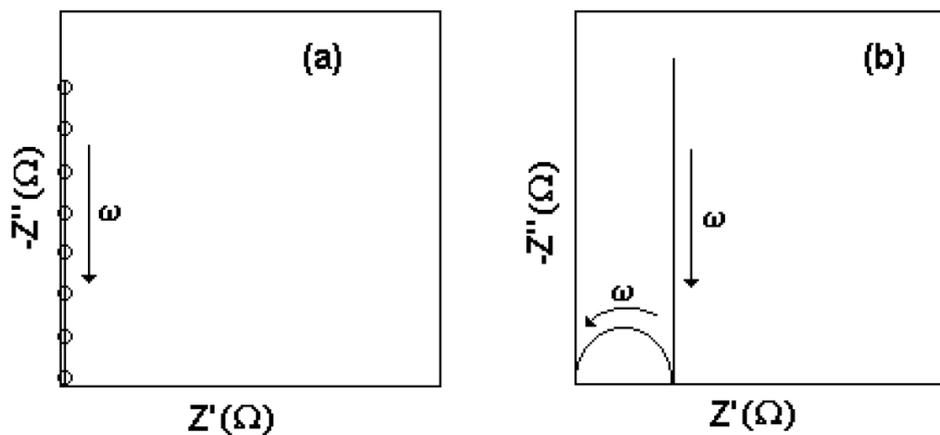
Figure 1.24 | Nyquist impedance plot of (**a**) an ideal capacitor and (**b**) a typical EC.

For an ideal capacitor, in Figure 1.23a, the line with a steep rising overlap with the imaginary axis Z''. The vertical slope means that capacitance is not various with frequency. However, for a real capacitor, the impedance plot exhibits an additional semicircle, which represents a parallel combination of a bulk resistance R_b and a geometrical capacitance C_g. R_b is generally produced by the ion migration due to the bulk electrolytes. And C_g is produced by the dielectric polarization of electrolyte under the influence of electric field. The interfacial polarization makes a double layer capacitor to form, which is characterized by the steep rising at lower frequencies' region of impedance plot.

1.7 Summary

Graphene-based nanosheets, as an advanced 2D material, display infinite potential in various application fields such as energy storage, conductive materials, protective coatings and *etc*. Graphene-based nanosheets can be produced by using both bottom-up or top-down approaches.

Moreover, among top-down method the liquid-phase exfoliation, appears as the most promising technique for large-scale production of graphene-base nanosheets. Actually, this way allows to get high concentration and well-dispersed graphene solutions.

Due to its low-boiling point, abundance, safety, low cost, water is an ideal solvent for liquid-phase exfoliation. However, pristine graphite can hardly be exfoliated and dispersed in water due to its hydrophobic feature. Moreover, strategies, like the use of a polymer as stabilizer or the introduction of oxygen-based groups within graphene, have proven to be effective to increase the nanosheets' concentration and their dispersible stabilization in aqueous media. However, the mechanism of stabilized graphene by polymer in a liquid phase is still not clear, it can be related to polymer physics theories including polymer solution theory and polymer adsorption theory.

In addition, noncovalent functionalization of graphene, performed via physisorption of polymer molecules on graphene surface through $\pi-\pi$ stacking, hydrophobic interaction or electrostatic interactions *etc*. can be directly used to fabricate hybrid composites. These hybrid composites have a tremendous potential for energy applications, especially applied as electrochemical capacitors.

References

1. Carbon | Facts, Uses, & Properties. Encyclopedia Britannica (2020). https://www.britannica.com/science/carbon-chemical-element.

2. Stanford scientists find a new way to turn graphite into diamond. *New Atlas* (2014). https://newatlas.com/graphite-synthetic-diamond-platinum-stanford/31496/

3. Chung, D. D. L. Review Graphite. *Journal of Materials Science* 37, 1475–1489 (2002).

4. Ke, Q. & Wang, J. Graphene-based materials for supercapacitor electrodes – A review. *J. Materiomics* **2**, 37–54 (2016).

5. Wallace, P. R. The Band Theory of Graphite. *Phys. Rev.* **71**, 622–634 (1947).

6. Dresselhaus, M. S. & Dresselhaus, G. Intercalation compounds of graphite. *Adv. Phys.* **51**, 1–186 (2002).

7. Shenderova, O. A., Zhirnov, V. V. & Brenner, D. W. Carbon Nanostructures. *Crit. Rev. Solid State Mater. Sci.* **27**, 227–356 (2002).

8. Land, T. A., Michely, T., Behm, R. J., Hemminger, J. C. & Comsa, G. STM investigation of single layer graphite structures produced on Pt(111) by hydrocarbon decomposition. *Surf. Sci.* **264**, 261–270 (1992).

9. Novoselov, K. S. Electric Field Effect in Atomically Thin Carbon Films. *Science* **306**, 666–669 (2004).

10. Pham, V. P. Direct Growth of Graphene on Flexible Substrates toward Flexible Electronics: A Promising Perspective. *Flexible Electronics*, chapter 4 (IntechOpen. Press, 2018)

11. Chemical functionalization of graphene and its applications. *Prog. Mater. Sci.* **57**, 1061–1105 (2012).

12. Brodie, B. C. XIII. On the atomic weight of graphite. *Philos. Trans. R. Soc. Lond.* **149**, 249–259 (1859).

13. Kim, H., Abdala, A. A. & Macosko, C. W. Graphene/Polymer Nanocomposites. *Macromolecules* **43**, 6515–6530 (2010).

14. Staudenmaier, L. Verfahren zur Darstellung der Graphitsäure. *Berichte Dtsch. Chem. Ges.* **31**, 1481–1487 (1898).

15. Hummers, W. S. & Offeman, R. E. Preparation of Graphitic Oxide. *J. Am. Chem. Soc.* **80**, 1339–1339 (1958).

16. Reynosa-Martínez, A. C. *et al.* Effect of the degree of oxidation of graphene oxide on As (III) adsorption. *Journal of Hazardous Materials* **384**, 0304-3894 (2019).

17. Konios, D., Stylianakis, M. M., Stratakis, E. & Kymakis, E. Dispersion behaviour of graphene oxide and reduced graphene oxide. *J. Colloid Interface Sci.* **430**, 108–112 (2014).

18. Luo, L. *et al.* Preparation of Graphite Oxide Containing Different Oxygen-Containing Functional Groups and the Study of Ammonia Gas Sensitivity. *Sensors* **18**, (2018).

19. Dasari Shareena, T. P., McShan, D., Dasmahapatra, A. K. & Tchounwou, P. B. A Review on Graphene-Based Nanomaterials in Biomedical Applications and Risks in Environment and Health. *Nano-Micro Lett.* **10**, 53 (2018).

20. Shim, G., Kim, M.-G., Park, J. Y. & Oh, Y.-K. Graphene-based nanosheets for delivery of chemotherapeutics and biological drugs. *Adv. Drug Deliv. Rev.* **105**, 205–227 (2016).

21. Ciesielski, A. & Samorì, P. Graphene via sonication assisted liquid-phase exfoliation. *Chem. Soc. Rev.* **43**, 381–398 (2014).

22. Stankovich, S. *et al.* Synthesis of graphene-based nanosheets via chemical reduction of exfoliated graphite oxide. *Carbon* **45**, 1558–1565 (2007).

23. Bagri, A. *et al.* Structural evolution during the reduction of chemically derived graphene oxide. *Nat. Chem.* **2**, 581–587 (2010).

24. Zhang, B., Wang, Y. & Zhai, G. Biomedical applications of the graphene-based materials. *Mater. Sci. Eng. C* **61**, 953–964 (2016).

25. Geim, A. K. & Novoselov, K. S. The rise of graphene. *Nat. Mater.* **6**, 183–191 (2007).

26. Park, S. & Ruoff, R. S. Chemical methods for the production of graphenes. *Nat. Nanotechnol.* **4**, 217–224 (2009).

27. Loh, K. P., Bao, Q., Ang, P. K. & Yang, J. The chemistry of graphene. *J. Mater. Chem.* **20**, 2277–2289 (2010).

28. Zhong, Y., Zhen, Z. & Zhu, H. Graphene: Fundamental research and potential applications. *FlatChem* **4**, 20–32 (2017).

29. Neto, A. C. & Geim, A. Graphene: Graphene's properties. *New Sci.* **214**, iv–v (2012).

30. Zhu, Y. *et al.* Graphene and Graphene Oxide: Synthesis, Properties, and Applications. *Adv. Mater.* **22**, 3906–3924 (2010).

31. Bolotin, K. I. *et al.* Ultrahigh electron mobility in suspended graphene. *Solid State Commun.* **146**, 351–355 (2008).

32. Wang, H., Zhang, X. & Takamatsu, H. Ultraclean suspended monolayer graphene achieved by *in situ* current annealing. *Nanotechnology* **28**, 045706 (2017).

33. Berber, S., Kwon, Y.-K. & Tomanek, D. Unusually High Thermal Conductivity of Carbon Nanotubes. *Phys. Rev. Lett.* **84**, 4613–4616 (2000).

34. Balandin, A. A. *et al.* Superior Thermal Conductivity of Single-Layer Graphene. *Nano Lett.* **8**, 902–907 (2008).

35. Materials Design and Discovery Group *et al.* A route to high surface area, porosity and inclusion of large molecules in crystals. *Nature* **427**, 523–527 (2004).

36. Nair, R. R. *et al.* Fine Structure Constant Defines Visual Transparency of Graphene. *Science* **320**, 1308–1308 (2008).

37. Bunch, J. S. *et al.* Impermeable Atomic Membranes from Graphene Sheets. *Nano Lett.* **8**, 2458–2462 (2008).

38. Bîru, E. I. & Iovu, H. Graphene Nanocomposites Studied by Raman Spectroscopy. (ed. Nascimento, G. M.,) chapter 9 (Raman Spectroscopy, 2018).

39. Xu, Y., Bai, H., Lu, G., Li, C. & Shi, G. Flexible Graphene Films via the Filtration of Water-Soluble Noncovalent Functionalized Graphene Sheets. *J. Am. Chem. Soc.* **130**, 5856–5857 (2008).

40. Hui, Y. *et al.* A facile strategy to fabricate highly-stretchable self-healing poly(vinyl alcohol) hybrid hydrogels based on metal–ligand interactions and hydrogen bonding. *Polym. Chem.* **7**, 7269–7277 (2016).

41. Qi, K., Sun, Y., Duan, H. & Guo, X. A corrosion-protective coating based on a solution-processable polymer-grafted graphene oxide nanocomposite. *Corros. Sci.* **98**, 500–506 (2015).

42. Zong, P. *et al.* Functionally reduced graphene oxide supported iron oxides composites as an adsorbent for the immobilization of uranium ions from aqueous solutions. *J. Mol. Liq.* **240**, 578–588 (2017).

43. Ji, X., Xu, Y., Zhang, W., Cui, L. & Liu, J. Review of functionalization, structure and properties of graphene/polymer composite fibers. *Compos. Part Appl. Sci. Manuf.* **87**, 29–45 (2016).

44. Zhang, Y., Fan, S., Li, S., Song, Y. & Wen, G. 3D porous oxygen-enriched graphene hydrogels with well-balanced volumetric and gravimetric performance for symmetric supercapacitors. *J. Mater. Sci.* **55**, 12214–12231 (2020).

45. Li, C. *et al.* Three dimensional graphene networks for supercapacitor electrode materials. *New Carbon Mater.* **30**, 193–206 (2015).

46. Horn, M., Gupta, B., MacLeod, J., Liu, J. & Motta, N. Graphene-based supercapacitor electrodes: Addressing challenges in mechanisms and materials. *Curr. Opin. Green Sustain. Chem.* **17**, 42–48 (2019).

47. Nag, A., Mitra, A. & Mukhopadhyay, S. C. Graphene and its sensor-based applications: A review. *Sens. Actuators Phys.* **270**, 177–194 (2018).

48. Bahreyni, A. *et al.* A new chemotherapy agent-free theranostic system composed of graphene oxide nano-complex and aptamers for treatment of cancer cells. *Int. J. Pharm.* **526**, 391–399 (2017).

49. Su, Y. *et al.* Impermeable barrier films and protective coatings based on reduced graphene oxide. *Nat. Commun.* **5**, 1–5 (2014).

50. Berry, V. Impermeability of graphene and its applications. *Carbon* **62**, 1–10 (2013).

51. Chen, S. *et al.* Oxidation Resistance of Graphene-Coated Cu and Cu/Ni Alloy. *ACS Nano* **5**, 1321–1327 (2011).

52. Krishnamurthy, A. *et al.* Passivation of microbial corrosion using a graphene coating. *Carbon* **56**, 45–49 (2013).

53. Chang, C.-H. *et al.* Novel anticorrosion coatings prepared from polyaniline/graphene composites. *Carbon* **50**, 5044–5051 (2012).

54. Yu, Y.-H., Lin, Y.-Y., Lin, C.-H., Chan, C.-C. & Huang, Y.-C. High-performance polystyrene/graphene-based nanocomposites with excellent anti-corrosion properties. *Polym Chem* **5**, 535–550 (2014).

55. Ghany, N. A. A., Elsherif, S. A. & Handal, H. T. Revolution of Graphene for different applications: State-of-the-art. *Surf. Interfaces* **9**, 93–106 (2017).

56. Wu, X., Mu, F., Wang, Y. & Zhao, H. Application of atomic simulation methods on the study of graphene nanostructure fabrication by particle beam irradiation: A review. *Comput. Mater. Sci.* **149**, 98–106 (2018).

57. Eizenberg, M., & Blakely, J. M. Carbon monolayer phase condensation on Ni(111) *Surface Science* **82**, 228–236 (1979).

58. Aizawa, T., Souda, R., Otani, S., Ishizawa, Y. & Oshima, C. Anomalous bond of monolayer graphite on transition-metal carbide surfaces. *Phys. Rev. Lett.* **64**, 768–771 (1990).

59. Yazdi, G. R., Iakimov, T. & Yakimova, R. Epitaxial Graphene on SiC: A Review of Growth and Characterization. *Crystals* **6**, 53 (2016).

60. Zhang, Y., Zhang, L. & Zhou, C. Review of Chemical Vapor Deposition of Graphene and Related Applications. *Acc. Chem. Res.* **46**, 2329–2339 (2013).

61. Li, X. *et al.* Large-Area Synthesis of High-Quality and Uniform Graphene Films on Copper Foils. *Science* **324**, 1312–1314 (2009).

62. Berger, C. *et al.* Ultrathin epitaxial graphite: 2D electron gas properties and a route toward graphene-based nanoelectronics. *J. Phys. Chem. B* **108**, 19912–19916 (2004).

63. Mattevi, C., Kim, H. & Chhowalla, M. A review of chemical vapour deposition of graphene on copper. *J Mater Chem* **21**, 3324–3334 (2011).

64. Ago, H. *et al.* Epitaxial Chemical Vapor Deposition Growth of Single-Layer Graphene over Cobalt Film Crystallized on Sapphire. *ACS Nano* **4**, 7407–7414 (2010).

65. Strupinski, W. *et al.* Graphene Epitaxy by Chemical Vapor Deposition on SiC. *Nano Lett.* **11**, 1786–1791 (2011).

66. Hu, B. *et al.* Epitaxial growth of large-area single-layer graphene over Cu(111)/sapphire by atmospheric pressure CVD. *Carbon* **50**, 57–65 (2012).

67. Novoselov, K. S. *et al.* Two-dimensional atomic crystals. *Proc. Natl. Acad. Sci.* **102**, 10451–10453 (2005).

68. Coleman, J. N. Liquid Exfoliation of Defect-Free Graphene. *Acc. Chem. Res.* **46**, 14–22 (2013).

69. Van Bommel, A. J., Crombeen, J. E. & Van Tooren, A. LEED and Auger electron observations of the SiC(0001) surface. *Surf. Sci.* **48**, 463–472 (1975).

70. Owman, F. & Mårtensson, P. The SiC(0001)6√3 × 6√3 reconstruction studied with STM and LEED. *Surf. Sci.* **369**, 126–136 (1996).

71. Li, L. & Tsong, I. S. T. Atomic structures of 6H SiC (0001) and (0001̄) surfaces. *Surf. Sci.* **351**, 141–148 (1996).

72. Forbeaux, I., Themlin, J.-M., Charrier, A., Thibaudau, F. & Debever, J.-M. Solid-state graphitization mechanisms of silicon carbide 6H–SiC polar faces. *Appl. Surf. Sci.* **162–163**, 406–412 (2000).

73. de Heer, W. A. *et al.* Epitaxial graphene. *Solid State Commun.* **143**, 92–100 (2007).

74. Yakimova, R. *et al.* Analysis of the Formation Conditions for Large Area Epitaxial Graphene on SiC Substrates. *Materials Science Forum* vols 645–648 565–568 /MSF.645-648.565 (2010).

75. Virojanadara, C. *et al.* Homogeneous large-area graphene layer growth on $6H$-SiC(0001). *Phys. Rev. B* **78**, 245403 (2008).

76. Niyogi, S. *et al.* Solution Properties of Graphite and Graphene. *J. Am. Chem. Soc.* **128**, 7720–7721 (2006).

77. Novoselov, K. S. *et al.* Two-dimensional gas of massless Dirac fermions in graphene. *Nature* **438**, 197–200 (2005).

78. Yi, M. & Shen, Z. A review on mechanical exfoliation for the scalable production of graphene. *J. Mater. Chem. A* **3**, 11700–11715 (2015).

79. Lomeda, J. R., Doyle, C. D., Kosynkin, D. V., Hwang, W.-F. & Tour, J. M. Diazonium Functionalization of Surfactant-Wrapped Chemically Converted Graphene Sheets. *J. Am. Chem. Soc.* **130**, 16201–16206 (2008).

80. Vallés, C. *et al.* Solutions of Negatively Charged Graphene Sheets and Ribbons. *J. Am. Chem. Soc.* **130**, 15802–15804 (2008).

81. Cravotto, G. & Cintas, P. Sonication-Assisted Fabrication and Post-Synthetic Modifications of Graphene-Like Materials. *Chem. – Eur. J.* **16**, 5246–5259 (2010).

82. Hernandez, Y. *et al.* High-yield production of graphene by liquid-phase exfoliation of graphite. *Nat. Nanotechnol.* **3**, 563–568 (2008).

83. Blake, P. *et al.* Graphene-Based Liquid Crystal Device. *Nano Lett.* **8**, 1704–1708 (2008).

84. Bourlinos, A. B., Georgakilas, V., Zboril, R., Steriotis, T. A. & Stubos, A. K. Liquid-Phase Exfoliation of Graphite Towards Solubilized Graphenes. *Small* **5**, 1841–1845 (2009).

85. Bourlinos, A. B. *et al.* Aqueous-phase exfoliation of graphite in the presence of polyvinylpyrrolidone for the production of water-soluble graphenes. *Solid State Commun.* **149**, 2172–2176 (2009).

86. De, S. *et al.* Flexible, Transparent, Conducting Films of Randomly Stacked Graphene from Surfactant-Stabilized, Oxide-Free Graphene Dispersions. *Small* **6**, 458–464 (2010).

87. Carrasco, P. M. *et al.* High-concentration aqueous dispersions of graphene produced by exfoliation of graphite using cellulose nanocrystals. *Carbon* **70**, 157–163 (2014).

88. Stankovich, S. *et al.* Graphene-based composite materials. *Nature* **442**, 282–286 (2006).

89. Hu, K., Kulkarni, D. D., Choi, I. & Tsukruk, V. V. Graphene-polymer nanocomposites for structural and functional applications. *Prog. Polym. Sci.* **39**, 1934–1972 (2014).

90. Wei, W., Jian, N. Direct exfoliation of graphene in organic solvents with addition of NaOH. *Chem. comm.* **24**, 6888-6890 (2011).

91. O'Neill, A., Khan, U., Nirmalraj, P. N., Boland, J. & Coleman, J. N. Graphene Dispersion and Exfoliation in Low Boiling Point Solvents. *J. Phys. Chem. C* **115**, 5422–5428 (2011).

92. Oh, S. Y., Kim, S. H., Chi, Y. S. & Kang, T. J. Fabrication of oxide-free graphene suspension and transparent thin films using amide solvent and thermal treatment. *Appl. Surf. Sci.* **258**, 8837–8844 (2012).

93. Du, W., Lu, J., Sun, P., Zhu, Y. & Jiang, X. Organic salt-assisted liquid-phase exfoliation of graphite to produce high-quality graphene. *Chem. Phys. Lett.* **568–569**, 198–201 (2013).

94. Lotya, M. *et al.* Liquid Phase Production of Graphene by Exfoliation of Graphite in Surfactant/Water Solutions. *J. Am. Chem. Soc.* **131**, 3611–3620 (2009).

95. Guardia, L. *et al.* High-throughput production of pristine graphene in an aqueous dispersion assisted by non-ionic surfactants. *Carbon* **49**, 1653–1662 (2011).

96. Zhang, M. *et al.* Production of Graphene Sheets by Direct Dispersion with Aromatic Healing Agents. *Small* **6**, 1100–1107 (2010).

97. Lotya, M., King, P., Khan, U., De, S., and Coleman, J., High-Concentration, Surfactant-Stabilized Graphene Dispersions. *ACS Nano*. **4**, 3155-3163 (2010)

98. Bang, G. S., So, H.-M., Lee, M. J. & Ahn, C. W. Preparation of graphene with few defects using expanded graphite and rose bengal. *J. Mater. Chem.* **22**, 4806–4810 (2012).

99. An, X. *et al.* Stable Aqueous Dispersions of Noncovalently Functionalized Graphene from Graphite and their Multifunctional High-Performance Applications. *Nano Lett.* **10**, 4295–4301 (2010).

100. Sampath, S. *et al.* Direct Exfoliation of Graphite to Graphene in Aqueous Media with Diazaperopyrenium Dications. *Adv. Mater.* **25**, 2740–2745 (2013).

101. Liu, Y. *et al.* Solution Adsorption Formation of a π-Conjugated Polymer/Graphene Composite for High-Performance Field-Effect Transistors. *Adv. Mater.* **30**, 1705377 (2018).

102. Wajid, A. S. *et al.* Polymer-stabilized graphene dispersions at high concentrations in organic solvents for composite production. *Carbon* **50**, 526–534 (2012).

103. Becerril, H. A. *et al.* Evaluation of Solution-Processed Reduced Graphene Oxide Films as Transparent Conductors. *ACS Nano* **2**, 463–470 (2008).

104. Hirata, M., Gotou, T., Horiuchi, S., Fujiwara, M. & Ohba, M. Thin-film particles of graphite oxide 1:: High-yield synthesis and flexibility of the particles. *Carbon* **42**, 2929–2937 (2004).

105. Kim, J., Cote, L. J. & Huang, J. Two Dimensional Soft Material: New Faces of Graphene Oxide. *Acc. Chem. Res.* **45**, 1356–1364 (2012).

106. Li, D., Müller, M. B., Gilje, S., Kaner, R. B. & Wallace, G. G. Processable aqueous dispersions of graphene nanosheets. *Nat. Nanotechnol.* **3**, 101–105 (2008).

107. Luo, J. *et al.* Graphene Oxide Nanocolloids. *J. Am. Chem. Soc.* **132**, 17667–17669 (2010).

108. Cote, L. J. *et al.* Graphene oxide as surfactant sheets. *Pure Appl. Chem.* **83**, 95–110 (2010).

109. Furtado, C. A. *et al.* Debundling and Dissolution of Single-Walled Carbon Nanotubes in Amide Solvents. *J. Am. Chem. Soc.* **126**, 6095–6105 (2004).

110. Giordani, S. *et al.* Debundling of Single-Walled Nanotubes by Dilution: Observation of Large Populations of Individual Nanotubes in Amide Solvent Dispersions. *J. Phys. Chem. B* **110**, 15708–15718 (2006).

111. Hasan, T. *et al.* Stabilization and "Debundling" of Single-Wall Carbon Nanotube Dispersions in N-Methyl-2-pyrrolidone (NMP) by Polyvinylpyrrolidone (PVP). *J. Phys. Chem. C* **111**, 12594–12602 (2007).

112. Hernandez, Y., Lotya, M., Rickard, D., Bergin, S. D. & Coleman, J. N. Measurement of Multicomponent Solubility Parameters for Graphene Facilitates Solvent Discovery. *Langmuir* **26**, 3208–3213 (2010).

113. Khan, U., O'Neill, A., Lotya, M., De, S. & Coleman, J. N. High-Concentration Solvent Exfoliation of Graphene. *Small* **6**, 864–871 (2010).

114. May, P., Khan, U., Hughes, J. M. & Coleman, J. N. Role of Solubility Parameters in Understanding the Steric Stabilization of Exfoliated Two-Dimensional Nanosheets by Adsorbed Polymers. *J. Phys. Chem. C* **116**, 11393–11400 (2012).

115. Xu, L. *et al.* Production of High-Concentration Graphene Dispersions in Low-Boiling-Point Organic Solvents by Liquid-Phase Noncovalent Exfoliation of Graphite with a Hyperbranched Polyethylene and Formation of Graphene/Ethylene Copolymer Composites. *J. Phys. Chem. C* **117**, 10730–10742 (2013).

116. Nishio, M., Hirota, M. & Umezawa, Y. *The CH/π Interaction: Evidence, Nature, and Consequences*. (John Wiley & Sons, 1998).

117. Rubinstein, M. & Colby, R. H. *Polymer physics*. (Oxford Univ. Press, 2010).

118. Silberberg, A. Adsorption of Flexible Macromolecules. IV. Effect of Solvent–Solute Interactions, Solute Concentration, and Molecular Weight. *J. Chem. Phys.* **48**, 2835–2851 (1968).

119. Conway, B. E. *Electrochemical Supercapacitors: Scientific Fundamentals and Technological Applications*. (Springer Science & Business Media, 2013).

120. Wang, C. *et al.* Advanced Carbon for Flexible and Wearable Electronics. *Adv. Mater.* **31**, 1801072 (2019).

121. Burke, A. & Zhao, H. Applications of Supercapacitors in Electric and Hybrid Vehicles. 15 (2015).

122. Conway, B. E. Electrochemistry Encyclopedia: Electrochemical capacitors. (Chemistry Department, University of ottawa, 2003)

123. Zhang, L. L. & Zhao, X. S. Carbon-based materials as supercapacitor electrodes. *Chem. Soc. Rev.* **38**, 2520–2531 (2009).

124. Frackowiak, E., Khomenko, V., Jurewicz, K., Lota, K. & Béguin, F. Supercapacitors based on conducting polymers/nanotubes composites. *J. Power Sources* **153**, 413–418 (2006).

125. Lee, S. W., Kim, B.-S., Chen, S., Shao-Horn, Y. & Hammond, P. T. Layer-by-Layer Assembly of All Carbon Nanotube Ultrathin Films for Electrochemical Applications. *J. Am. Chem. Soc.* **131**, 671–679 (2009).

126. Ike, I. S., Sigalas, I. & Iyuke, S. Understanding performance limitation and suppression of leakage current or self-discharge in electrochemical capacitors: a review. *Phys. Chem. Chem. Phys.* **18**, 661–680 (2016).

127. Zhang, L. L., Zhou, R. & Zhao, X. S. Graphene-based materials as supercapacitor electrodes. *J. Mater. Chem.* **20**, 5983 (2010).

128. Xia, J., Chen, F., Li, J. & Tao, N. Measurement of the quantum capacitance of graphene. *Nat. Nanotechnol.* **4**, 505–509 (2009).

129. Graphene-Based Supercapacitor with an Ultrahigh Energy Density | Nano Letters. https://pubs-acs-org.docelec.insa-lyon.fr/doi/abs/10.1021/nl102661q.

130. Xu, B. *et al.* What is the choice for supercapacitors: graphene or graphene oxide? *Energy Environ. Sci.* **4**, 2826 (2011).

131. Zhang, X. *et al.* Mechanically strong and highly conductive graphene aerogel and its use as electrodes for electrochemical power sources. *J. Mater. Chem.* **21**, 6494 (2011).

132. Stoller, M. D., Park, S., Zhu, Y., An, J. & Ruoff, R. S. Graphene-Based Ultracapacitors. *Nano Lett.* **8**, 3498–3502 (2008).

133. Wang, Y. *et al.* Supercapacitor Devices Based on Graphene Materials. *J. Phys. Chem. C* **113**, 13103–13107 (2009).

134. Sun, Y. & Shi, G. Graphene/polymer composites for energy applications. *J. Polym. Sci. Part B Polym. Phys.* **51**, 231–253 (2013).

135. Zhang, X. & Samorì, P. Graphene/Polymer Nanocomposites for Supercapacitors. *ChemNanoMat* **3**, 362–372 (2017).

136. Zhang, X. *et al.* Supramolecular Chemistry on Graphene Field-Effect Transistors. *Small* **10**, 1735–1740 (2014).

137. Kumar, N. A. *et al.* Polyaniline-Grafted Reduced Graphene Oxide for Efficient Electrochemical Supercapacitors. *ACS Nano* **6**, 1715–1723 (2012).

138. Zhang, B. *et al.* Conjugated Polymer-Grafted Reduced Graphene Oxide for Nonvolatile Rewritable Memory. *Chem. – Eur. J.* **17**, 13646–13652 (2011).

139. Wang, D.-W. *et al.* Fabrication of Graphene/Polyaniline Composite Paper via In Situ Anodic Electropolymerization for High-Performance Flexible Electrode. *ACS Nano* **3**, 1745–1752 (2009).

140. Wu, Q., Xu, Y., X., Yao, Z., Y., Liu, A., & Shi, G., Q. Supercapacitors Based on Flexible Graphene/Polyaniline Nanofiber Composite Films. *ACS Nano*. **4**, 1963-1970 (2010)

141. Lai, L. *et al.* Preparation of Supercapacitor Electrodes through Selection of Graphene Surface Functionalities. *ACS Nano* **6**, 5941–5951 (2012).

142. Xu, J., Wang, K., Zu, S.-Z., Han, B.-H. & Wei, Z. Hierarchical Nanocomposites of Polyaniline Nanowire Arrays on Graphene Oxide Sheets with Synergistic Effect for Energy Storage. *ACS Nano* **4**, 5019–5026 (2010).

143. Lai, L. *et al.* Tuning graphene surface chemistry to prepare graphene/polypyrrole supercapacitors with improved performance. *Nano Energy* **1**, 723–731 (2012).

144. Zhao, Y. *et al.* Highly Compression-Tolerant Supercapacitor Based on Polypyrrole-mediated Graphene Foam Electrodes. *Advanced Materials* **4**, 25 (2012)

145. Zhu, C., Zhai, J., Wen, D. & Dong, S. Graphene oxide/polypyrrole nanocomposites: one-step electrochemical doping, coating and synergistic effect for energy storage. *J. Mater. Chem.* **22**, 6300–6306 (2012).

146. Yang, X. *et al.* Three-Dimensional Macroporous Polypyrrole-Derived Graphene Electrode Prepared by the Hydrogen Bubble Dynamic Template for Supercapacitors and Metal-Free Catalysts. *ACS Appl. Mater. Interfaces* **7**, 23731–23740 (2015).

147. Meng, Y., Wang, K., Zhang, Y. & Wei, Z. Hierarchical Porous Graphene/Polyaniline Composite Film with Superior Rate Performance for Flexible Supercapacitors. *Adv. Mater.* **25**, 6985–6990 (2013).

148. Park, J. W. *et al.* In Situ Synthesis of Graphene/Polyselenophene Nanohybrid Materials as Highly Flexible Energy Storage Electrodes. *Chem. Mater.* **26**, 2354–2360 (2014).

149. Weng, Z. *et al.* Graphene–Cellulose Paper Flexible Supercapacitors. *Adv. Energy Mater.* **1**, 917–922 (2011).

150. Ye, S., Feng, J. & Wu, P. Highly elastic graphene oxide–epoxy composite aerogels via simple freeze-drying and subsequent routine curing. *J. Mater. Chem. A* **1**, 3495 (2013).

151. Chen, S. *et al.* Conductive, tough, hydrophilic poly(vinyl alcohol)/graphene hybrid fibers for wearable supercapacitors. *J. Power Sources* **319**, 271–280 (2016).

152. Theophile, N. & Jeong, H. K. Electrochemical properties of poly(vinyl alcohol) and graphene oxide composite for supercapacitor applications. *Chem. Phys. Lett.* **669**, 125–129 (2017).

153. Fard, H. N., Pour, G. B., Sarvi, M. N. & Esmaili, P. PVA-based supercapacitors. *Ionics* **25**, 2951–2963 (2019).

154. Pawar, P. B., Shukla, S. & Saxena, S. Graphene oxide – Polyvinyl alcohol nanocomposite based electrode material for supercapacitors. *J. Power Sources* **321**, 102–105 (2016).

155. Marka, S. K., Mohiddon, Md. A., Prasad, M. D. & Srikanth, V. V. S. S. Growth of MgO on multi-layered graphene and Mg in PVA matrix. *Superlattices Microstruct.* **83**, 530–537 (2015).

156. Cai, D. & Song, M. Recent advance in functionalized graphene/polymer nanocomposites. *J. Mater. Chem.* **20**, 7906 (2010).

157. Xu, Y., Hong, W., Bai, H., Li, C. & Shi, G. Strong and ductile poly(vinyl alcohol)/graphene oxide composite films with a layered structure. *Carbon* **47**, 3538–3543 (2009).

158. Liu, H., Bandyopadhyay, P., Kim, N. H., Moon, B. & Lee, J. H. Surface modified graphene oxide/poly(vinyl alcohol) composite for enhanced hydrogen gas barrier film. *Polym. Test.* **50**, 49–56 (2016).

159. Cano, M. *et al.* Improving the mechanical properties of graphene oxide based materials by covalent attachment of polymer chains. *Carbon* **52**, 363–371 (2013).

160. Liang, J. *et al.* Molecular-Level Dispersion of Graphene into Poly(vinyl alcohol) and Effective Reinforcement of their Nanocomposites. *Adv. Funct. Mater.* **19**, 2297–2302 (2009).

161. Lima, T. B. S., Silva, V. O., Araujo, E. S. & Araujo, P. L. B. Polymer Nanocomposites of Surface-Modified Graphene. I: Thermal and Electrical Properties of Poly(Vinyl Alcohol)/Aminoacid-Functionalized Graphene. *Macromol. Symp.* **383**, 1800051 (2019).

162. Wei, N. *et al.* Superelastic active graphene aerogels dried in natural environment for sensitive supercapacitor-type stress sensor. *Electrochimica Acta* **283**, 1390–1400 (2018).

163. Frackowiak, E, Carbon materials for supercapacitor application. *Phys. Chem. Chem. Phys.*, 9(15), 1774-85 (2007).

Chapter 2

Experimental methodology

This chapter gathers all specific method that we have carried out within this thesis. First of all, samples preparation process will be illustrated, including PVA solution preparation, oxidation of graphite, liquid-phase exfoliation of bulk graphite and graphite oxide in PVA solution, preparation of PVA/GO aerogels via freeze drying method, and preparation of electrode materials. Secondly, the information of relative materials and equipment will be displayed. Thirdly, all characterization techniques applied in graphene-based nanosheets will be carefully explained, and electrochemical measurements for our materials will be illustrated.

2.1 Preparation of samples

2.1.1 Introduction of liquid-phase exfoliation process

Liquid-phase exfoliation (LPE) of pristine graphite or graphite oxide in polymer solution is carried out according to the following steps: a) addition of the pristine graphite or graphite oxide in a polymer solution; b) ultrasonication of the mixture for a period; c) centrifugation of the as-obtained mixture to get homogeneous graphene or GO dispersion. Figure 2.1 shows the process scheme of liquid-phase exfoliation used in this thesis.
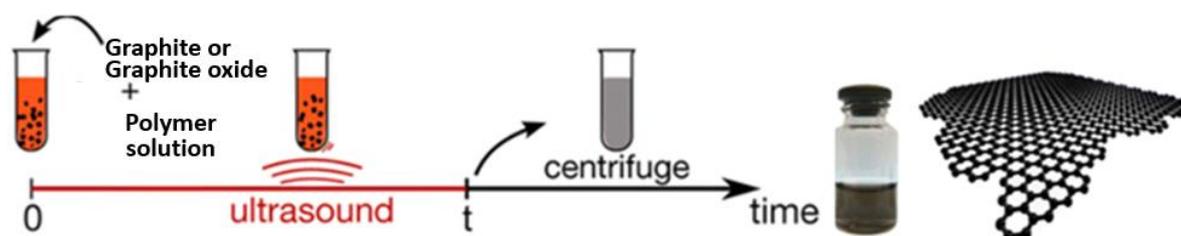
Figure 2.1 | Process scheme of liquid phase exfoliation

2.1.2 PVA solution preparation

Three molar weights of PVA, PVA1 (130000 g/mol), PVA2 (31000-50000 g/mol), and PVA3 (13000-23000 g/mol) are dissolved according to various concentrations in distilled water and stirred at 80 ^{o}C for 4 hours. The studied concentration distribution of these three PVA solutions are shown in Table 2.1.

Table 2.1 The concentration distribution of three PVA solutions

Samples	Concentration distribution (mg/mL)												
PVA1	0	0.05	0.15	0.25	0.3	0.5	1.25	2.5	5.0	7.5	10.0	12.5	20.0
PVA2	0	0.25	0.5	1.0	1.5	2.0	5.0	10.0	15.0	20.0	25.0	30.0	40.0
PVA3	0	0.25	0.5	1.25	2.5	5.0	10.0	15.0	37.5	45.0	60.0	67.5	75.0

All three PVA solutions with different concentrations will be used in Chapter 3, and only PVA1 solution with different concentrations will be used in Chapter 4 and Chapter 5.

2.1.3 Preparation of graphite oxide with different oxygen content

3g of pristine graphite flakes are mixed with 75mL of concentrated H_2SO_4 (98%) into a 250 mL beaker. $KMnO_4$, with required amount of 0.75 g or 9 g is gradually added into the mixture kept at low temperature (< 10 ^{o}C) in an ice bath. Then, the obtained dark green suspension is continuously stirred at 35 ^{o}C for 2 hours. Then 75 mL of deionized water are added to the suspension under vigorous stirring, the dark green mixture got fuchsia. Finally, 7.5 mL of 35% aq. H_2O_2 is added to finish the reaction, leading the mixture turns to a brown/yellowish color. [1] To remove impurity ions, the resulting graphite oxide (GO) is washed two or three times as follows: a) HCl at 30% v/v, b) deionized water, c) ethanol. [2] Finally, GO slurry is obtained after centrifugation to remove excess water. In this study, two GOs with different oxidation degree are obtained by using different ratio of graphene: $KMnO_4$ =1:4 and 3:1, named GO1, and GO2 respectively. The weight percent of GO1 and GO2 in slurry are calculated as 35 wt.% for GO1 and 9 wt.% for GO2. Figure 2.2 displays the scheme of preparation of GO slurry.
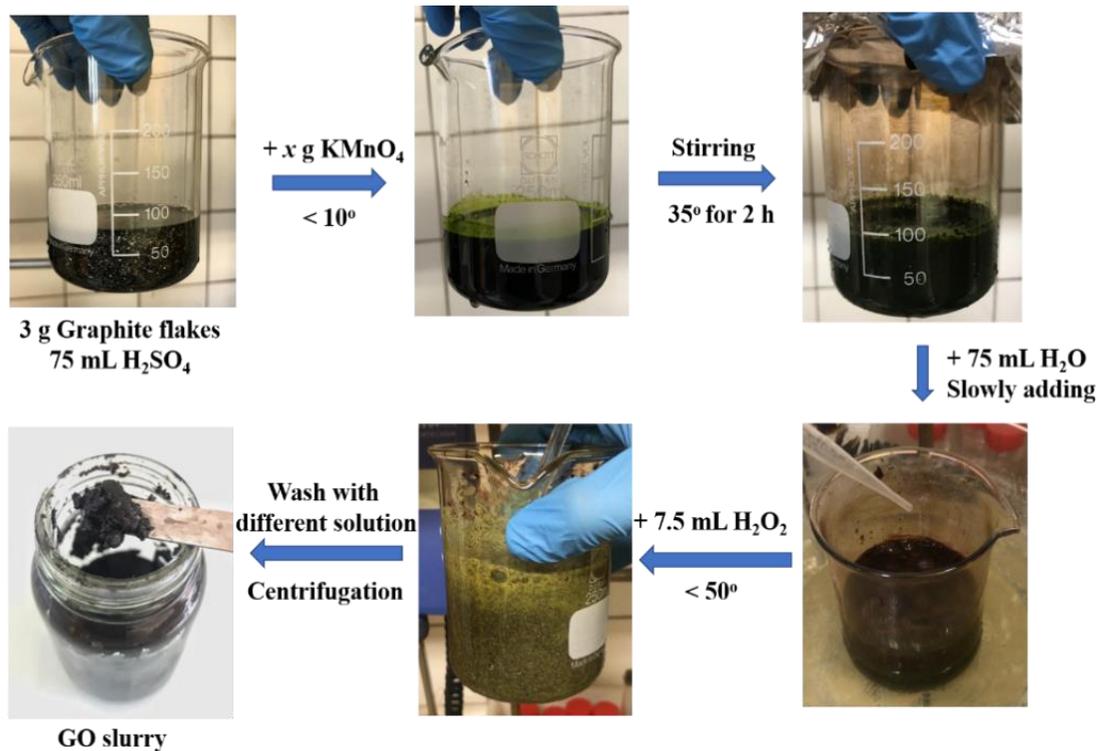
Figure 2.2 | Scheme of preparation of GO slurry

2.1.4 Liquid-phase exfoliation of pristine graphite and graphite oxide in PVA/ water solution

a) Exfoliation of raw graphite in three PVA solutions

Pristine graphite flakes, with a ratio of 4.5 mg/mL, are added into the three PVA/water solution with different concentrations. These ternary mixtures are sonicated in a sonic water bath at 40 °C (±2 °C) for 24 h. Moreover, the sonication duration was extended up to 1 week and measure of the concentration of the exfoliated solution was done every 24 h. Then, the suspension is transferred into centrifuge tube, and centrifuged at 1500 RMP for 90 min. Finally, the supernatants (top two thirds of the centrifuged dispersion) are carefully collected and further diluted (10, 20 or 50 times) to facilitate the comparison and the measurement. Because of unaverage energy distribution in the sonic bath, all samples are repeated several times, finally, the solution with highest dispersion concentration are recorded.

b) Exfoliation of graphite oxide in PVA solutions

To reduce the exfoliation time and increase its efficiency, in chapter 4 a sonic tip is employed to exfoliate GO. GO1 and GO2 (4.5 mg/mL) are added into PVA solutions (only PVA1 is used in this chapter), then mixtures are sonicated using a sonic tip at ~40 $^{\circ}$C for 30 minutes. Pristine graphite (PG) without any oxidation is also used using the same process as reference. The suspension is then transferred into centrifuge tubes and centrifuged at 1500 RMP for 90 min to obtain a stabilized dispersion. Finally, the obtained suspensions are diluted with 5 times to facilitate the comparison and the characterization.

2.1.5 Preparation of PVA/ GO2 hybrid aerogels by freeze drying process

A series of PVA/GO2 mixtures are prepared with different concentration of PVA: 0, 0.05, 0.15, 0.25, 0.3, 0.5, 1.0, 1.25, 2.5, 5.0, 7.5, 10.0, and 12.5 mg/mL, still using GO2 at 4.5 mg/mL and PVA1. Those solutions are first frozen in a refrigerator at -80 $^{\circ}$C for 12h, the frozen samples are then freeze-dried in a lyophilizer at -200 $^{\circ}$C for three days. The PVA/GO2 aerogels with different mass ratio are obtained. Based on the different content of PVA, they are named as pure GO2, 0.05PVA/GO2, 0.15PVA/GO2, 0.25PVA/GO2, 0.3PVA/GO2, 0.5PVA/GO2, 1.0PVA/GO2, 1.25PVA/GO2, 2.5PVA/GO2, 5.0PVA/GO2, 7.5PVA/GO2, 10.0PVA/GO2, and 12.5PVA/GO2.

2.1.6 Preparation of electrode

Firstly, we carefully weigh the 1 mg of sample, and press it into Ni foam current collector. For this step, we press it using a small mold in our lab, which can manually control the compression force. Otherwise, you can press it by Infrared Press machine with ~5Mpa, which is the most commonly used method for aerogels electrode material preparation. 1 mg is a low mass loading used for a comparison purpose. In order to have better contact of the electrolyte with the electrode material, the Ni foam loaded with the electroactive materials are soaked in a 1M Na_2SO_4 solution overnight.

2.2 Materials and Equipment

2.2.1 Materials

The information of all reagents and materials involved in this thesis are summarized in Table 2.2. The digital photo and SEM image of Nickel foam current collector used are shown in Figure 2.3.

Table 2.2 Information of materials

Name	Parameters	Producer
Raw graphite flakes	12.01 g/mol + 100 mesh	Sigma Aldrich
Polyvinyl Alcohol (PVA)	130000 g/mol 31000-50000 g/mol 13000-23000 g/mol	Sigma Aldrich
Potassium Permanganate	Analysis	CHEMIE-PLUS
Sulfuric Acid	98%, Analysis	CHEMIE-PLUS
Hydrogen Peroxide	35% aq., Analysis	CHEMIE-PLUS
Hydrochloric Acid	36.5-38%, Analysis	CHEMIE-PLUS
Ethanol	Analysis	CHEMIE-PLUS
Sodium Sulfate	Analysis	CHEMIE-PLUS
Nickel Foam	1 mm thickness	Guang Jiayuan New Materials Co., China
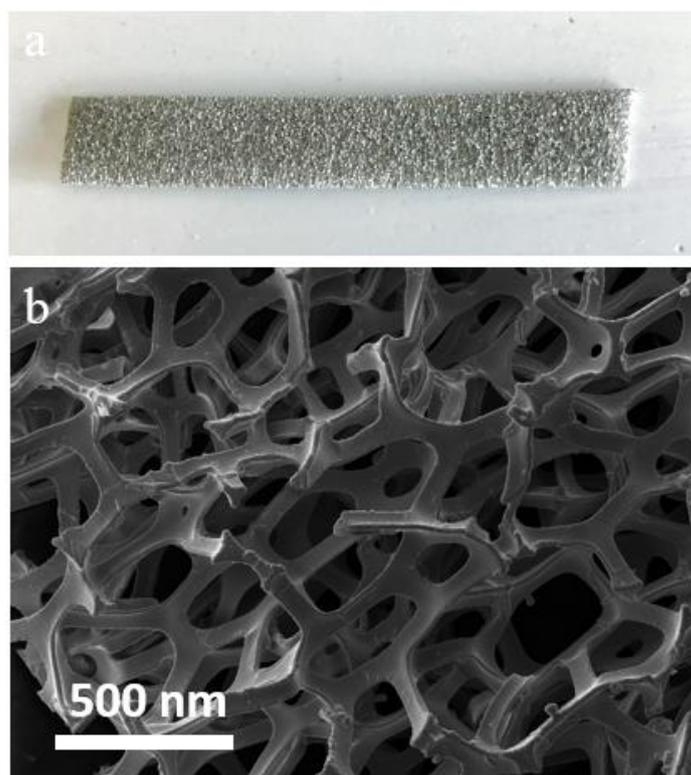
Figure 2.3 | (**a**) Digital photo and (**b**) SEM image of Nickel foam

2.2.2 Equipment

Figure 2.4 presents all equipment, including the sonic bath (Fisherbrand 11201, Thermo Fisher Scientific, USA), the sonic tip (Ultraturrax IKA T25, Thermo Fisher Scientific, USA), the centrifuge machine (Thermo Scientific™ Medifuge™ small benchtop centrifuge, Thermo Fisher Scientific, USA) and lyophilizer (Labconco de 6l , FreeZone 6plus, USA) that we used during the process of samples' preparation.
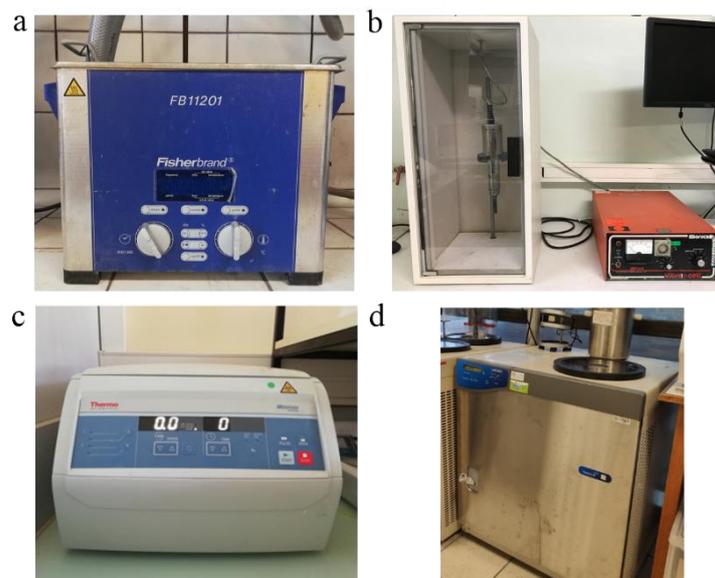
Figure 2.4 | Digital photo of (**a**) the sonic bath, (**b**) the sonic tip, (**c**) the centrifuge machine, and (**d**) lyophilizer

2.3 Structural characterization techniques

The Structural characterization of materials is crucial to investigate their physical and chemical properties. For graphene-based nanosheets (GBN) produced by liquid-phase exfoliation (LPE), it is important to characterize their structure such as domain size of crystal, thickness, number of atomic layers, and elemental composition. A series of techniques have been employed in this thesis, including Scanning Electron Microscope (SEM), Energy Dispersive Spectroscopy (EDS), Transmission Electron Microscope (TEM), X-ray Photoelectron Spectroscopy (XPS), X-ray Diffraction (XRD), Raman spectroscopy, Fourier transform infrared (FTIR) spectroscopy, *etc*. Furthermore, GBN concentration can be estimated using Ultraviolet–visible spectroscopy (UV-Vis) using Beer-Lambert's law.

2.3.1 Electron microscopy

a) Scanning Electron Microscope (SEM)

Scanning Electron Microscope (SEM) is a powerful and versatile tool for material characterization, especially in recent years with the continuous reduced dimension of materials. SEM generates images by scanning a specimen with a focused beam of electrons. The

interaction of high-energy electrons and the specimen produces signals that contain information about the surface topography and its composition.

Energy Dispersive Spectroscopy (EDS) is a standard semi-quantitative analysis technique to determine elemental composition. When the electron beam generated by the SEM system, bombards materials, the production of characteristic X-ray can be analyzed by an energy dispersive spectrometer.

All SEM images and EDS mappings in this thesis are obtained using a ZEISS Supra55 SEM/EDS system (Figure 2.5a). Figure 2.5b and c display pristine graphite falkes and elemental distributions of carbon and oxygen elements. The mapping by red color and by green colore represent corbon and oxygen element, respectively. Samples for SEM are prepared by direct coating on a so-called double sided sticky carbon tape that was deposited on a metal substrate table, and then inserted into the electronic microscope.
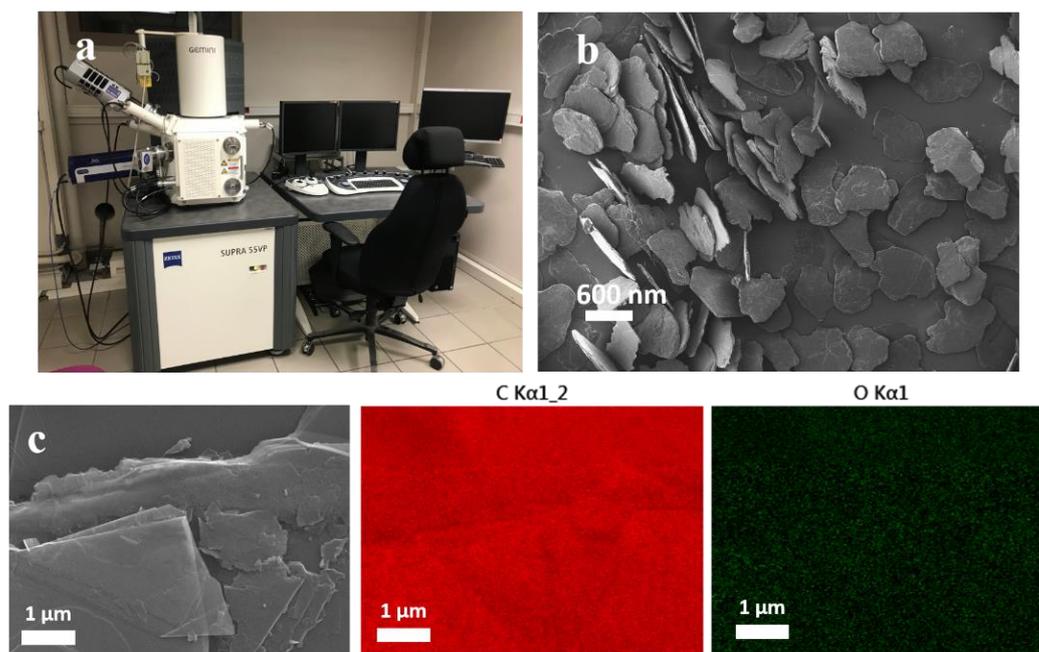
Figure 2.5 | (**a**) Digital photo of SEM/ EDS instrument of a ZEISS Supra55 used in this thesis. (**b**) SEM image of the raw graphite flakes. (**c**) SEM/EDS images of the raw graphite flakes in this thesis

b) Transmission Electron Microscope (TEM)

Transmission Electron Microscope (TEM) is a powerful technique for the microstructure characterization of materials. TEM image is generated by electrons beam transmitting through

an ultrathin sample (less than 100 nm thick) often deposited of a carbon grid. Images provide information about morphology, crystallography and chemical composition of the material over a range of length scale. High-resolution TEM (HRTEM) can analyze the depth of nanosheets down to the atomic dimension and the number of layers, whereas selected area electron diffraction (SAED) can be used to identify nanosheet structures and examine nanosheet defects.

All TEM images are obtained using a Jeol 2010F electron microscope in bright field mode. Samples are prepared by placing a droplet of the solution containing the sample on a 300-mesh holey carbon microscopy grid. The grid is dried overnight and then inserted into the electron microscope. Figure 2.6 shows the TEM instrument of Jeol 2010F electron microscope as well as a typical TEM image and associated electron diffraction pattern recorded on GO2 sample.
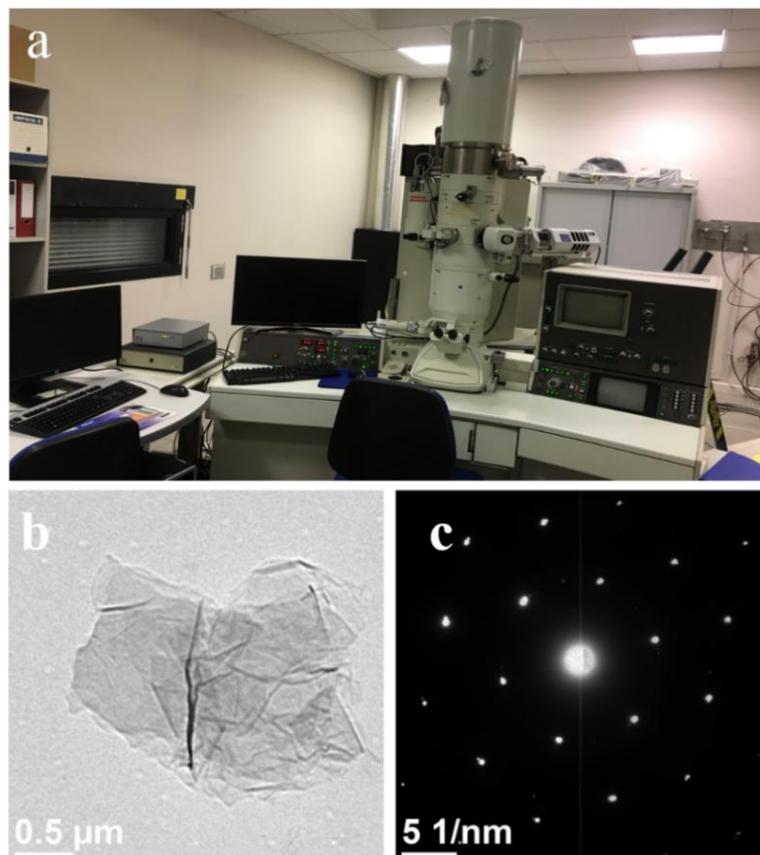
Figure 2.6 | (**a**) Digital photo of TEM instrument of Jeol 2010F electron microscope used in this thesis. (**b**) TEM image of GO2 and (**c**) An electron diffraction pattern from a selected monolayer area of GO2

2.3.2 X-ray Photoelectron Spectroscopy

X-ray photoelectron spectroscopy (XPS) is a surface-sensitive spectroscopic technique that quantitatively provides information about material's elemental composition (empirical formula) as well as the chemical and electronic states of the different elements present within the material. XPS spectra are obtained by irradiating a material with a beam of X-ray while simultaneously measuring the kinetic energy and quantity of the electrons that escape from the material top surface within 0 ~ 10 nm.

Typical full scan spectra of the pristine graphite and corresponding exfoliated graphene are shown in Figure 2.7A. C1s peak at 284.6 eV is considered as intrinsic in-plane crystal structure of graphene. The O1s is ascribed to the adsorbed molecular oxygen on the surface of graphene and graphite. [3] Figure 2.7B presents typical full scan spectra recorded on GO and rGO, and their C1s region spectra that indicate the degree of oxidation corresponding to C atoms in different functional group. [4]
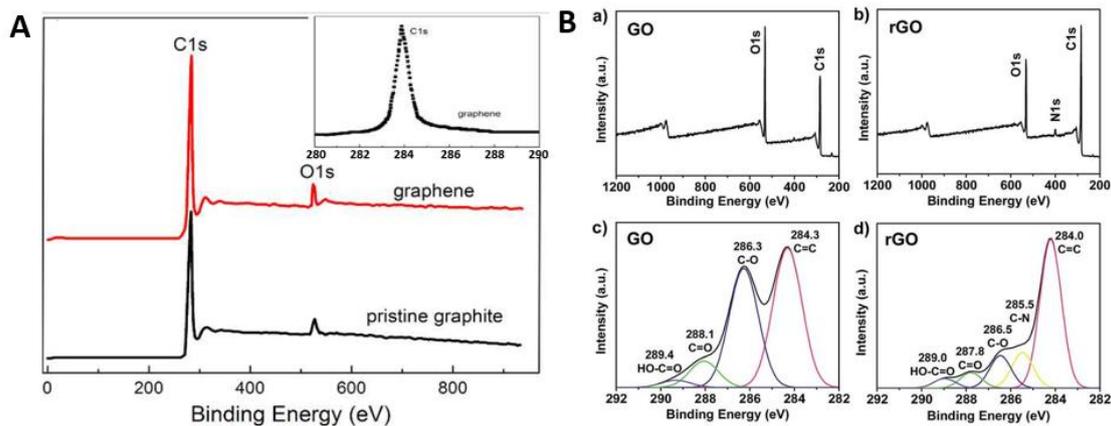
Figure 2.7 | XPS survey spectra of (**A**) pristine graphite and exfoliated graphene, inset is C1s core-level XPS spectrum of graphene.[3] XPS spectra of (**B**) GO and rGO. (**a**) and (**b**) survey XPS spectra: C1s, O1s peaks comely appear, and N1s peak appear after the hydrazine reduction; (**c**) and (**d**) C1s region of XPS spectra: Commonly 4 spectra related to graphitic C=C and functional groups (C-O, C=O, HO-C=O) appear in GO and rGO. Especially in rGO, additional peak with C-N appears due to the use of hydrazine during the reduction process. [4]

A VG 2201 apparatus with an Al K radiation source is used to conduce XPS analyses. (see Figure 2.8) The size of the X-ray probe is adjusted to 200×200 μm². Graphite-based materials are deposited on a steel disk. While analyzing samples, small part of steel disk is also analyzed

at the same time. The C1s and O1s peaks are calibrated by shifting iron oxide peaks from an O1s peak to 530.0 eV. [5] The same analysis is repeated but without the steel disk to ensure that all signals come from the sample. Since the major C1s peak is found at the same binding energy during both analyses before calibration, the C1s positions after calibration should be the same. The take-off angle is fixed at 45°.

Figure 2.8 | XPS instrument used in this thesis

2.3.3 X-ray Diffraction

X-ray Diffraction (XRD) is a powerful nondestructive technique for characterizing material's crystallinity, which provides information about structures, crystalline phases, preferred crystal orientations, and crystallite size. XRD peaks are generated by the constructive interference of a monochromatic beam of X-ray scattered at specific angles with each set of lattice planes in a sample. Figure 2.9 illustrates how the diffraction of X-rays by crystal planes allows to deduce lattice spacings by using the Bragg's law.

$$n\lambda = 2d \sin\theta$$
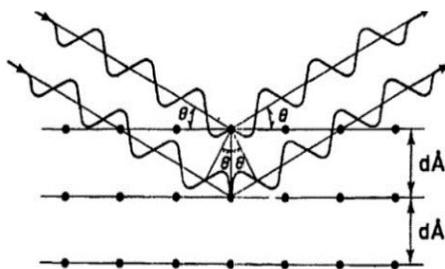
Figure 2.9 | Schematic representation of Bragg's law

In this law, n is an integer called the order of reflection, λ is the wavelength of X-rays, d is the characteristic spacing between the crystal planes of a given specimen and θ is the angle between the incident beam and the normal to the reflecting lattice plane. By measuring the incident angle, θ, under which the constructively interfering x-rays leave the crystal, the interplanar spacing, d, of each single crystallographic phase can be determined. [6,7]

The powder XRD patterns of natural graphite, GO and rGO are presented in Figure 2.10a.[8] Generally the natural graphite shows a basal reflection peak (002) at $2\theta = 26.6°$ which reflects graphite's hexagonal structure. For GO powders, 2θ peak can be seen to be shift to $2\theta = 11°$, meaning a full oxidization of graphite. Besides, a broad peak in the range of 17-24° corresponds to the oxygen-containing groups produced between the GO sheets. After a reduction treatment, a weaker intensity peak in the range of 17-24° of the rGO can be attributed to that the $\pi-$conjugated structure of graphene has been stacked considerably.

All XRD patterns in this thesis are performed using a Bruker D8 advance instrument with a Lynx Eye high speed detector, (Figure 2.10b). This equipment uses a Cu-Kα radiation of 0.15406 nm. Samples (flakes or powder) are simply deposited into the hollow part of a sample holder and the excess of powder is removed by using a glass slide or a razor blade to smooth the upper face. Then the sample is put into the machine.
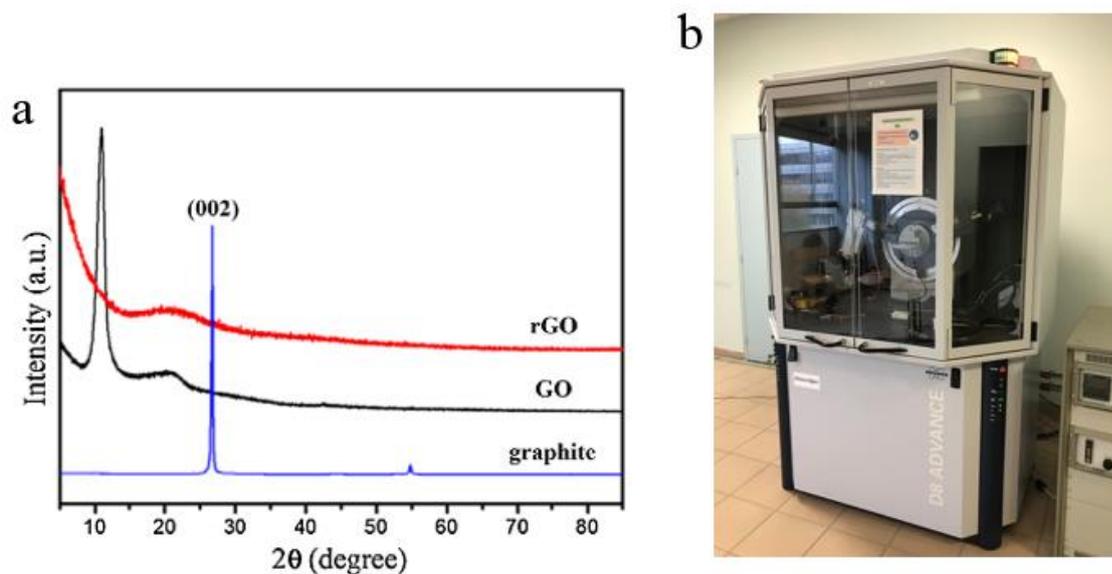
Figure 2.10 | (**a**) X-ray diffraction of natural graphite, GO, and rGO. [8] And (**b**) XRD instrument of Bruker D8 advance used in this thesis

2.3.4 Raman spectroscopy

Raman spectroscopy is a spectroscopic technique typically used to identify the inter- and intramolecular bonds within a material. It produces peaks showing the intensity and Raman shift of the scattered light.

Raman spectroscopy is sensitive for the disorder and defects in graphite and its derivatives. For carbon-based materials, the G bond at ~1600 cm^{-1} is common for all sp^2 of C and the D bond at ~1360 cm^{-1} is common for all defects induced by oxidation. The intensity ratio of D bond and G bond (I_D/I_G) determinates the quality of graphite. Figure 2.11 shows Raman spectra of natural graphite GO and rGO. I_D/I_G ratio increases from 0.7 (graphite) to 1.03 (GO). After a reduction step, the D bond intensity is reduced, reaching 0.93 in rGO, which indicates the removal of partial oxygen containing groups. [9]

Raman spectra are recorded at a room temperature with a Horiba Labram aramis using a wavelength at 473nm as excitation sources, focused through a 50 X objective to give a laser spot of around 2 µm. Samples are simply deposited on an appropriate holder and directly analyzed by Raman spectroscopy.
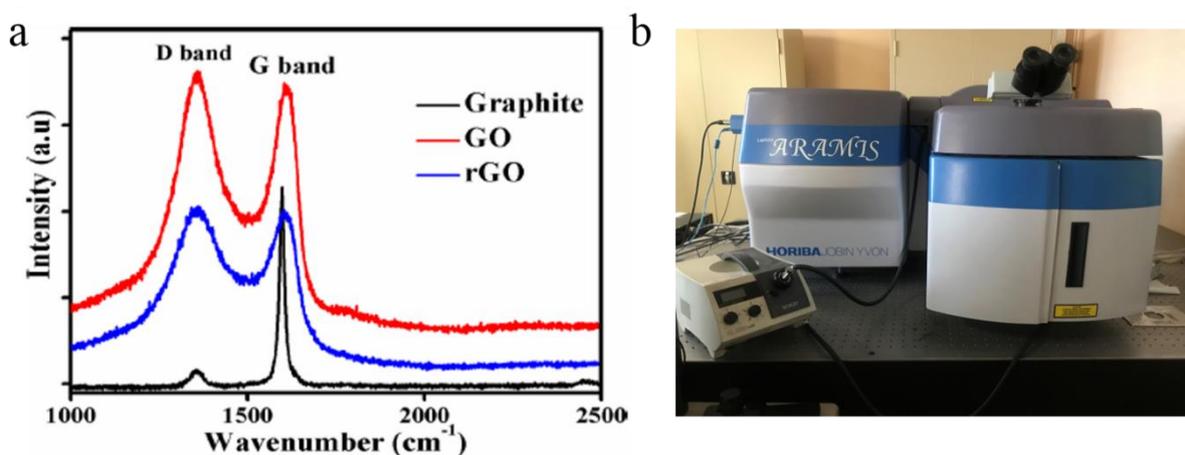
Figure 2.11 | (a) Raman spectra of graphite, GO, and rGO [9] and (**b**) a digital photo of Raman spectrometer Horiba Labram aramis used in this thesis.

2.3.5 Fourier transform infrared (FTIR) spectroscopy

Fourier transform infrared (FTIR) spectroscopy is a technique used to measure the interaction of IR radiation with matter via absorption, emission, and reflection. The molecules adsorb frequencies which allow to determine their structure.

In general, FTIR spectrum of GO has a broad and intense band at ~ 3500 cm^{-1} which correspond to -OH groups and a peak at ~1722 cm^{-1} assigned to the C=O stretching mode, which is attributed to the carboxylic acid functional group. Another peak at ~ 1623 cm^{-1} assigned to the C=C stretching mode, characterized the aromatic structure of graphene. Besides, peaks at ~1377, ~1225 and 1067 cm^{-1} are belonging to the deformation mode of C-H, C-O-C and C-OH bonds found in GO, respectively. Figure 2.12a shows typical FTIR spectra of GO with different oxidation degree. [2]

In this thesis, the FTIR spectrum of graphene or GO are recorded using a Thermo Scientific™ Nicolet™ iS™ 50 with pure KBr as background reagents. The samples are mixed with dry KBr powder and grinded in an agate mortar. Then the resulting mixture is pressed into a transparent pellet by using a hydraulic press. Figure 2.12b shows the FTIR spectrometer equipment used.
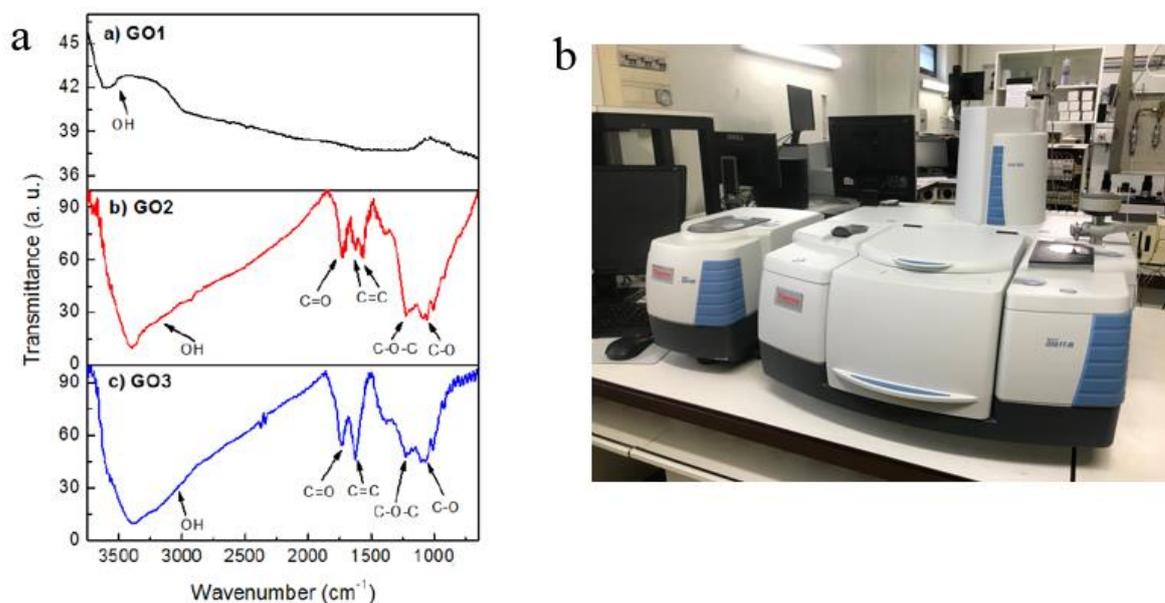
Figure 2.12 | (**a**) A typical FTIR spectra of GO with different oxidation degree, [2] and (**b**) a digital photo of FTIR spectrometer Thermo Scientific™ Nicolet™ iS™ used in this thesis.

2.3.6 Ultraviolet–visible spectroscopy

Ultraviolet–visible spectroscopy (UV-Vis) is commonly used in analytical chemistry for a quantitative measurement of different analytes like transition metal ions, organic compounds, and biological macromolecules. The concentration of a sample is determined by carrying out absorption measurement, following the Lambert- Beer's law:

$$A/l = \alpha C$$

Figure 2.13a shows UV-Vis spectra of graphene dispersions stabilized by cellulose nanocrystals (CNC) and Triton X-100. [10] The peak at $\lambda = 269$ nm seen in both samples is attributed to $\pi-\pi^*$ transitions of aromatic C-C bonds. [11] In order to preclude the influence of scattering phenomenon, the signal at wavelength $\lambda = 660$ nm is used. Using Lambert-Beer's law, the concentration of graphene dispersion ~0.9 mg mL^{-1} is measured 4 months later.

In this thesis, UV-Vis spectrum of graphene/GO dispersion are recorded using Spectrophotomètre UV-Visible: PASTEL UVILINE that is shown in Figure 2.13b.
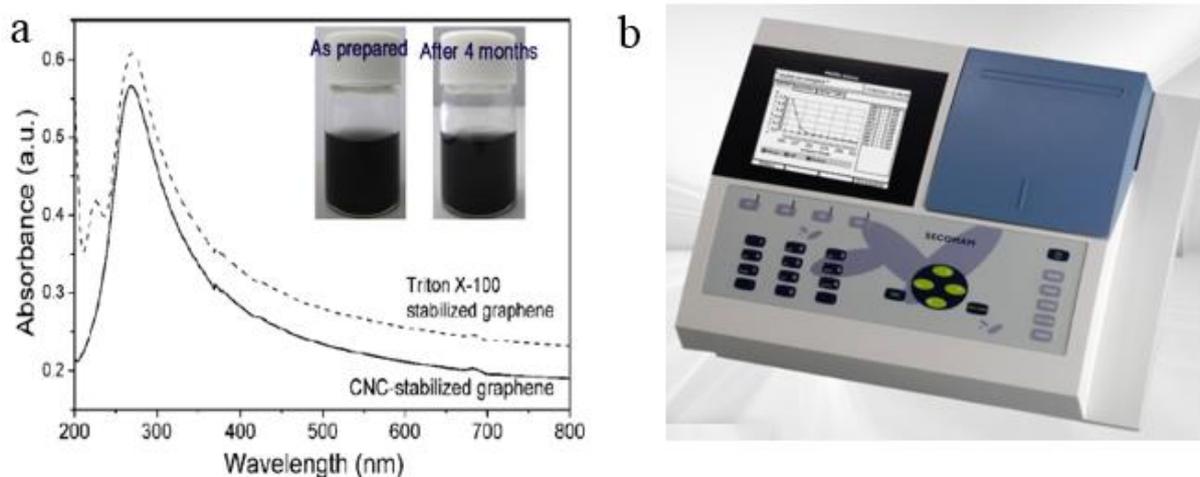
Figure 2.13 | (a) UV-Vis spectra of graphene dispersions stabilized by CNC and Triton X-100. Inset photographs are CNC-stabilized graphene dispersions: as-prepared and after 4 months. [10] **(b)** A digital photo of Spectrophotomètre UV-Visible: PASTEL UVILINE used in this thesis

2.4 Electrochemical measurements

All electrochemical measurements are carried out with a Gamry Ref600 potentiostat by using a traditional three-electrode cell. The Ni foam loaded with the electroactive material is used as working electrode, the platinum wire and the Ag/AgCl (KCl saturated solution) electrodes are used as the counter electrode and the reference electrode, respectively. The electrolyte chosen is 1M Na_2SO_4 solution (pH = ~6).
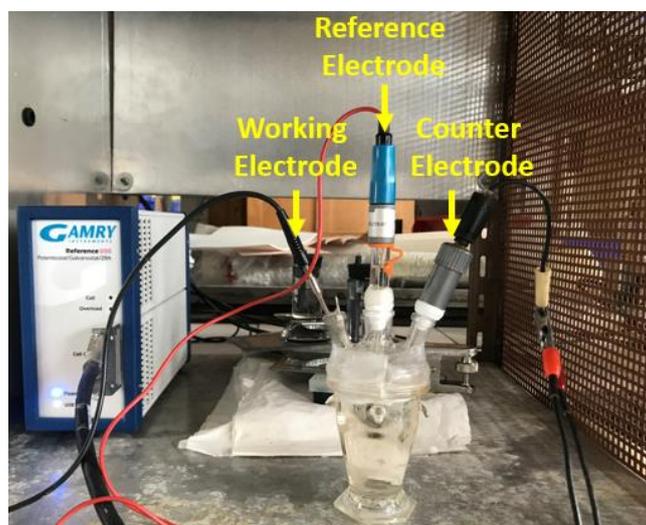
Figure 2.14 | Digital photo of three electrode system in this thesis

The cyclic voltammetry (CV) are measured in the voltage range of -0.8-0 V with a scan rate of 50 mV s^{-1}. Galvanostatic charge-discharge (GCD) are measured in the same voltage window of -0.8-0V at the current density of 1 A g^{-1}. Electrochemical impedance spectroscopy (EIS) measurements are performed in the frequency range from 0.1Hz to 100KHz and the oscillation potential amplitudes of 5 mV.

The specific capacitances (C, F g^{-1}) of working electrode are calculated from galvanostatic discharge curves according to: [12]

$$C = \frac{I \times \Delta t}{m \times \Delta V} \qquad (2.1)$$

Where I (A) is the discharge current, Δt (s) is the discharge time, m (g) is the mass of electroactive materials on single electrode, and ΔV (V) is the total potential change.

2.5 Summary

In this chapter, we have introduced our experimental methods through several aspects: preparation of samples, introduction of materials and equipment, characterization techniques, and electrochemical measurements.

The modified Hummers' method is employed to prepare graphite oxide. Liquid-phase exfoliation technique is used to disperse graphene and GO in PVA/water solution. Freeze-drying method is used to process GO/PVA hybrid aerogels. All above experimental processes are clarified.

.

References

1. Morimoto, N., Kubo, T. & Nishina, Y. Tailoring the Oxygen Content of Graphite and Reduced Graphene Oxide for Specific Applications. *Scientific Reports* **6**, 21715 (2016).

2. Reynosa-Martínez, A. C. *et al.* Effect of the degree of oxidation of graphene oxide on As (III) adsorption. *Journal of Hazardous Materials* **384** 121440 (2019)

3. Liu, X. *et al.* Simple, green and high-yield production of single- or few-layer graphene by hydrothermal exfoliation of graphite. *Nanoscale* **6**, 4598–4603 (2014).

4. Shin, Y.-E. *et al.* An ice-templated, pH-tunable self-assembly route to hierarchically porous graphene nanoscroll networks. *Nanoscale* **6**, 9734–9741 (2014).

5. Shah, R. R., Davis, T. P., Glover, A. L., Nikles, D. E. & Brazel, C. S. Impact of magnetic field parameters and iron oxide nanoparticle properties on heat generation for use in magnetic hyperthermia. *Journal of Magnetism and Magnetic Materials* **387**, 96–106 (2015).

6. Handbook of Analytical Techniques in Concrete Science and Technology | ScienceDirect. (Noyes publications / William Andrew Press, 2001)

7. Chatterjee, A. K. 8 - X-Ray Diffraction. in *Handbook of Analytical Techniques in Concrete Science and Technology* (eds. Ramachandran, V. S. & Beaudoin, J. J.) 275–332 (William Andrew Press, 2001).

8. Chen, Y. *et al.* Microbial reduction of graphene oxide by Azotobacter chroococcum. *Chemical Physics Letters* **677**, 143–147 (2017).

9. Perumbilavil, S., Sankar, P., Priya Rose, T. & Philip, R. White light Z-scan measurements of ultrafast optical nonlinearity in reduced graphene oxide nanosheets in the 400–700 nm region. *Applied Physics Letters* **107**, 051104 (2015).

10. Carrasco, P. M. *et al.* High-concentration aqueous dispersions of graphene produced by exfoliation of graphite using cellulose nanocrystals. *Carbon* **70**, 157–163 (2014).

11. Khan, U., O'Neill, A., Lotya, M., De, S. & Coleman, J. N. High-Concentration Solvent Exfoliation of Graphene. *Small* **6**, 864–871 (2010).

12. Wei, N. *et al.* Superelastic active graphene aerogels dried in natural environment for sensitive supercapacitor-type stress sensor. *Electrochimica Acta* **283**, 1390–1400 (2018).

Chapter 3

PVA-assisted pristine graphene dispersing in water via physisorption

Polymer can assist the pristine graphene dispersion in water. Understand of the stabilization mechanism can help us to better improve graphene dispersion and serve to the multifunctional composites' innovation. In this chapter, we demonstrated the pristine graphene concentration in water can be manipulated by varying concentrations of Polyvinyl Alcohol (PVA). Based on classic Flory's theory, we firstly proposed a model to describe the polymer adsorption process in graphene/ polymer/ solvent ternary system in a "dilute" regime and simulated the adsorption free energy change during this transformation.

3.1 Introduction

Pristine graphene can only slightly disperse in several environmentally disastrous organic solvents. [1,2] Comparing with this, it is better to use ecofriendly polymer as stabilizers to assist the layered materials dispersion in water media and to achieve a better stability as well as a higher nanosheet concentration. [3,4] In that way, the colloidal solution is an ideal starting material for nanocomposite preparation. [5–7] Besides, so-obtained colloidal solution possesses high graphene/ polymer ratio that would be of high interest in electric devices. [6]

The mechanism involved in the stabilization of graphene by polymer intermediates can be understood by the generation of a steric force when polymer chains are physically or chemically adsorbed on the surface. [8] The polymer covered nanosheets induces a repulsive force between two atomic layers, which prevents the further agglomeration. [9–13] May and Khan firstly proposed a framework to choose the most suitable polymer/solvent combination that is matched with Hildebrand solubility parameters. [8] They chose a relatively low polymer concentration (3 mg/ml) for all the experiments and assumed that polymer coils are partially adsorbed on graphene and partially stay freely in solvent. In that work, the authors presented a model based on lattice theory to predict correctly the dispersion ability of graphene in different polymer solutions. Elsewhere reported that it is possible to obtain well-dispersed pristine graphene in

Polyvinylpyrrolidone (PVP) solutions and pointed out the influence of PVP concentration on graphene concentration. [14] However, the mechanism of this influence has not been systematically discussed yet. And it is still eagerly required the effort to consider the interaction in the mixture system.

Indeed, the dispersion efficiency of graphene depends closely on the adsorption of polymer coils. With different polymer concentration, the macromolecule has gradually varying conformation, which can affect the free energy change of the whole graphene/ polymer/ solvent ternary system when adsorption occurs. To understand its influence, in this chapter, we have chosen ecofriendly pure water as the solvent in which graphene is insoluble, and PVA as the stabilizer because of its biocompatibility, non-toxic and processability. [15,16] Pristine graphene is dispersed in three PVA/water solution with different PVA concentrations using liquid-phase exfoliation in a sonic bath. More details about experiment has been presented in chapter 2.

3.2 Results and discussion

3.2.1 Results

In Figure 3.1a, as graphene's content varies, the color intensity varies with increasing polymer concentration C_p. Figure 3.1b fits the corresponded UV-Visible adsorption intensity of each specimen as function of the polymer concentration, at wavelength $\lambda = 660$ nm for the three polymers. We can observe two maximum UV intensity at polymer concentration $C_p \approx 0.3$ mg/mL and $C_p \approx 10$ mg/mL for PVA1, $C_p \approx 1.3$ mg/mL and $C_p \approx 21.3$ mg/mL for PVA2, $C_p \approx 2.9$ mg/mL and $C_p \approx 37.5$ mg/mL for PVA3. We respectively name these two peaks as C_c and C^* which are marked in Figure 3.1b.
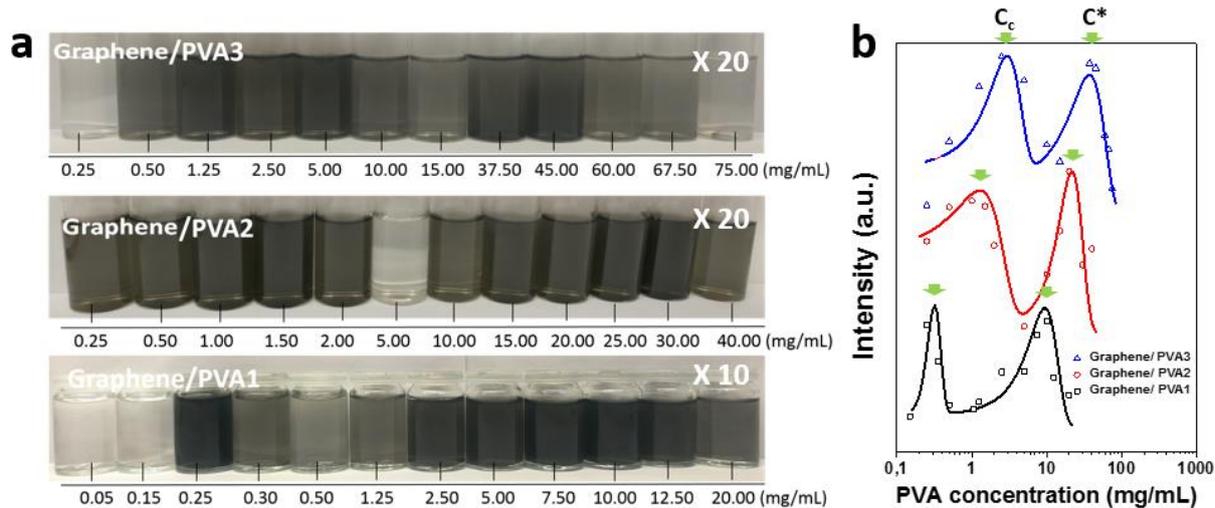
Figure 3.1 | Graphene stabilized by PVA in water media (**a**) Images of the colloid of graphene in PVA1, PVA2 and PVA3 solution after dilution 10 (x10) and 20 times (x20). (**b**) UV-Visible light absorption of graphene at λ = 660 nm curve versus PVA concentrations

Figure 3.2 presents the UV-Visible absorption intensity of pure polymer with different concentrations and graphene in PVA1, PVA2, and PVA3 solutions. Once the wavelength was greater than 300 nm, the polymers' absorption intensity was almost zero and was neglected. To preclude the influence of the scattering phenomenon, we used the signal at a λ = 660 nm wavelength for graphene. [4,48]
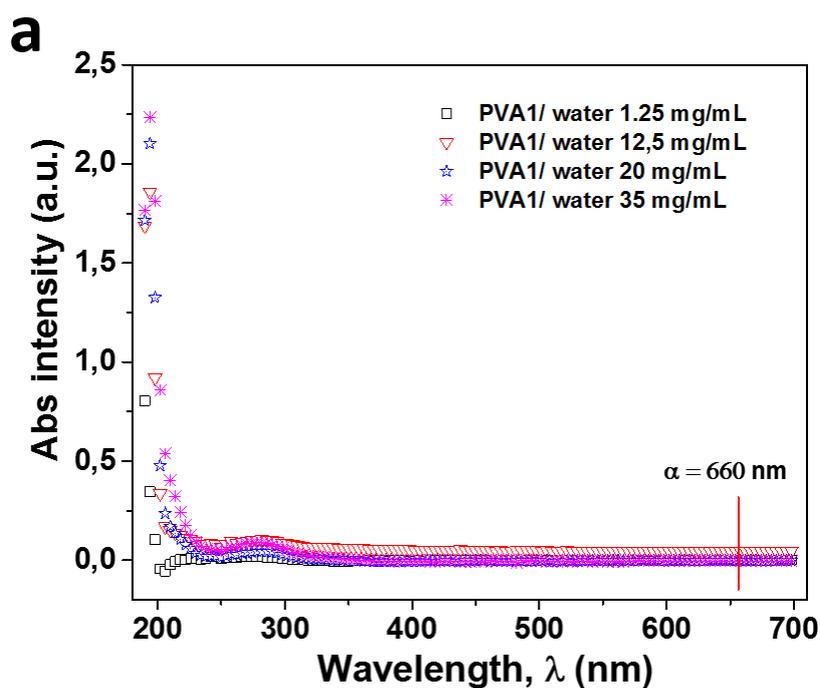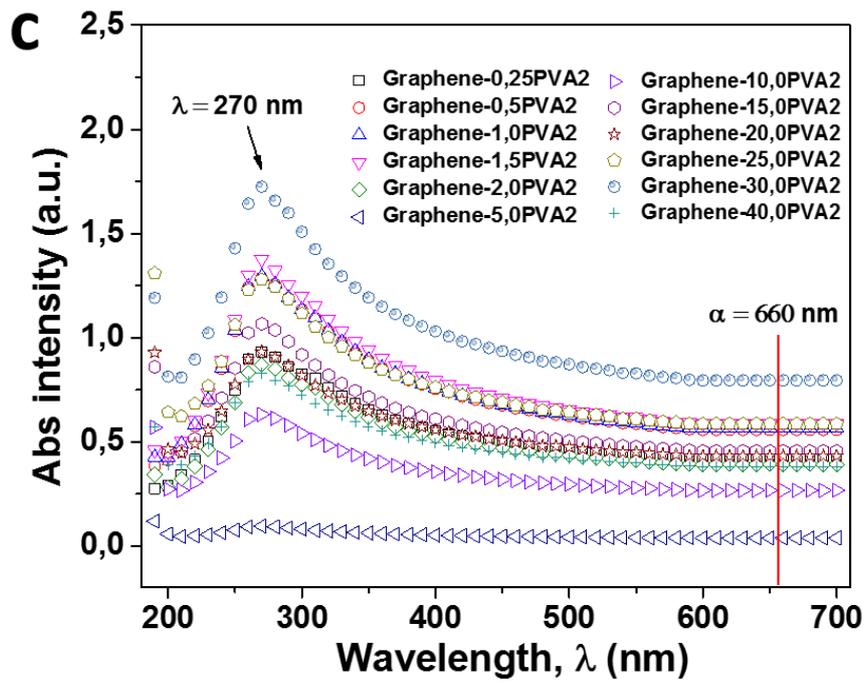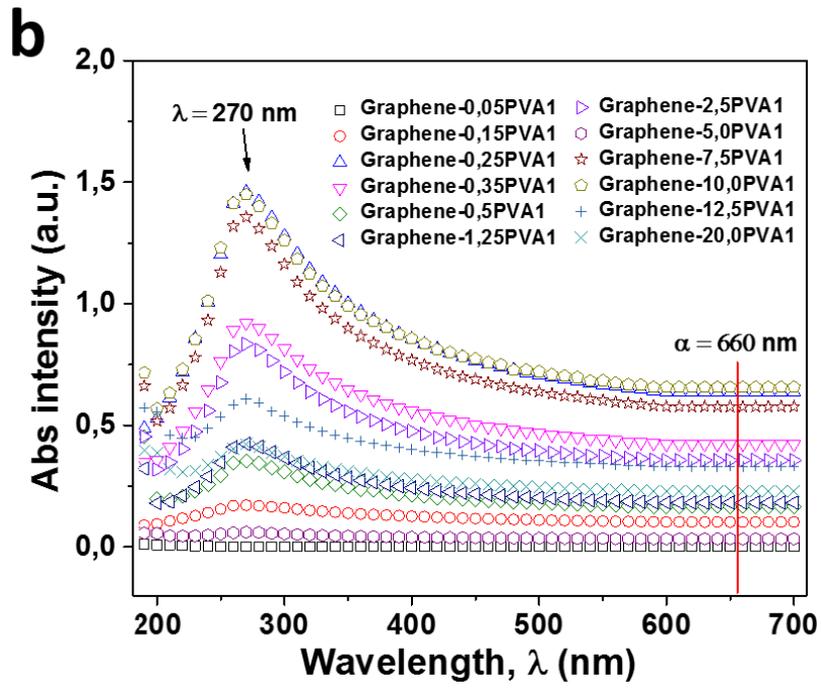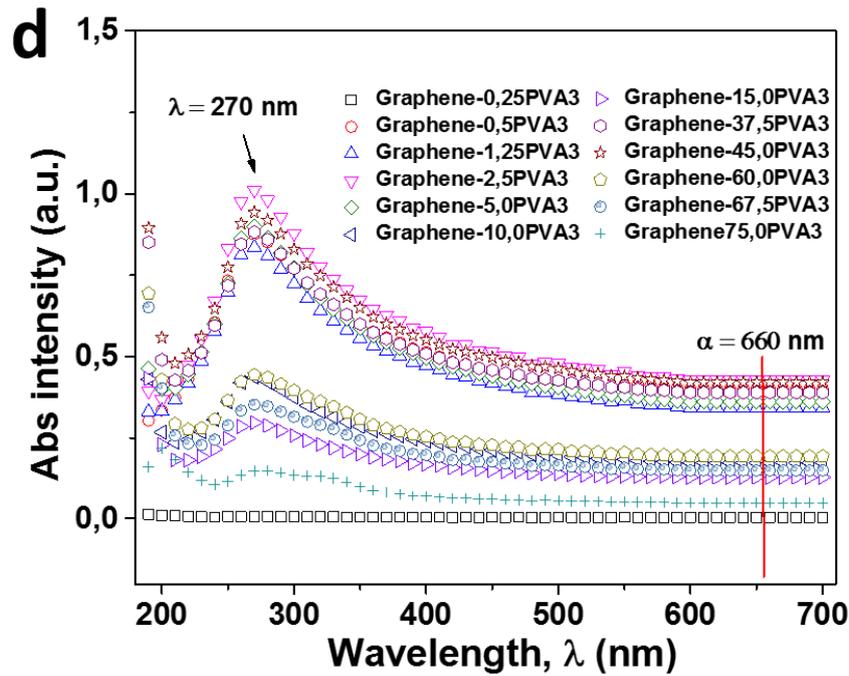
Figure 3.2 | The UV-visible absorption spectroscopy of solution of (**a**) PVA/ water at representative concentrations and (**b**) graphene in PVA1, (**c**) graphene in PVA2, and (**d**) graphene in PVA3

The absorption intensity is linearly proportional to the suspended species concentration: $A/l = \langle\alpha\rangle C$ (Beer-Lambert's law). A is the optical absorption intensity, I is the passage length (10 mm), and $\langle a \rangle$ is the extinction coefficient. Our study focused on the tendency of graphene concentration variations with C_p, which can be estimated using $\langle a \rangle$ equal to 2460 mL/m/mg. [17] The corresponding graphene concentration calculated gives 0.27 mg/mL and 0.28 mg/mL for PVA1 at C_c and C^*, 0.51 mg/mL and 0.61 mg/mL for PVA2, and 0.37 mg/mL and 0.35 mg/mL for PVA3. In this chapter we focused on polymer's critical concentration C_c. at which the content of graphene in polymer are respectively 47 wt.% for PVA1, 28 wt.% for PVA2 and 8 wt.% for PVA3 after 24h sonication.

Extending the sonication time efficiently increases graphene dispersion concentration. Figure 3.3 presents the variation in graphene concentration for PVA1 solution in one week of sonication, and corresponding UV-Visible light absorption of graphene at $\lambda = 660$ nm curve versus PVA1 concentrations.
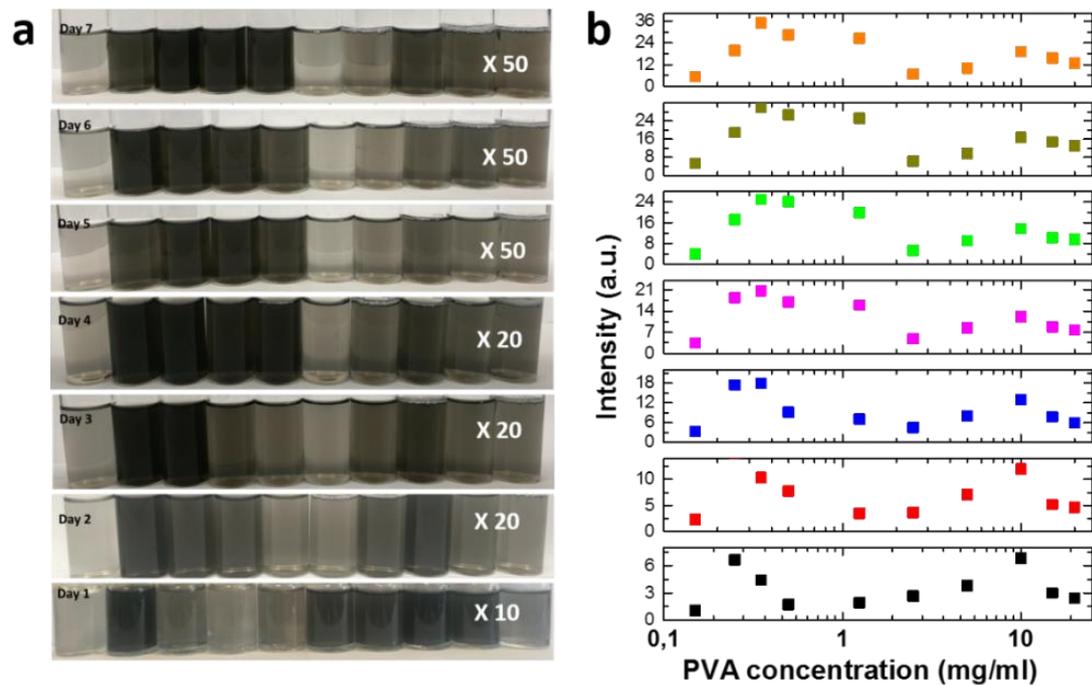
Figure 3.3 | Variation of the graphene concentration in one week. (**a**) Photographs of the colloid of graphene in PVA1 with different dilute times. (**b**) UV-Visible light absorption intensity of graphene at $\lambda = 660$ nm curve versus PVA1 concentration.

Figure 3.4 plots the variation of two peaks at C_c and C^*. Results show that extended sonication time efficiently increases graphene dispersion concentration. The highest graphene concentrations in PVA1 solution reach 1.42 mg/mL and 0.78 mg/mL respectively after 7 days of bath sonication. The ratio of graphene in polymer at first peak becomes 85 wt.%.
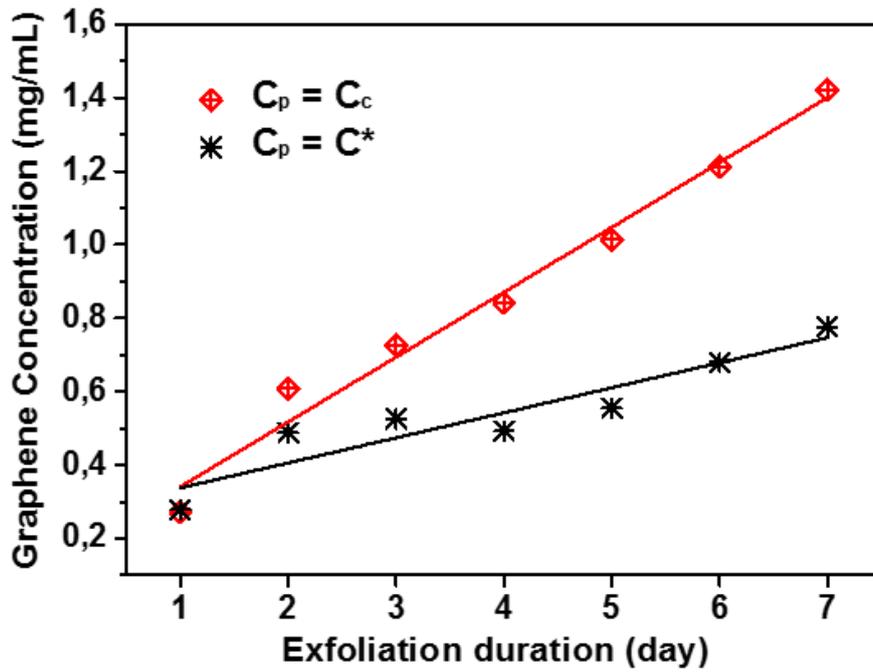
Figure 3.4 | Variation of the graphene concentration for one week at C_c in red and C^* in black

3.2.2 Discussion

As we know, polymer solution can be divided into the "semi-dilute" regime and the "dilute" regime, the boundary concentration is named overlap concentration C^*. [18,19] Moreover, the "dilute" solution is further distinguished by another boundary concentration, denoted C_s. [19,20] In the early 90s, Dondos and Tsitsilianis have already demonstrated that the variation of polymer conformation occurs in the "dilute" solution. [21] (see Figure 3.5)
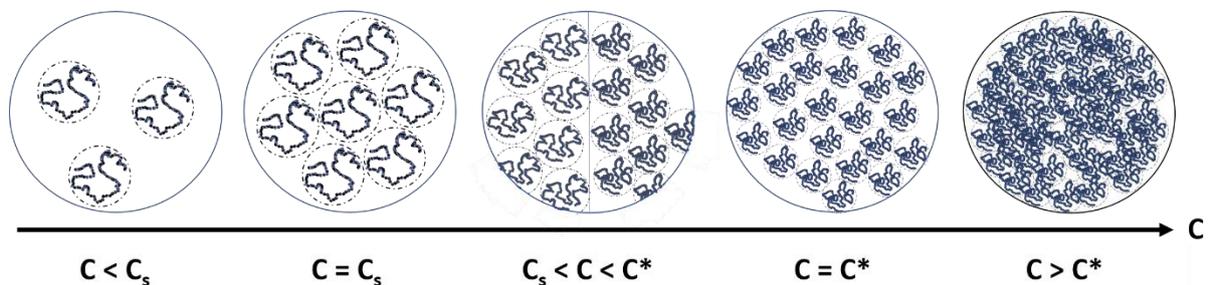
Figure 3.5 | Schematic representation of the polymer concentration regions defined in relation to the two specific concentrations C_s and C^*. Dashed line shows the pervaded volume of single polymer coil.

When concentration is lower than C_s, the polymer coils are isolated, and the solution is called "very dilute". When over than C_s but lower than C^*, the intermolecular interaction is produced, coils are compressed leading a pervaded volume decreasing, but maintains macromolecule's individuality. When above C^*, the polymer coils start to penetrate each other. [21]

C^* can be evaluated using the intrinsic viscosity $[\eta]$ of solution: [22]

$$C^* = 1/ [\eta] \qquad (3.1)$$

Moreover, $[\eta]$ can be obtained according to Mark-Kuhn–Hawink's equation: [23]

$$[\eta] = K_\eta \, M^\tau \qquad (3.2)$$

where K_η is a factor impacted by temperature, polydisperse and branching, the τ value is linked to thermodynamic state of the solvent, chain stiffness, macromolecular conformation, and M is the average molar weight of the polymer. For a PVA aqueous solution, K_η is 4.53×10^{-4} dl/g and τ is given elsewhere a value 0.64 at room temperature. [24]

In a similar way, C_s is closely linked with the intrinsic viscosity of polymer solution: [19]

$$C_s = 2.5 \text{x} 10^{-2}/ [\eta] \qquad (3.3)$$

C^* and C_s for PVA1, PVA2 and PVA3 are calculated as showing Table 3.1.

Table 3.1 C_s and C^* of PVA1, PVA2 and PVA3

Samples	PVA1	PVA2	PVA3
C^*, mg/mL	11.8	24.8	41.7
C_s, mg/mL	0.3	0.6	1.0

It is interesting to notice that the first peaks at C_c given ~0.3, ~1.3 and ~2.9 mg/mL for PVA1, PVA2 and PVA3 are closing to their "very dilute" regime, and the another one at C^* given ~10, ~21.3 and ~37.5 mg/mL for PVA1, PVA2 and PVA3 are near their overlap concentration C^*. This phenomenon will be explained in section 3.5.

3.3 Electrical conductivity measurement

Under vacuum filtration, nanocomposites can be easily produced from liquid phase starting materials. Figure 3.6a shows a conductive flexible membrane in which the graphene in PVA1 is 47 wt.%. Here, we use straight 'four-point probe' to measure the conductivity. By several different direction measurement, an average value of electrical conductivity, 10 S/m, has been obtained. This nanocomposite's cross-section had a lamellar structure, as demonstrated in Figure 3.b.
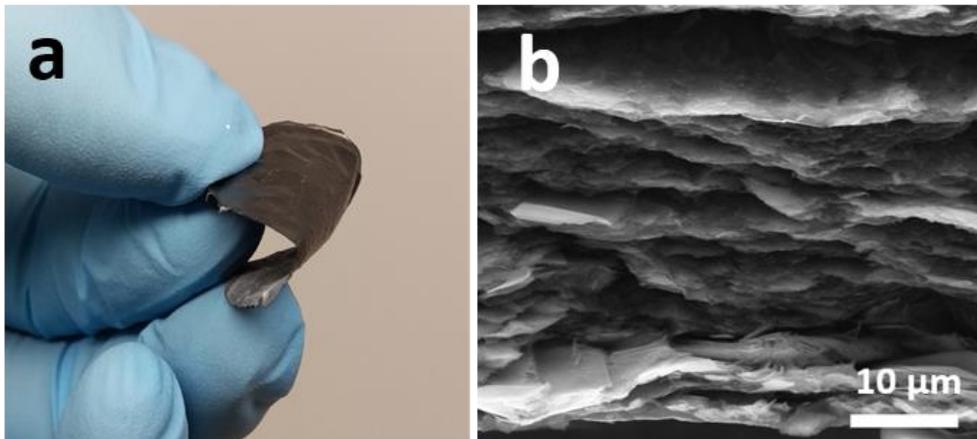
Figure 3.6 | (a) A flexible composite membrane of the graphene/PVA1 (47 wt.%) with an electrical conductivity of approximately 10 S/m. **(b)** Cross-section of the graphene/PVA1 (47 wt.%) membrane.

3.4 Characterizations

3.4.1 Transmission Electron Microscope (TEM)

Transmission electron microscopy (TEM) measurements are used to assess the nanosheets' morphology. The TEM images (Figure 3.7 a-d) display similar lamellar graphene structures with an average length of approximately 0.3-1 μm and an average width of approximately 0.8 μm. The number of nanosheets is estimated by analyzing the flakes' folded edges, which varies from 1 to 5 layers. Figure 3.7e shows an example of graphene flakes with only three layers. Electron diffraction patterns are obtained with monolayers showing typical hexagonal spots, as demonstrated in Figure 3.7f.

73
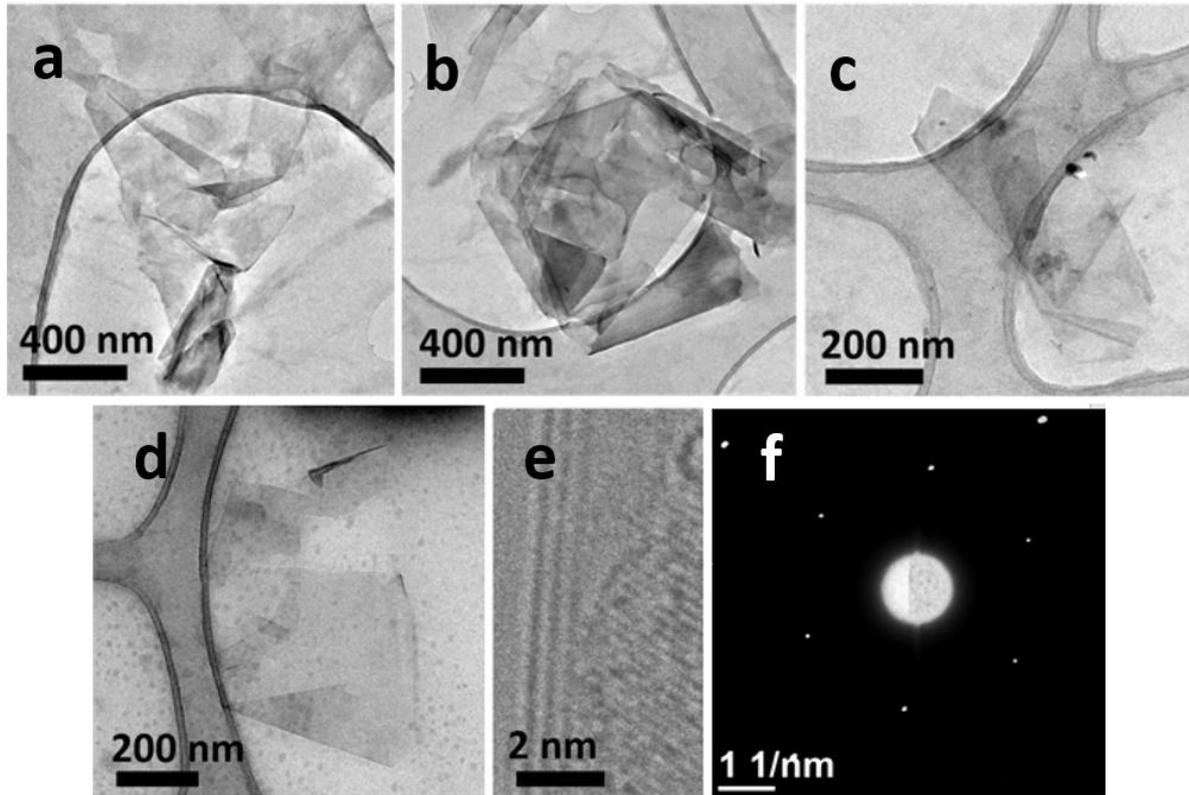
Figure 3.7 | TEM images of typical graphene obtained at (**a**) $C_p = 0.25$, (**b**) 1.25, (**c**) 5, and (**d**) 20 mg/mL (**e**) Graphene flake with three atomic layers in TEM. (**f**) An electron diffraction pattern from a selected monolayer area at $C_p = 0.25$ mg/mL

The TEM images of Figure 3.8a and b show that PVA molecules gather and isolate to each other, respectively. No electron diffraction patterns in Figure 3.8c proves further PVA grains in Figure 3.8a and b. Figure 3.8d and e display PVA molecules adsorbed on graphene surface and existed between graphene layers, which demonstrates that polymer molecules can play the role of preventing graphene agglomeration. Electron diffraction patterns are obtained from graphene monolayer area at Figure 3.8e showing typical hexagonal spots, as demonstrated in Figure 3.8f.
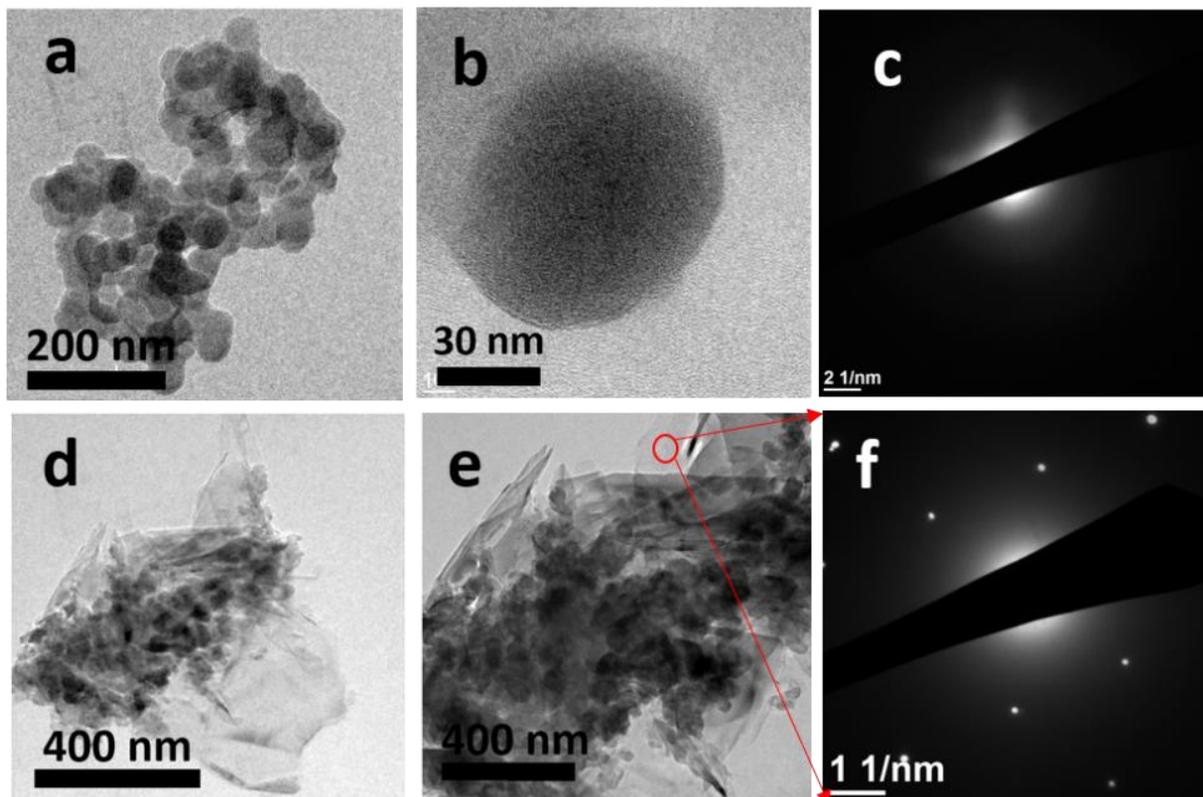
Figure 3.8 | TEM images of typical graphene obtained at $C_p = 0.25$. (**a**) Gathered PVA molecules, (**b**) Isolated PVA molecule (**c**) An electron diffraction pattern from a selected PVA molecule. (**d, e**) PVA molecules adsorbed on graphene layers and existed between graphene layers. (**f**) An electron diffraction pattern from a selected graphene monolayer area at (**e**)

3.4.2 X-ray Photoelectron Spectroscopy

Pristine graphite is analyzed by XPS. It is composed of 97.8 % of C and 2.2 % of O. After calibration, the major peak of C 1s is located at 284.4 eV, which attributes to C=C from the carbon aromatic ring. The binding energy difference between C-C and C=C is 1.1 eV. Carbon in graphite are also witnessed to form bond with oxygen. C-O, C=O, and O-C=O peaks are found at 286.4 eV, 287.4 eV, and 289.0 eV, respectively. Furthermore, peak at 291.4 eV corresponds to π to π^* transition. [25,26] The peaks of O 1s located at 531.3 eV, 532.5 eV and 533.8 eV are from the groups of C-O-C, C=O and O-C=O. [27] More fitting details are shown in Figure 3.9 and Table 3.2. As shown, a relatively weak oxygen contain can be found in the raw graphite materials. Taking into account the mild exfoliation conditions, the resulting graphene

will only be slightly oxidized on the nanosheet edge or at several defect sites. In a general way, the graphene sheet stays chemically stable.
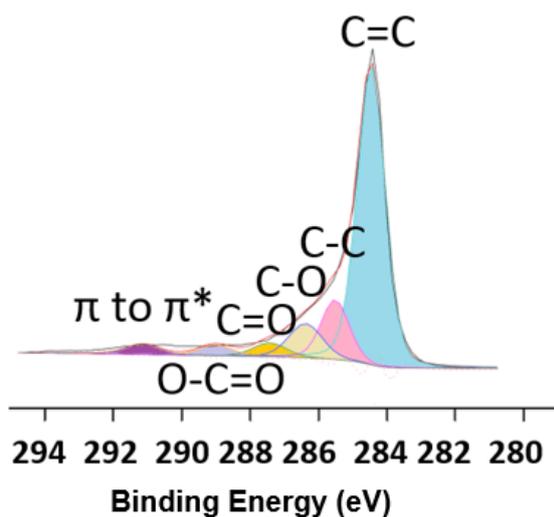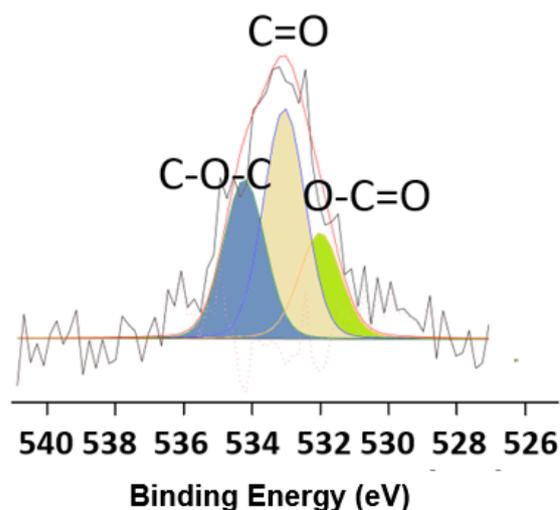
Figure 3.9 | XPS result of pristine graphite: (**a**) C 1s and (**b**) O 1s

Table 3.2 Fitting details in C 1s and O 1s of graphite.

Graphite	Percent, at %	Peaks in details	Positions (eV)
C 1s	97.8	C=C	284.4
		C-C	285.5
		C-O	286.4
		C=O	287.4
		O=C-O	289.0
		π to π*	291.4
O 1s	2.2	O-C=O	531.3
		C=O	532.5
		C-O-C	533.8

3.5 Stabilization mechanism

It is important to explore the mechanism of PVA-stabilized graphene in aqueous solution and the variation of the graphene concentration in this media to understand this phenomenon. The polymer-assisted 2D materials' dispersion can be divided into two steps: 1) pristine 2D materials are exfoliated from raw materials; 2) polymers adsorb on nanosheets and stabilize them by steric forces. At step 1, the efficiency of exfoliation process is closely related to the viscosity of PVA solution which remains almost constant in the "diluted regime" (< C*). [28–30] If we assume that excess amount of graphene nanosheets can be obtained after ultrasonic sonication in PVA solutions with different concentrations, graphene content is mainly governed by step 2, in which PVA chain adsorption takes place if it is favorable considering the free energy variation of the whole system.

Regarding the interaction nature, it can be either chemisorption or physisorption in polymer chains on graphene. The XPS results of pristine graphite show low oxygen levels (~2.2 %) in last section. Considering the chemical inertness of pristine graphene under the exfoliation conditions, the major energy gain of real chain physisorption is estimated using equation (3.4) [31]:

$$F_{ads} \approx -\delta_e kTN \frac{b}{D}, \tag{3.4}$$

where D is the thickness of the adsorbed chain, b is the length of Kuhn monomer, N is the number of Kuhn monomers in one coil, and $\delta_e kT$ is the energy gain per Kuhn monomer in the polymer coil after adsorption.

Adsorption energy parameter, δ_e

δ_e is the so-called adsorption energy parameter of polymer-surface interactions representing the nature of the components involved in adsorption, including adsorbents, polymers, and solvents. [31] When $0 < \delta_e \leq 1$, the adsorption is weak, and when $\delta_e > 1$, the adsorption is strong. [32] δ_e depends on the material's intrinsic properties.

In classic Flory Theory, when a polymer coil in dilute solution gets close to a surface, it tends to adsorb on the surface to gain adsorption free energy $-\delta_e kT$ for a Kuhn monomer. For the best of our knowledge, there is not a direct calculation method for δ_e reported in the literature.

However, a different expression has been shown in elsewhere report, in which A. Silberberg developed a quasicrystalline lattice model and proposed a similar formula $-(\chi_s-\chi)kT$ to calculate the adsorption energy of one repeating unit adsorbed on the surface in solution. [33] The specific physical process was described as the exchange of a solvent molecule in contact with the surface in solvent reference by a polymer monomer with equivalent size from the pure reference phase. In this expression χ is the Flory-Huggins' interaction parameter which is used for the characterization of interaction energy between polymer and solvent in the mixture, χ equals:[31]

$$\chi = \frac{z}{2}\left(\frac{2u_{ps}-u_{pp}-u_{ss}}{kT}\right) \tag{3.5}$$

Where z is coordination number from model, u_{pp}, u_{ss} and u_{ps} are defined as potential-energy for each type of contact (polymer-polymer, solvent-solvent and polymer-solvent). Connecting the potential-energy with the Hildebrand solubility parameter, there is a classic relationship:

$$u_{ps} = -\frac{2v_o\delta_p\delta_s}{z} \tag{3.6}$$

where v_0 is the solvent molecular volume. Water's volume equals 30 $\mathring{A}^3$. δ_p and δ_s are the solubility parameter of polymer and solvent. Combination equation 3.5 and equation 3.6, χ equal to:

$$\chi = \frac{v_o}{kT}(\delta_p - \delta_s)^2 \tag{3.7}$$

Hildebrand solubility parameters can be used to calculate χ in the non-polar system. However considering the polarity and hydrogen bonding in polar solvent, like water, the Hansen solubility parameters are required [34]:

$$\chi = \frac{v_o}{kT}\left[\left(\delta_{d,p} - \delta_{d,s}\right)^2 - 0.25\left(\delta_{p,p} - \delta_{p,s}\right)^2 - 0.25\left(\delta_{h,p} - \delta_{h,s}\right)^2\right] \tag{3.8}$$

where δ_d, δ_p and δ_h are dispersion solubility parameters, polar solubility parameter and hydrogen bonding solubility parameter, respectively. Correspondingly, χ_s can be calculated by [33]:

$$\chi_s = \frac{z}{kT}\left[u_{gs} - \left(u_{gp} - u_{pp}\right) - \left(\frac{1}{2}\right)(u_{ss} + u_{pp})\right] \tag{3.9}$$

Combined with equation 3.6, χ_s can also be calculated by the Hildebrand solubility parameters:

$$\chi_s = \frac{v_o}{kT}\left[(\delta_s - \delta_g)^2 - (\delta_p - \delta_g)^2\right] \tag{3.10}$$

So far, we found that two parameters, δ_e and χ_s-χ, used in representing the interaction between polymer and the surface and calculating the adsorption free energy. But their mismatch is that $-\delta_e kT$ corresponds to the energy change of one Kuhn monomer and $-(\chi_s$-$\chi) kT$ depicts the interaction of one repeating unit.

We speculate that, in a mean-field estimate, the repeating units are uniformly distributed within a given distance from the absorbent. Therefore, the fraction of Kuhn monomer in direct contact with absorbent within a distance of one repeating unit size l equals to l/b. The number of adsorbed repeating units in a Kuhn length is then nl/b where n is the number of repeating units in a Kuhn monomer. Since nl and b are both the Kuhn length, nl/b equals to 1, indicating that the adsorption energy of a Kuhn monomer is that of a repeating unit. Therefore, the relationship of $\delta_e = \chi_s$-χ could be established. Then, developing equation 3.10 in a similar way to that of equation 3.8 using Hansen solubility parameters, it has $\delta_e = 0.9$ for the graphene/ PVA/ water ternary system. Table 3.3 shows the Hansen solubility parameters of each component.

Table 3.3 The Hansen solubility parameters of graphene, PVA and water. [34–36]

	δ_d	δ_p	δ_h
Graphene	18.0 (15-21)	9.3 (3-17)	7.7 (2-18)
PVA	17.0	9.0	18.0
Water	15.5	16.0	42.3

The free energy of a free-standing polymer coil before adsorption

The free energy of a polymer coil in a solvent, without any graphene incorporation, is composed of an energetic term and a confinement term as described in equation 3.11: [31]

$$F = F_{ener} + F_{conf} \approx kT \left(v \frac{N^2}{R_{end}^3} + \frac{R_{end}^2}{Nb^2} \right) \tag{3.11}$$

where k is the Boltzmann constant, T is the temperature, N is the total number of Kuhn monomers in one coil, b is the length of Kuhn monomer ($b \approx 1.5$ nm), and v is the excluded volume of a Kuhn monomer ($v \approx b^3$). R_{end} represents the end-to-end distance for a free-standing polymer coil in the solution. The lowest energy in equation 3.11 is obtained when the first order derivation, dF/dR_{end} equals to zero. It has $R_{end} = bN^\alpha$. If it is good solvent, $\alpha = 0.6$.
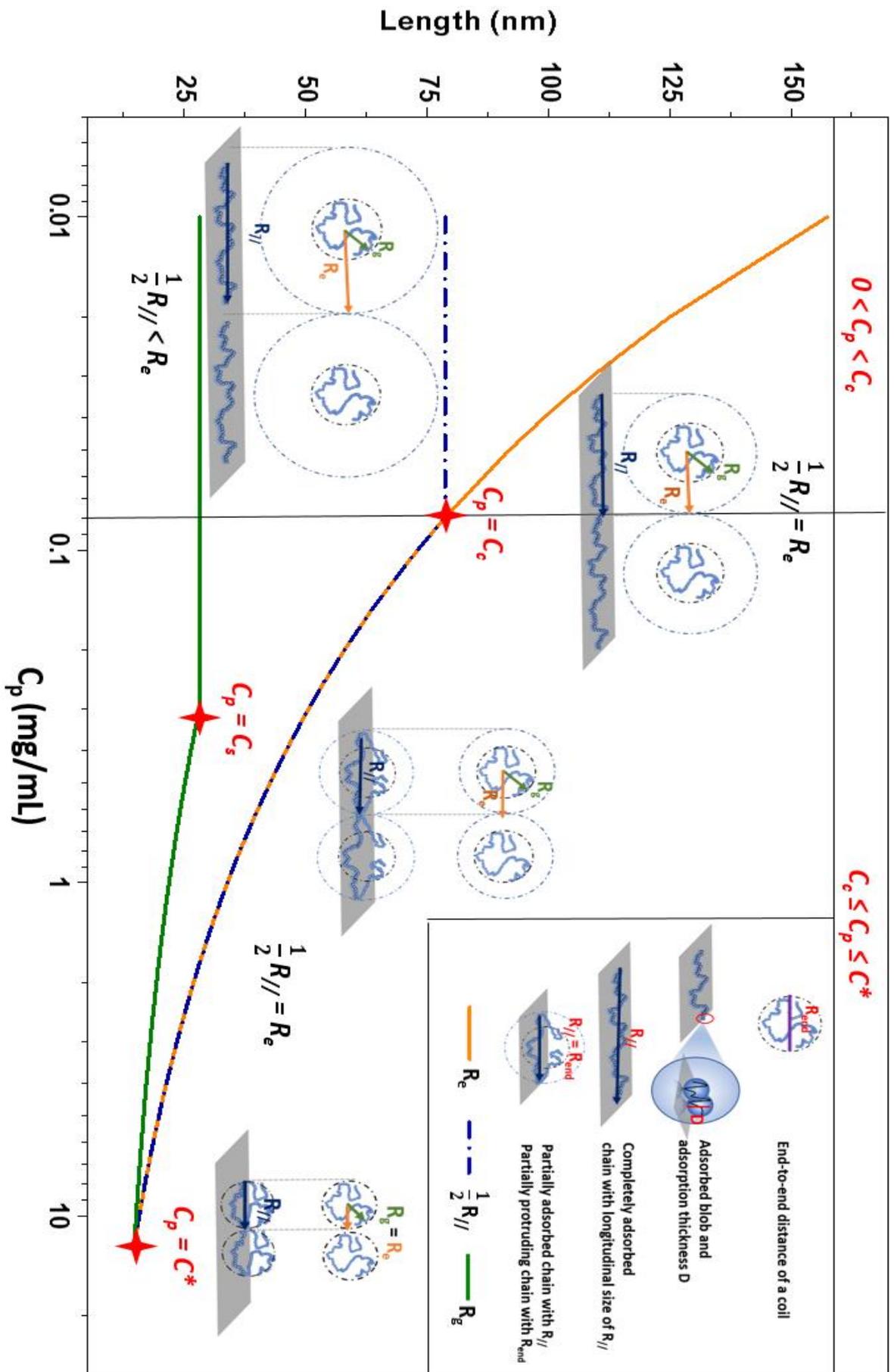
Figure 3.10 | Adsorption process of polymer coils in "dilute" regime. R_g is defined as the average square distance between monomers and the polymer's center of mass in a given conformation. [31] R_g has a relationship with R_{end}: $R_{end} = \sqrt{6}\, R_g$. R_{end} is a constant calculated by $bN^{0.6}$ at $C_p \leq C_s$, and R_g is a constant in this regime in good solvent. [30,31] At $C_s < C_p < C^*$, R_g will continuously decrease due to the repulsive forces produced among the coils until C^* at which the dimension is the same as in Flory theta solvents, $R_{end} = bN^{0.5}$. [22] We assume that the coil volume decreases linearly as C_p increases, which decreases R_g by a cube root (the green line). The effective volume represents the average volume occupied by each coil in the solution. Its effective radius R_e depends on polymer molar weight M and concentration C_p (see equation 3.18). R_e is greater than R_g in "dilute" regime. When the concentration reaches C^*, $R_e = R_g$ [18,24] (the orange line). $R_{//}$ is the longitudinal size of the coil after surface adsorption. At $C_p < C_c$, the polymer chains are completely adsorbed, and $R_{//}$ remains constant (the dotted blue line). It has $1/2 R_{//} < R_e$ in this regime. When C_p reaches a critical concentration C_c, the adsorbed polymer chains connect to their neighbors, $R_{//}$ starts to decrease and partial adsorption occurs. From C_c to C^*, $R_{//}$ is equivalent to the size of the free-standing coil's effective volume projected on the adsorbent. Therefore, it has $1/2 R_{//} = R_e$ at $C_c \leq C_p \leq C^*$ (this relationship is represented by the overlapping dotted blue line and orange line). All the curves in Figure 3.10 are obtained by taking PVA1 in water as an example.

The free energy of a polymer coil after adsorption

When free-standing polymer coils meets an adsorbent, they attempt to attach to absorbent as much as possible to gain the adsorption energy. Therefore, polymer coils should be confined to compensate for the energy gain by losing conformational entropy. The free energy of an adsorbed polymer $F_{a,\,p}$ consists of an entropic term and an enthalpic term according to Flory's theory: [31]

$$F_{a,p} \approx \mathrm{k}TN \left(\frac{b}{D}\right)^{5/3} - \delta_e kTN \frac{b}{D} \tag{3.12}$$

At very low polymer concentrations, polymer chains have enough space to spread out in solvents and show a "pancake-like" conformation, as shown in Figure 3.10 (the left side of the black vertical line). [37,38] However, as the polymer concentration increases (the right side of the black vertical line), the chain-chain interaction appears and compresses the adjacently adsorbed-chains. We first define a new critical concentration, C_c, below which complete

adsorption occurs. Once the polymer concentration is higher than C_c, the coil starts to partially adsorb with N^* ($N^* \leq N$) Kuhn monomers on the absorbent and partially protrudes into the solution with N-N^* Kuhn monomers. The coils' protruding parts, usually called "loops" for the middle segments and "tails" for the end segments, have been thoroughly investigated for decades.[39] Therefore, there are two situations of polymer coil adsorption in solution.

a) The free energy of a complete adsorption chain

For a complete adsorption chain, the free energy after adsorption is exactly calculated by equation 3.12. The variation of the free energy showed in equation 3.13:

$$\Delta F_{tot} = F_{a,p} - F \approx [kTN \left(\frac{b}{D}\right)^{5/3} - \delta_e kTN \frac{b}{D}] - F \tag{3.13}$$

F is calculated by equation 3.11. In "very dilute" regime, it has $R_{end} = bN^{0.6}$ in a good solvent to reach the minimum free energy of the coil. Water is usually considered as a good solvent for PVA. [40] So, here the free energy of free-standing polymer coil has $F = 2N^{1/5}kT$. After complete adsorption, the thickness D of adsorbed chain can be calculated by [31]

$$D = \frac{b}{\delta_e^{3/2}} \tag{3.14}$$

given $\delta_e = 0.9$, it has $D = 1.7$ nm for completely adsorbed chain. Then the energy gain F_{ads}, where $F_{ads} = -\delta_e kTN \frac{b}{D}$, are compensated by its confinement energy F_{conf}, where $F_{conf} = kTN \left(\frac{b}{D}\right)^{5/3}$. It has $F_{a,p} = 0$, and $\Delta F_{tot} = -F = -2N^{1/5}kT$. The strictly negative ΔF_{tot} means that the adsorption of the polymer PVA on to the graphene surface is spontaneous and irreversible. It is important to notice that the graphene content increases with the polymer concentration C_p at beginning because of the energy gain increase.

b) The free energy of a partial adsorption chain

For a partial adsorption chain, the free energy of the adsorbed part $F_{a,p}$ becomes:

$$F_{a,p} \approx kTN^* \left(\frac{b}{D}\right)^{5/3} - \delta_e kTN^* \frac{b}{D} \tag{3.15}$$

where the N^* is the number of adsorbed Kuhn monomers. The more sophisticated bound fraction effect and concentration profile as a function of the adsorption energy are not discussed

in this chapter, since the polymer concentration and intramolecular interactions remain low. In the first approximation, the protruding part is considered as a whole, and its end-to-end distance R_{end} roughly equals $R_{//}$ ($R_{end} \approx R_{//}$), where $R_{//}$ is the longitudinal size of the "pancake" as shown in Figure 3.10. This approximation is enough to reveal that the protruding part is undergoing extension stress and has a size change. When the adsorption size $R_{//}$ decreases, the protruding part dimension R_{end} also decreases, and vice versa. The free energy of the protruding part $F_{p,\,p}$ is estimated by: [31]

$$F_{p,p} \approx kT \left(v \frac{(N-N^*)^2}{R_{//}^3} + \frac{R_{//}^2}{(N-N^*)b^2} \right) \tag{3.16}$$

the variation of the free energy is shown in equation 3.17:

$$\Delta F_{tot} = F_{a,p} + F_{p,p} - F \approx kTN^* \left[\left(\frac{b}{D}\right)^{5/3} - \delta_e \frac{b}{D} \right] + kT \left[v \frac{(N-N^*)^2}{R_{//}^3} + \frac{R_{//}^2}{(N-N^*)b^2} \right] - F \tag{3.17}$$

with polymer concentration increasing, F varies from $2N^{1/5}kT$ to kT because of coils' size change from $R_{end} = bN^{0.6}$ to $R_{end} = bN^{0.5}$. More specifically, when C_p varies from C_s to C^*, the corresponding exponent α varies from 0.6 to 0.5. To simplify the calculation, we considered F decrease is linear. ΔF_{tot} depends on polymer concentration C_p and adsorbed thickness D.

For spontaneous adsorption to occur, both completely adsorbed chains and partially adsorbed chains should have an overall free energy change equal or less than 0. The completely adsorbed chains have been proved $\Delta F_{tot} < 0$, however, for partially adsorbed chain, there is:

$$\Delta F_{tot} = F_{a,p} + F_{p,p} - F \approx kTN^* \left[\left(\frac{b}{D}\right)^{5/3} - \delta_e \frac{b}{D} \right] + kT \left[v \frac{(N-N^*)^2}{R_{//}^3} + \frac{R_{//}^2}{(N-N^*)b^2} \right] - F \leq 0$$

The variables in equation (3.17), including N^*, D, and $R_{//}$ have a direct relationship with the polymer conformation, which is a function of its concentration. The polymer conformation before and after adsorption is detailed in Figure 3.10 by showing the four characteristic dimension parameter variations: R_g is the gyration radius, R_{end} is the end-to-end distance, $R_{//}$ is the longitudinal size of the adsorbed chain, and R_e is the radius of the effective volume of a free-standing polymer coil. As previously described, each coil attempts to occupy the absorbent surface as much as possible to gain adsorption-free energy. We expect that the polymer's confinement is rapid enough that all of the chains' intra- and inter-molecular forces reach equilibrium, so neither overlap between two adjacent chains nor shrinkage of the longitudinal

size occur. We can then estimate the polymer coils' parameters as a function of the polymer concentration.

The effective radius R_e is described by: [18]

$$R_e \approx \left(\frac{3M}{4\pi N_A C_p}\right)^{1/3},$$ (3.18)

where N_A is the Avogadro constant, and M is the polymer molar weight. Pursuant to Flory's theory, the longitudinal size $R_{//}$ of a polymer chain under uniaxial compression with a thickness D is a function of the adsorbed Kuhn monomer numbers N^*: [31]

$$R_{//} = N^{*3/4} b \left(\frac{b}{D}\right)^{1/4}$$ (3.19)

For complete adsorption ($C_p < C_c$), the adsorbed Kuhn monomer number N^* in equation (3.19) equals N. For partial adsorption ($C_c \leq C_p \leq C^*$), the longitudinal size of the adsorbed part $R_{//}$ is the size of the projection of the polymer coils' effective volume on the absorbent; thus, it has a relationship of $1/2 R_{//} = R_e$ as shown in Figure 3.10. Combining equation (3.18) and (3.19) with this relationship, $R_{//}$ depends on the polymer concentration C_p and its molar weight M:

$$R_{//} \approx 1.47 C_p^{-1/3} M^{1/3},$$ (3.20)

where C_p is expressed in mg/mL, M is expressed in g/mol, and the numerical simplification $R_{//}$ is expressed in nm. By combining equations (3.19) and (3.20), we deduct the expression of the adsorbed Kuhn monomer number N^* for one chain:

$$N^* \approx 1.67 C_p^{-4/9} M^{4/9} b^{-5/3} D^{1/3}$$ (3.21)

Hereafter, combining equations (3.20) and (3.21) with equation (3.17), ΔF_{tot} is only a function of the polymer concentration C_p and the adsorbed thickness D. For partial adsorption ($C_c \leq C_p \leq C^*$), D is no longer constant like complete adsorption, but progressively increases under the effect of the protruding part. ΔF_{tot} depends on the polymer concentration C_p and adsorption thickness D for the three PVA samples, which is shown in Figure 3.11. A concave surface of ΔF_{tot} is cut by the $\Delta F_{tot} = 0$ plane, which can be defined as the energetic adsorption surface. Under this plane, the adsorption process is thermodynamically favored and irreversible. Obviously, all three PVA can spontaneously adsorb onto graphene within specific concentration ranges. PVA1, with the highest molar weight, has the deepest free energy,

indicating a high transformation potential. In contrast, the adsorption becomes increasingly difficult for PVA2 and PVA3.
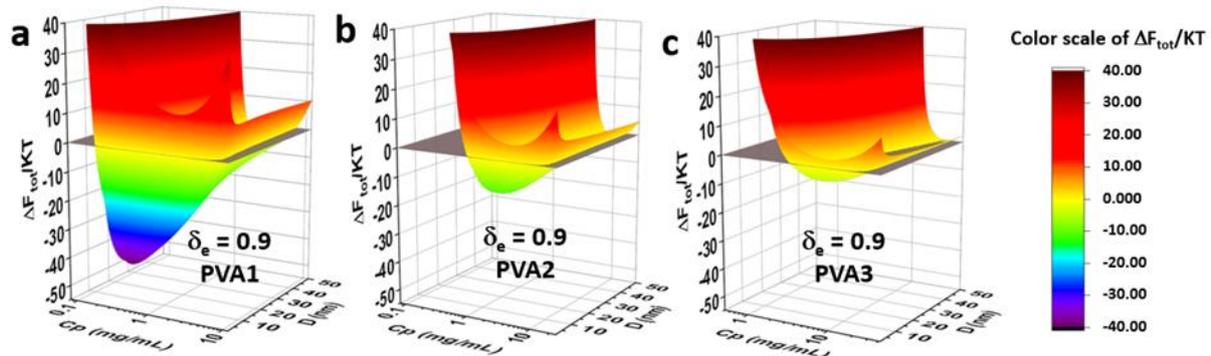
Figure 3.11 | Calculated free energy ΔF_{tot} plotted as a function of the polymer concentration C_p (mg/mL) and adsorbed thickness D (nm). In the case of real situation, successful adsorption is characterized by the thickness (D), which is greater than the polymer's Kuhn length b and smaller than the size of the polymer coil R_{end} ($b < D < R_{end}$). δ_e is 0.9 for (**a**) PVA1 (130000 g/mol), (**b**) PVA2 (31000-50000 g/mol), and (**c**) PVA3 (13000-23000 g/mol).

The influence of the polymer molar weight can be explained by the fact that more Kuhn monomers in the polymer coil cause greater energy gain from the adsorption. Specifically, divided ΔF_{tot} of Figure 3.11 into two parts: $F_{a,\,p}$ and $F_{p,\,p}$. Figure 3.12 shows respectively the variation of $F_{a,\,p}$ and $F_{p,\,p}$ for varied C_p and D for PVA1, PVA2 and PVA3. Comparing these three PVA, PVA1 with higher molar weight has the deeper free energy $F_{a,\,p}$. This adsorption energy gain decreases rapidly when PVA's molar weight gets smaller for PVA2 and PVA3, see Figure 3.12a. Meanwhile, in Figure 3.12b the $F_{p,\,p}$ value is similar for all PVA which is just shifted to a higher polymer concentration. Therefore, the influence of the polymer molar weight can be explained by the fact that more Kuhn monomers in the polymer coil cause greater energy gain from the adsorption.
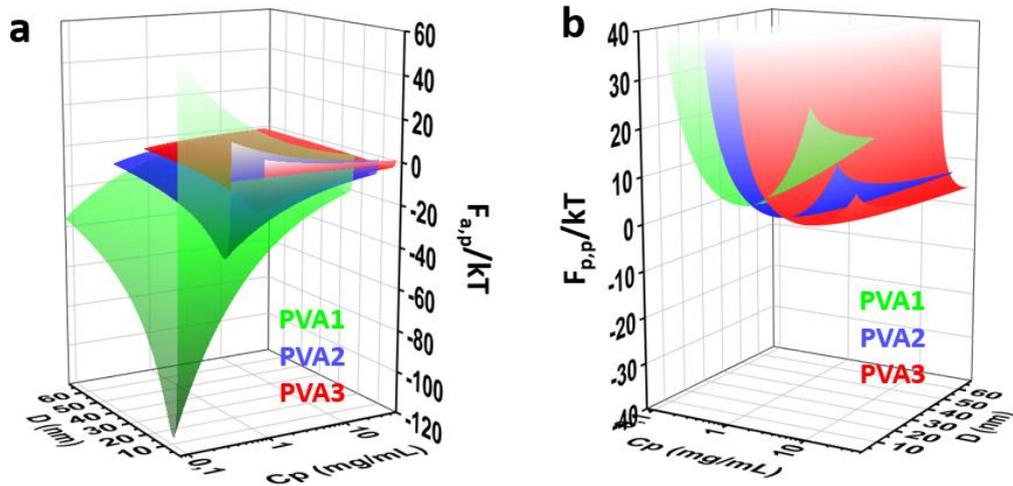
Figure 3.12 | Calculated free energy of (**a**) $F_{a,p}$ and (**b**) $F_{p,p}$ plotted as a function of polymer concentration C_p (mg/mL) and adsorbed thickness D (nm) for PVA1, PVA2 and PVA3.

It is usually difficult to discuss the free energy change of an irreversible process. For further discussion, we will focus only on the situation when $\Delta F_{tot} = 0$, so that the adsorption occurrence takes time and maintains equilibrium. In this case, the adsorbed thickness D depending on C_p is a loop curve leading two possible trends for D at the same polymer concentration in Figure 3.11. On the upper side of the curve, the D value beyond the R_{end} of free-standing polymer coils is thermodynamically impossible. On the bottom side of the loop curve, the D value remains stable and becomes slightly higher than 1.7 nm under the protruding part's tensile stress effect. Therefore, only the bottom side corresponding to the D value accurately reveals the variations in the adsorbed polymer chain and will be considered for further discussion.
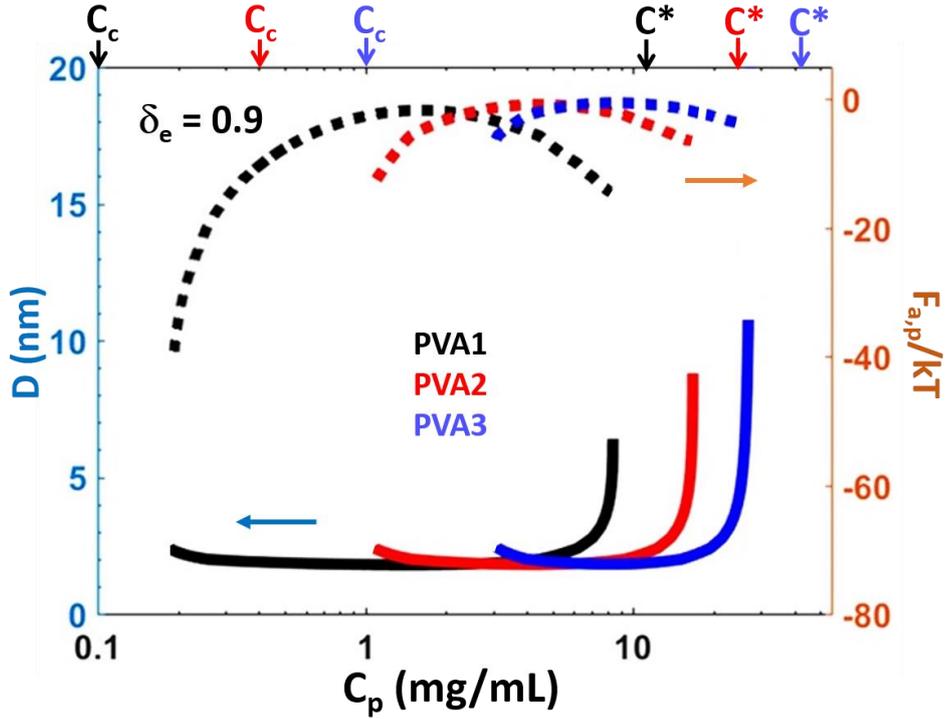
Figure 3.13 | Calculated adsorbed thickness D and free energy of adsorbed part $F_{a,p}$ in a partially adsorbed chain plotted as functions of the polymer concentration C_p when $\Delta F_{tot} = 0$. The result of PVA1 (black curves), PVA2 (red curves), and PVA3 (blue curves) are plotted. The theoretical values of C_c and C^* of three PVA are indicated with the arrows in relative colors on the top.

Figure 3.13 plots the free energy of the adsorbed part of the polymer coils and its thickness as a function of C_p for reversible transformation. In this C_p regime, $F_{a,\,p}$ is always negative, which is the driving force for the adsorption process and shows a peak for all three PVA. In Figure 3.13, $F_{a,\,p}$ first increases, meaning that the energy gain decreases, and the adsorption becomes more difficult, which explains why the graphene concentration decreases when C_p increases slightly higher than C_c. As C_p increases, $F_{a,\,p}$ has a maximum value corresponding to the lowest graphene concentration. $F_{a,\,p}$ eventually decreases again while the graphene concentration increases until C^*. Figure 3.13 is compared with the middle section of Figure 3.1b.

Critical concentration C_c

In our model, the concentration C_c is the key parameter to cause highly concentrated graphene dispersion at the molecular level in the polymer matrixes. In equation 3.21, $N^*= N$ make us to evaluate the critical concentration C_c:

$$C_c = 3.18 N^{-9/4} b^{-3} \delta_e^{-9/8} M \qquad (3.22)$$

C_c corresponds to the onset point where the adsorbed polymer chain starts to connect with its neighbors. Theoretically, the adsorption free energy gain is maximum at C_c where high graphene concentration was experimentally obtained. C_c is predominated by the energy interaction parameter δ_e and polymer molar weight M. In Figure 3.14, for a given molar weight of polymer, the C_c value decreases when δ_e increases.
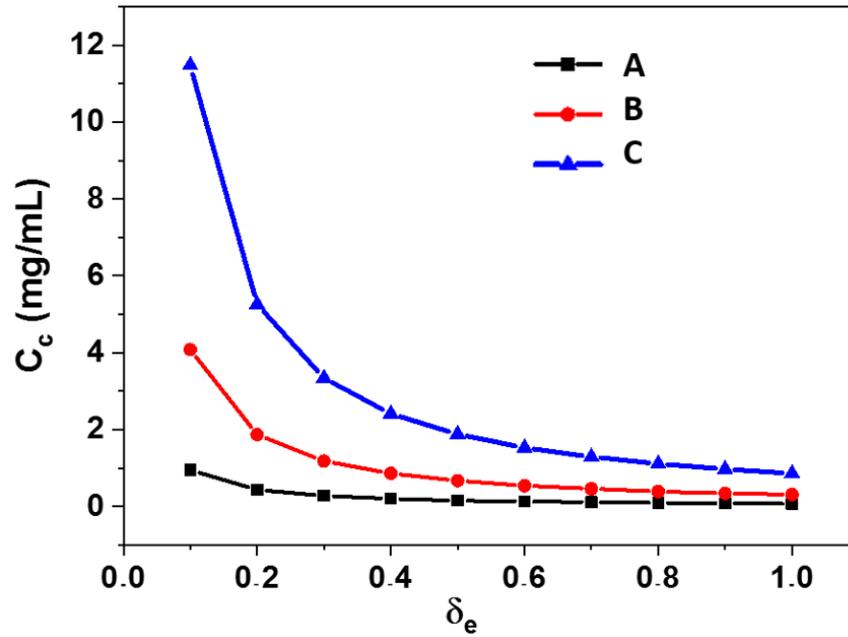
Figure 3.14 | Calculated C_c plotted as functions with the energy interaction parameter δ_e. And The influence of molar weight of polymer on C_c. Taking examples of three molar weight: *A* with 130000 g/mol, *B* with 31000-50000 g/mol and *C* with 13000-23000 g/mol.

Indeed, the stronger interaction between polymer and adsorbent gives rise to a thin adsorption thickness D according to equation 3.14. As a result, the longitudinal size of adsorption part $R_{//}$ becomes larger by polymer spreading out to a greater extent, so that the adsorbed chains starting to contact each other at a lower C_c. Besides, for the same polymer, a lower molar weight means less Kuhn monomers in polymer coil as well as a smaller adsorption size $R_{//}$. Therefore, the adsorbed chains start to contact to each other at a higher C_c. Here we firstly propose the critical concentration C_c definition and its calculation method, which gives the first clue for the polymer/ solvent couple selection and for the optimization of graphene/ polymer ratio in the nanocomposite.

For graphene/PVA/water ternary systems, the critical concentrations C_c of PVA1, PVA2, and PVA3 are calculated to be 0.1, 0.4, and 1.0 mg/mL, respectively (Table 3.4). The experimental values are slightly higher than the calculated values. One reason for this discrepancy could be that we assumed water is a good solvent for PVA to simplify this discussion. However, the Flory interaction parameters of PVA/water are 0.494 in the volume fraction range of 0-0.15 under 25°C. [40] This value very close to 0.5 creates indistinct limitations between good solvents and "theta" solvents. For the record, in good solvents, the excluded volume of a Kuhn monomer v is approximatively equal to b^3, and the size of one coil is $R_{end} = bN^{0.6}$. But in theta solvents, $v \approx 0$ and $R_{end} = bN^{0.5}$. Therefore, the assumption may lead to an overestimation of the coil size, especially in "very dilute" regime, which shifts C_c to a lower concentration. Nevertheless, this model predicts the C_c value reasonably.

Table 3.4 | Comparison of the theoretical and experimental results of C_c and C^*

Samples	C_c, mg/mL		C^*, mg/mL	
	t^a	e^b	t^a	e^b
PVA1	0.1	~0.3	11.8	~10.0
PVA2	0.4	~1.3	24.8	~21.3
PVA3	1.0	~2.9	41.7	~37.5

[a]Theoretical results.

[b]Experimental results.

There are some limitations to this model. We cannot simulate the free energy change close to C_c and C^*. When C_p is slightly higher than C_c, the protruding part contains only a few monomers that cannot be extended to the size $R_{//}$. Otherwise, the energy cost for conformation adaptation is infinitely high. On the other hand, when C_p is close to C^*, the gradually reduced space for each coil cannot contain the increasing protruding monomers while maintaining $v = b^3$. Otherwise, the energy cost for conformation adaptation is also infinitely high. Fortunately, the two small gaps located at the two extremes of $C_c < C_p < C^*$ range in Figure 3.13 do not affect the trend.

This model can be easily extended to all types of 2D material/polymer/solvent systems if only physisorption happens on the absorbent. At the same molar weight, the influence of different materials is characterized by δ_e as shown in Figure 3.15. When δ_e is too small, $\delta_e = 0.1$, adsorption is impossible (Figure 3.15a). Adsorption is easier for ternary systems with high δ_e values since ΔF_{tot} is deeper, demonstrating a higher transformation potential (see equation 3.4).

Therefore, obtaining a value of δ_e as high as possible via choosing or modifying 2D materials/polymer/solvent combinations could be a way to achieve a high concentration dispersion of layer materials for specific applications.
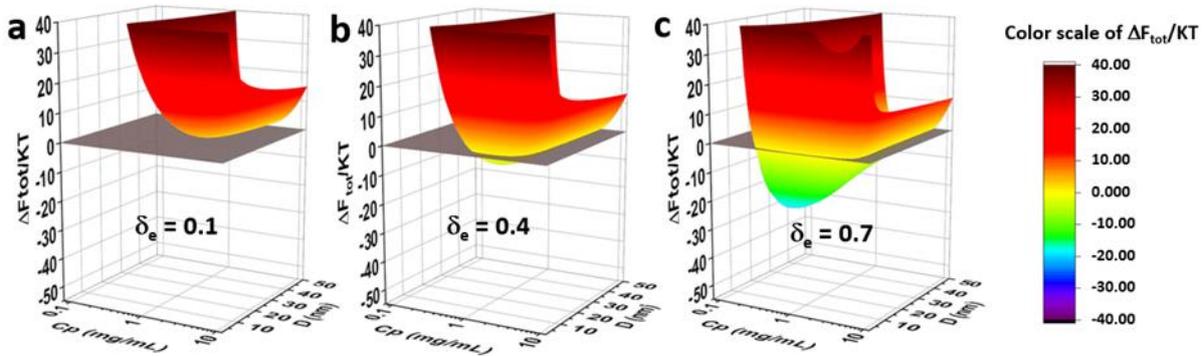
Figure 3.15 | Calculated free energy ΔF_{tot} plotted as a function of the polymer concentration C_p (mg/mL) and adsorbed thickness D (nm). Fixed molar weight M with 130000 g/mol and varying adsorption energy parameters: (**a**) $\delta_e = 0.1$, (**b**) $\delta_e = 0.4$, and (**c**) $\delta_e = 0.7$.

3.6 Summary

In this chapter, three different molar weight of PVA as stabilizes have been used to disperse pristine graphene in water. With increase of PVA concentration, the pristine graphene contents in solutions for all those three PVA have showed similar trend, in which there were two peaks of graphene contents located at C_c and C^* of PVA solution. Based on Flory theory we have proposed a model to describe the process of polymer coils adsorbing onto the graphene surface in "dilute" regime of polymer solution. From the model, an equation has been developed to calculate the free energy variation of this process. Those provide powerful tools to design graphene dispersion at the molecular level into polymer matrixes by noncovalent physisorption. Moreover, we first introduced the so-called critical concentration, C_c in which a high graphene content in low concentration of polymer matrixes can be achieved, which is of interest for fabrication of graphene/ polymer nanocomposites. For example, we have prepared a conductive flexible membrane using the graphene/PVA1/water solution at C_c, this membrane with 47 wt.% graphene exhibits an electrical conductivity of approximately 10 S/m.

References

1. Choi, E.-Y., Choi, W. S., Lee, Y. B. & Noh, Y.-Y. Production of graphene by exfoliation of graphite in a volatile organic solvent. *Nanotechnology* **22**, 365601 (2011).

2. Park, S. *et al.* Colloidal Suspensions of Highly Reduced Graphene Oxide in a Wide Variety of Organic Solvents. *Nano lett.* **9**. 1593-1597 (2009)

3. Carrasco, P. M. *et al.* High-concentration aqueous dispersions of graphene produced by exfoliation of graphite using cellulose nanocrystals. *Carbon* **70**, 157–163 (2014).

4. Liang, Y. T. & Hersam, M. C. Highly Concentrated Graphene Solutions via Polymer Enhanced Solvent Exfoliation and Iterative Solvent Exchange. *Journal of the American Chemical Society* **132**, 17661–17663 (2010).

5. Kim, H., Abdala, A. A. & Macosko, C. W. Graphene/Polymer Nanocomposites. *Macromolecules* **43**, 6515–6530 (2010).

6. Du, J. & Cheng, H.-M. The Fabrication, Properties, and Uses of Graphene/Polymer Composites. *Macromolecular Chemistry and Physics* **213**, 1060–1077 (2012).

7. Khan, U., May, P., O'Neill, A. & Coleman, J. N. Development of stiff, strong, yet tough composites by the addition of solvent exfoliated graphene to polyurethane. *Carbon* **48**, 4035–4041 (2010).

8. May, P., Khan, U., Hughes, J. M. & Coleman, J. N. Role of Solubility Parameters in Understanding the Steric Stabilization of Exfoliated Two-Dimensional Nanosheets by Adsorbed Polymers. *The Journal of Physical Chemistry C* **116**, 11393–11400 (2012).

9. Israelachvili, J. N. *Intermolecular and Surface Forces*. (Academic Press, 2015).

10. SATO, T., T, S. & R, R. STABILIZATION OF COLLOIDAL DISPERSIONS BY POLYMER ADSORPTION. *SURFACTANT SCI. SER.* **9**, 166 (1980).

11. Napper, D. H. Steric stabilization. *Journal of Colloid and Interface Science* **58**, 390–407 (1977).

12. De Gennes, P. G. Polymer solutions near an interface. Adsorption and depletion layers. *Macromolecules* **14**, 1637–1644 (1981).

13. De Gennes, P. G. Polymers at an interface. 2. Interaction between two plates carrying adsorbed polymer layers. *Macromolecules* **15**, 492–500 (1982).

14. Wajid, A. S. *et al.* Polymer-stabilized graphene dispersions at high concentrations in organic solvents for composite production. *Carbon* **50**, 526–534 (2012).

15. Lotya, M. *et al.* Liquid Phase Production of Graphene by Exfoliation of Graphite in Surfactant/Water Solutions. *Journal of the American Chemical Society* **131**, 3611–3620 (2009).

16. Kim, J. *et al.* Direct exfoliation and dispersion of two-dimensional materials in pure water via temperature control. *Nature Communications* **6**, (2015).

17. Hernandez, Y. *et al.* High-yield production of graphene by liquid-phase exfoliation of graphite. *Nature Nanotechnology* **3**, 563–568 (2008).

18. Ying, Qicong. & Chu, Benjamin. Overlap concentration of macromolecules in solution. *Macromolecules* **20**, 362–366 (1987).

19. Cherif, E., Zoghlami, O. & Othman, T. Investigation of critical concentrations of poly (vinyl pyrrolidone) in N, N-dimethylformamide by a viscosity technique. *Physics and Chemistry of Liquids* **53**, 75–83 (2015).

20. Yang, H. *et al.* Viscometric study of polyvinyl alcohol in NaCl/water solutions ranged from dilute to extremely dilute concentration. *European Polymer Journal* **37**, 1939–1942 (2001).

21. Dondos, A. & Tsitsilianis, C. Viscometric study of extremely dilute macromolecular solutions: Critical concentration c and the intrinsic viscosity of the polystyrene through scaling laws. The values of the Huggins constant. *Polymer International* **28**, 151–156 (1992).

22. Meng Kok, C. & Rudin, A. A semi-empirical method for prediction of critical concentrations for polymer overlap in solution. *European Polymer Journal* **18**, 363–366 (1982).

23. Weissberg, S. G., Simha, R. & Rothman, S. Viscosity of dilute and moderately concentrated polymer solutions. *Journal of Research of the National Bureau of Standards* **47**, 298 (1951).

24. Liu, M., Cheng, R. & Qian, R. Effect of solution concentration on the gelation of aqueous polyvinyl alcohol solution. *Journal of Polymer Science Part B: Polymer Physics* **33**, 1731–1735 (1995).

25. Cooper, A. J., Wilson, N. R., Kinloch, I. A. & Dryfe, R. A. W. Single stage electrochemical exfoliation method for the production of few-layer graphene via intercalation of tetraalkylammonium cations. *Carbon* **66**, 340–350 (2014).

26. Stobinski, L. *et al.* Graphene oxide and reduced graphene oxide studied by the XRD, TEM and electron spectroscopy methods. *Journal of Electron Spectroscopy and Related Phenomena* **195**, 145–154 (2014).

27. Al-Gaashani, R., Najjar, A., Zakaria, Y., Mansour, S. & Atieh, M. A. XPS and structural studies of high-quality graphene oxide and reduced graphene oxide prepared by different chemical oxidation methods. *Ceramics International* **45**, 14439–14448 (2019).

28. Lămătic, I.-E., Bercea, M. & Morariu, S. INTRINSIC VISCOSITY OF AQUEOUS POLYVINYL ALCOHOL SOLUTIONS. *Revue Roumaine de Chimie* **54** (11-12), 981-986 (2009).

29. Hong, P.-D., Chou, C.-M. & He, C.-H. Solvent effects on aggregation behavior of polyvinyl alcohol solutions. *Polymer* **42**, 6105–6112 (2001).

30. Du, D.-X., Zuo, J., An, Y.-L., Zhou, L. & Liu, Y. Study of viscosity abnormality of PS/toluene solution in extremely dilute concentration regime. *Journal of Applied Polymer Science* **102**, 4440–4446 (2006).

31. Rubinstein, M. & Colby, R. H. *Polymer physics*. (Oxford Univ. Press, 2010).

32. O'Shaughnessy, B. & Vavylonis, D. Irreversible adsorption from dilute polymer solutions. *The European Physical Journal E* **11**, 213–230 (2003).

33. Silberberg, A. Adsorption of Flexible Macromolecules. IV. Effect of Solvent–Solute Interactions, Solute Concentration, and Molecular Weight. *The Journal of Chemical Physics* **48**, 2835–2851 (1968).

34. *Hansen solubility parameters: a user's handbook*. (CRC Press, 2007).

35. O'Neill, A., Khan, U., Nirmalraj, P. N., Boland, J. & Coleman, J. N. Graphene Dispersion and Exfoliation in Low Boiling Point Solvents. *The Journal of Physical Chemistry C* **115**, 5422–5428 (2011).

36. Park, S. *et al.* Colloidal Suspensions of Highly Reduced Graphene Oxide in a Wide Variety of Organic Solvents. *Nano Letters* **9**, 1593–1597 (2009).

37. Sukhishvili, S. A. *et al.* Diffusion of a polymer 'pancake'. *Nature* **406**, 146–146 (2000).

38. Gennes, P.-G. de & Gennes, P. P.-G. *Scaling Concepts in Polymer Physics*. (Cornell University Press, 1979).

39. Stuart, M. A. C., Hoogendam, C. W. & Keizer, A. de. Kinetics of polyelectrolyte adsorption. *Journal of Physics: Condensed Matter* **9**, 7767–7783 (1997).

40. Sakurada, I., Nakajima, A. & Fujiwara, H. Vapor pressures of polymer solutions. II. Vapor pressure of the poly (vinyl alcohol)-water system. *Journal of Polymer Science* **35**, 497–505 (1959).

Chapter 4

Effect of the oxidation degree of GO on its dispersion in PVA/water solution

Graphite oxide is a graphite derivative displaying different oxygen-based functional groups that can form hydrogen bonds with some polymers such as PVA. Compared to pristine graphite (PG), graphite oxide also has strong interactions with water, resulting in a higher concentration of graphene oxide (GO) nanosheets in the dispersion solution. Thus, tailoring the oxygen content on graphene is beneficial to form hybrid composites with enhanced performance. In this chapter, two GO with different oxidation degree will be prepared to explore the effect of oxidation degree of GO on its dispersion in PVA/water solution.

4.1 Introduction

In general, for a two-phase system, a maximized solubility is obtained when the solubility parameters of solute and solvent match. [1] In the case of graphene/solvent, a higher graphene concentration is obtained by choosing small difference of solubility parameters between graphene and solvent. [2] This simple framework used to guide the solvent choice has been well proved in most situation.

When a solvent poorly disperses graphene, such as water, a polymer can be added to the system as a stabilizer to assist the dispersion of graphene in such a solvent. The corresponding stabilization mechanism involving polymer physisorption in the three-phase system was carefully discussed in the last chapter. Interestingly, we have found that the adsorption parameter δ_e which is used to calculate the adsorption free energy $F_{ads} = -\delta_e kT$, plays an important role during the polymer adsorption process. δ_e can be understood as a combination of interactions for graphene, polymer and solvent. When $0 < \delta_e \leq 1$, the adsorption is weak, when $\delta_e > 1$, the adsorption is strong, whereas when $\delta_e < 0$, the adsorption will not occur. [3] According to the last chapter, δ_e is closely related to the component materials' intrinsic properties which can be characterized by their solubility parameters.

94

$$\delta_e = \frac{v_o}{kT}[(\delta_s - \delta_g)^2 - (\delta_p - \delta_g)^2 - (\delta_p - \delta_s)^2] \quad\quad\quad (4.1)$$

Equation 4.1 is coming from equations 3.7 and 3.10. Understanding of the effect of component materials' intrinsic properties on δ_e is important. Actually, it can help us to choose the optimized composition of graphene/polymer/solvent system according to their aimed applications. May et al. have discussed the effect of Hildebrand solubility parameters on graphene dispersion in the three-phase system, which is achieved by choosing different polymer in the same solvent. [4] However, Hildebrand solubility parameter is rather relevant for non-polar interactions, which is only Van der Waals forces between species, meaning that this parameter is not adapted to mixtures displaying strong polar species with hydrogen bonds. Hansen solubility parameters (HSPs) consider the forces between species, including (atomic) dispersion force, (molecular) permanent dipole - permanent dipole forces, and molecular hydrogen bonding (electron exchange), [5] which can be used to calculate δ_e, and help us to understand the interaction among strong polar species.

In this chapter, graphene oxide (GO) with different oxidation degree, GO1 and GO2, have been prepared using modified Hummer's method, which has been presented in chapter 2. As already written, GO nanosheets presenting oxygen-functional groups could generate hydrogen bonding with PVA when GO nanosheets are dispersed in water via liquid-phase exfoliation method. Therefore, the effect of hydrogen bonding on the interactions between GO, PVA and water during the liquid-phase exfoliation will discuss in this chapter. Pristine graphite (PG) with almost zero oxidation degree represents reference.

4.2 Characterizations of PG, GO1 and GO2

4.2.1 Morphology analysis

Scanning Electron Microscope (SEM) measurements are used to assess the morphology of the raw PG flakes as well as the GO with different oxidation degree. Figure 4.1a shows the raw PG flakes' morphology. By measuring 50 flakes' size and 30 flakes' thickness, Figure 4.1b and c show that most of PG flakes have about 600-700 µm length and 15-20 µm thickness. The morphology of GO1 is presented in Figure 4.1d, and the same statistical analysis to their size and thickness are presented in Figure 4.1e and f. By comparing with PG flakes, GO1 ones display smaller sizes mostly observed at 500-600 µm length, and their thickness significantly

95

increase to 60-70 µm, even > 100 µm. The light oxidation, corresponding to a graphite: KMnO$_4$ ratio of 4:1, is supposed to introduce a small amount of oxygen functional groups at the edge of the GO1 sheets and some defects within the sheets, [6] which cause an expansion of the layers and part of GO1 flakes are broken. Figure 4.1g and h show the morphology of GO2 with a deeper oxidation, corresponding to a graphite: KMnO$_4$ ratio of 1:3, we can see that its layered form is lost and that all flakes agglomerate after dying.
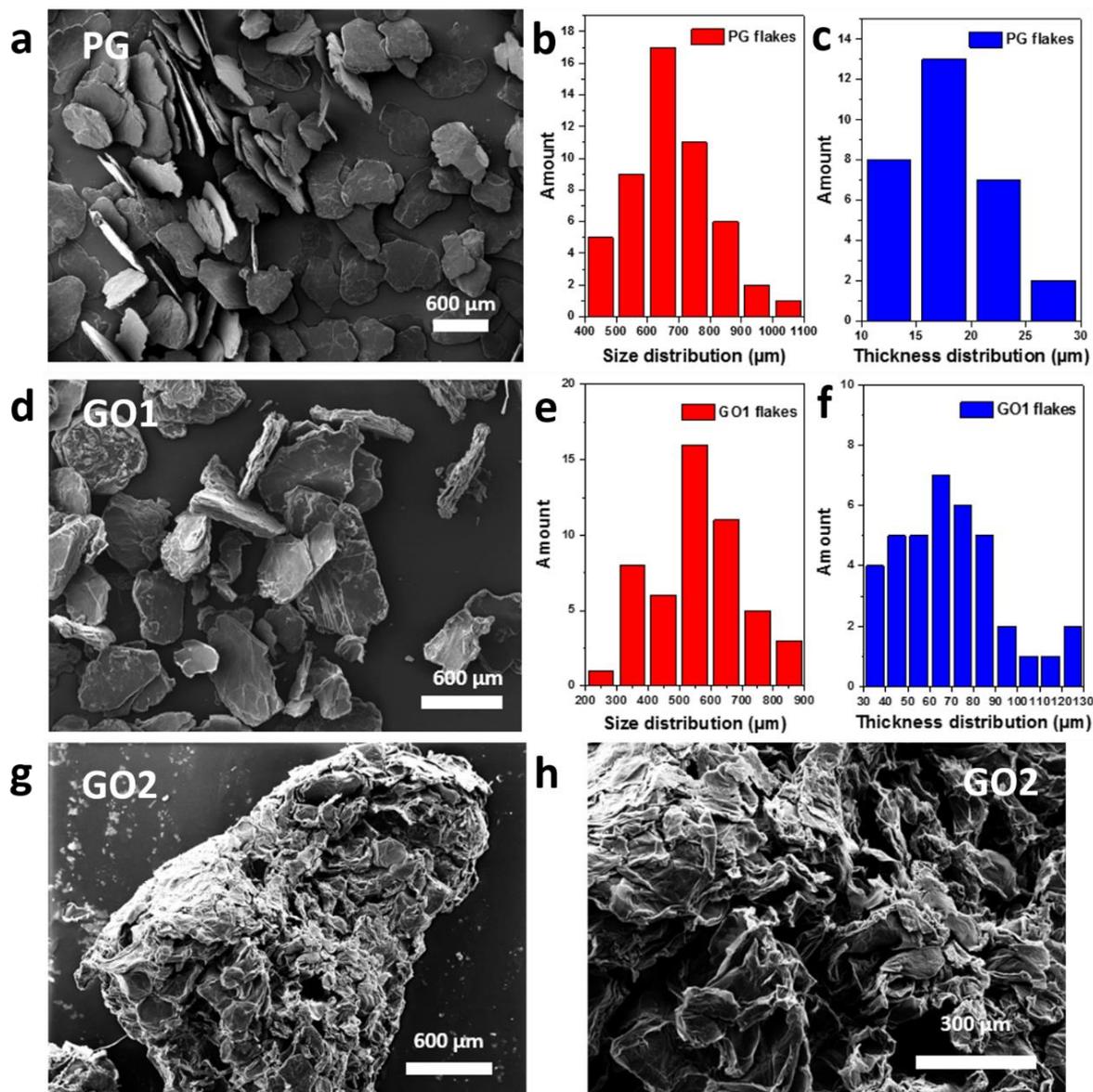
Figure 4.1 | SEM images of (**a**) PG flakes, (**d**) GO1 flakes, (**g& h**) GO2 aggregates. The size and the thickness contributions of (**b& c**) PG flakes and (**e& f**) GO1 flakes measured by Digital Micrograph

4.2.2 Structural analysis

Figure 4.2 shows the comparison of XRD patterns recorded on raw PG and both types of prepared GO. The raw PG presents a main thin peak at $2\theta = 26.4°$ for the (002) planes with d-spacing of 0.335 nm. [7] A broaden peak at $2\theta = 25.8°$ is observed for GO1, with an interlayer spacing d-spacing of 0.345 nm. Light oxidation causes a graphite lattice distortion and an increase in the interlayer distance, which comes from of C=C bonds breakage and the oxygen-containing functional groups presence. [8] Furthermore, the XRD pattern recorded on GO2 shows two reflection peaks at 24.4° and ~10°, which indicates the production of GO with a (002) d-spacing in plane up to 0.365 nm. This two broaden peaks are related to the presence of more oxygen containing groups within the GO sheets, and a transition from an ordered to a disordered structure. [8,9]
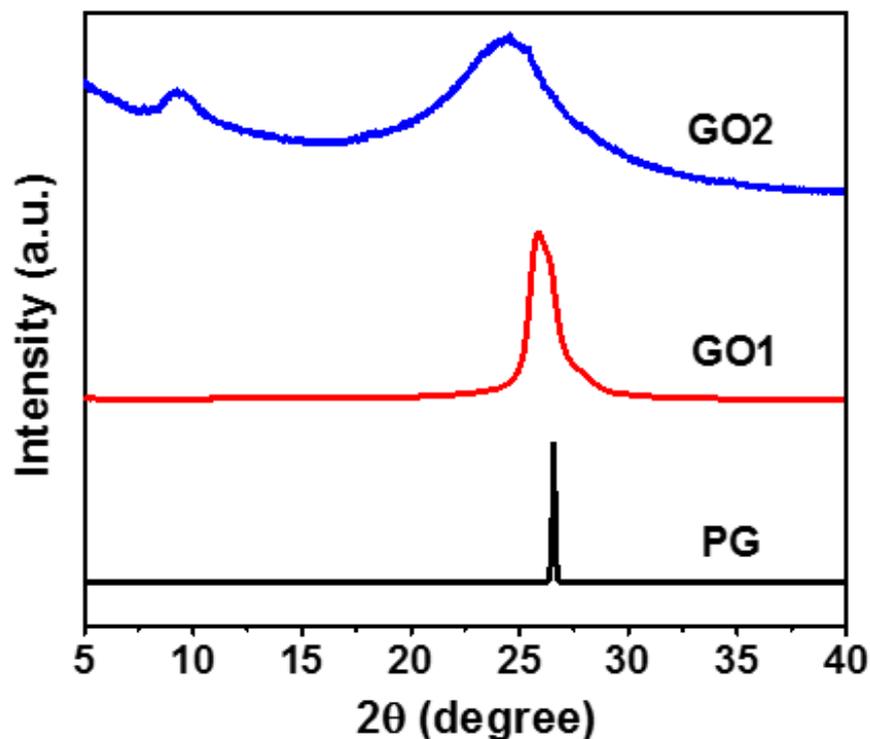
Figure 4.2 | X-ray diffraction pattern of PG, GO1 and GO2.

Raman spectra characterization can be used to estimate the carbon materials' physic properties like crystallite size, defects and number of layers. [7,10] Figure 4.3 presents the Raman spectra of raw PG and both types of GO. There is a typical intense G band at 1570 cm^{-1} for PG sample, which is attributed to the order scattering of E_{2g} mode. [11] A small D band at 1355 cm^{-1} is also

observed, which shows the presence of some defects in the raw PG. Beside, another peak is visible at ~2700 cm^{-1} which is characteristic of the stacking order and the number of layers in graphene. [12] In comparison with raw PG, the D band of GO1 and GO2 displays an apparently higher intensity. This variation is ascribed to the introduction of oxygen-containing functional groups within the GO samples. [13] On the other hand, the intensity of the 2D band becomes broader, demonstrating a decrease in the stacking order due to the oxidation process. The Raman intensity ratio I_D/I_G can be used to evaluate the GO samples' oxidation degree. For our samples, the value of I_D/I_G are 0.09 (PG), 0.76 (GO1), and 0.90 (GO2).
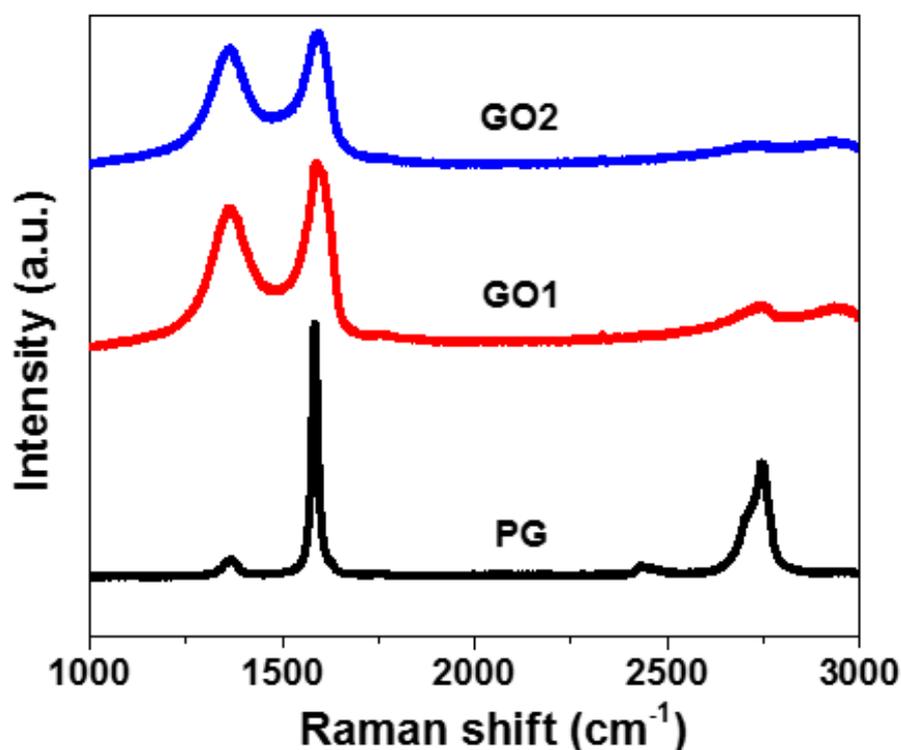
Figure 4.3 | Raman spectra of PG, GO1 and GO2.

Figure 4.4 shows FT-IR spectra of raw PG and both types of GO. Obviously, GO1 and GO2 present a strong and broad peak where two bands overlap: the one at ~3500 cm^{-1} which corresponds to the -OH functional group stretching, and the second at ~3400 cm^{-1} attributed to the hydrogen-bonded water (H-O-H) symmetric stretching. [8] In addition, both GO spectra display peaks at 1720 cm^{-1}, 1530 cm^{-1}, 1215 cm^{-1}, 1045 cm^{-1}, and 850 cm^{-1} characteristic of C=O stretching mode (carboxyl/carbonyl), C=C stretching in graphite domains, C-O-C stretching, C-O stretching, and =C-H bond, respectively. [7,8,11,14–17] As expected, neither the

large signal at ~3450 cm^{-1} nor signals relative to C=O, C-O-C and C-OH are observed on PG sample.
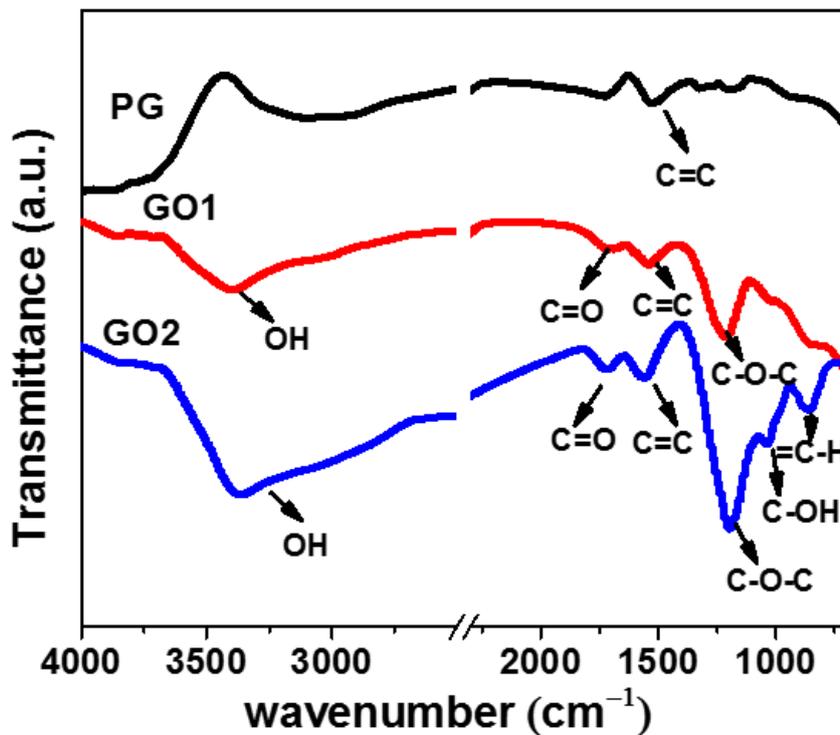
Figure 4.4 | FT-IR spectra of PG, GO1 and GO2.

4.2.3 Elemental analysis

Chemical analyses by means of EDS analyses are also performed on the three samples. SEM images and EDS elemental mapping of C and O obtained on each sample are proposed in Figure 4.5. As expected, the PG surface (Figure 4.5a1 and 2) is composed almost entirely of carbon. On the opposite, the presence of oxygen is clearly demonstrated on GO samples, and from sample GO1 to GO2 (Figures 4.5b2 and 4.5c2), meaning from the least to the most oxidized GO, we can see that the oxygen seems increase especially at the edges of GO2 sample, demonstrating that the edges are more easily oxidized when graphite undergoes a deeper oxidation treatment.
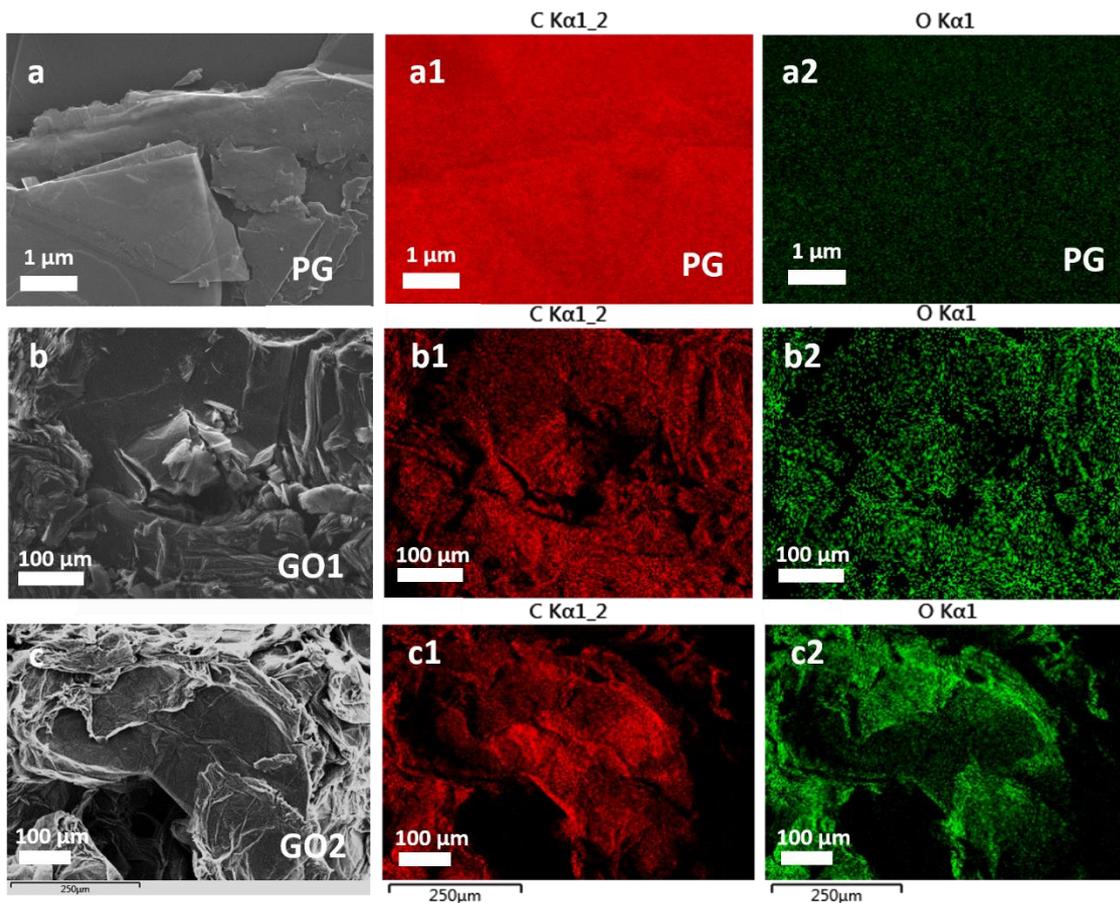
Figure 4.5 | SEM images and EDS elemental mapping of C and O of the samples. (**a**) PG, (**b**) GO1, and (**c**) GO2

In order to accurately confirm the element contents and their chemical states, XPS measurement is performed additionally. All spectra display C1s and O1s peaks at around 286 and 532 eV respectively. The C1s peak deconvolution allows identifying five carbon environments. The majority contribution at 284.4 eV, is attributed to C=C environment from the carbon hexagonal structure. In addition to C=C, the carbon region (282-292 eV) also shows the presence of C-C (285.5 eV), C-O (286.4 eV), C=O (287.4-287.5 eV), O=C-O (289.0-289.1 eV) and π to π* satellite bonds (291.4-291.5 eV). [18,19] Concerning the O1s peak presents in the region of 530-536 eV, it can be deconvoluted as O-C=O (531.3-531.4 eV), C=O (532.5 eV), C-O-C (533.8 eV), and chemisorbed oxygen (535.3 eV) species. [14,15] (see Figure 4.6)
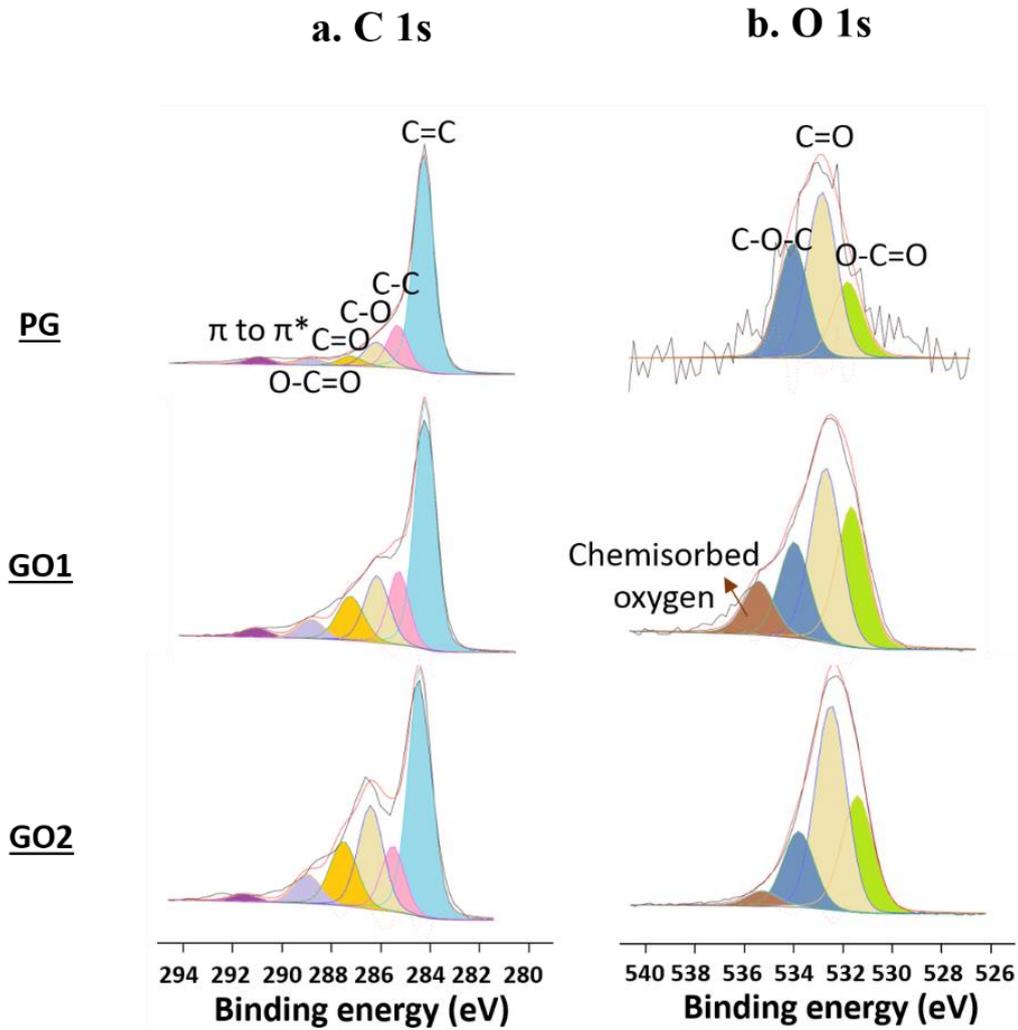
Figure 4.6 | XPS result of PG, GO1 and GO2: (**a**) C 1s and (**b**) O 1s

By measuring the area of each peak in the three samples, the chemical composition can be approximately determined. Thus, the raw PG is composed of 97.8% of carbon and 2.2% of oxygen. GO1 and GO2, as to them, are composed of 80.5% of C and 19.5% of O, and 64.4% of C and 33.4% of O, respectively. The increase in the oxygen content with decreasing the weight ratio of PG:KMnO$_4$ is now clearly proved. All information has been resumed in Table 4.1.

Table 4.1 Fitting details in C 1s and O 1s of graphite.

	Peaks	C=C	C-C	C-O	C=O	O=C-O	π to π*	O-C=O	C=O	C-O-C	Chemisorbed oxygen
					C 1s					**O 1s**	
PG	BE, eV	284.4	285.5	286.4	287.4	289.0	291.4	531.3	532.5	533.8	
	FWHM	1.0	1.0	1.2	1.3	1.3	1.3	1.5	1.5	1.5	
	Perc, %				97.8					2.2	
GO1	BE, eV	284.4	285.5	286.4	287.5	289.1	291.4	531.4	532.5	533.8	535.3
	FWHM	1.0	1.0	1.2	1.3	1.3	1.3	1.5	1.5	1.5	1.5
	Perc, %				80.5					19.5	
GO2	BE, eV	284.4	285.5	286.4	287.5	289.0	291.5	531.4	532.5	533.8	535.3
	FWHM	1.1	1.1	1.2	1.3	1.3	1.3	1.5	1.5	1.5	1.5
	Perc, %				64.6					33.4	

4.3 Results and discussion

4.3.1 Results
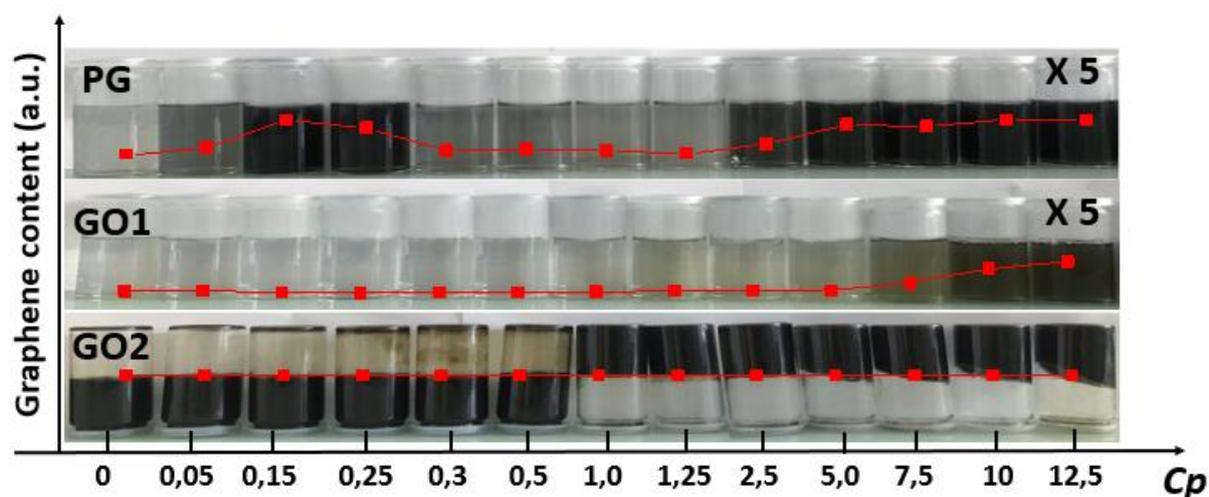
Figure 4.7 | Images of the colloid of PG, GO1 and GO2 dispersing in PVA solution after dilution 5 times (x5) for PG and GO1, and no dilution for GO2. Red curves represent UV-Visible light absorption of PG, GO1, and GO2 at λ = 660 nm curve versus PVA concentrations

Liquid-phase exfoliation of raw PG, GO1 and GO2 in PVA/water solution with varying PVA concentration has been carried out. (more details in the synthesis can be found in chapter 2) Figure 4.7 shows images of all solutions prepared from PG, GO1 and GO2 with increasing PVA concentration. The added red curves of PG and GO1 correspond to UV-Visible absorption intensity of each specimen as a function of the polymer concentration measured at wavelength $\lambda = 660$ nm. For both series relatives to PG and GO1, we can see that the color intensity varies according to the polymer concentration C_p. Corresponding UV-visible absorption spectroscopy data are given on Figure 4.8. The behavior of PG in PVA solution with different concentration follows the same trend as the results discussed in chapter 3, meaning that the different sonication methods used, sonic bath or sonic tip, has no influence on LPE of graphite in water assisted with PVA. However, it appears preferable to use a sonic tip to save time and increase the data reproducibility. Actually, the use of a sonic bath needs a longer sonication and since the energetic distribution in the bath is unevenly, the reproducibility of the experiments can be affected. By now considering results obtained with the GO1 series, we can see that the content of GO1 dispersed in solution overall increases with the PVA concentration. Moreover, unexpectedly, in the same experimental conditions, the final amount of GO1 always remains much lower than the PG one. This trend will be discussed below.

Figure 4.8 presents the UV-Visible absorption intensity measurements performed on both series of PG and GO1 in PVA solution. To avoid the influence of the scattering phenomenon, we have used the signal at a $\lambda = 660$ nm wavelength. [4] The absorption intensity is linearly proportional to the suspended species concentration: $A/l = <\alpha>C$ (Beer-Lambert's law). A is the optical absorption intensity, I is the passage length (10 mm), and $<a>$ is the extinction coefficient. Our study focused on the variation of PG or GO concentration with C_p in solutions, which is positively correlated with the absorption intensity.
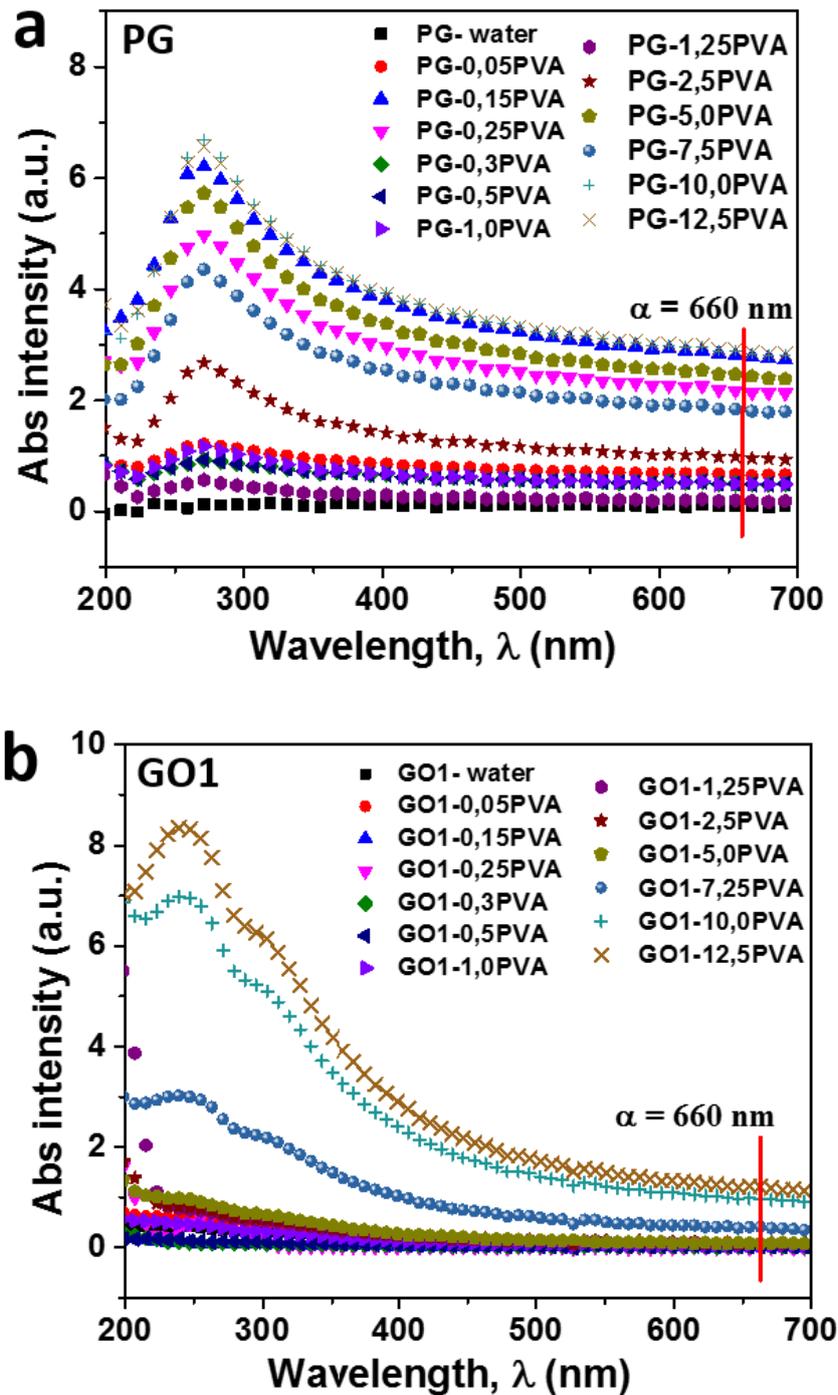
Figure 4.8 | The UV-visible absorption spectroscopy of solution of (**a**) PG and (**b**) GO1 dispersing in PVA/water with different concentration.

Unlike GO1, at any time, GO2 is well dispersed in water, and the addition of different amount of PVA has no influence on GO2 content in the final dispersion. Observations confirm that GO2 are well dispersed in solution without any precipitation occurring after the centrifugation process. Interestingly, there is a sol-like to gel-like transition phenomenon occurring at 1

104

mg/mL PVA colloid containing ~4.5 mg/mL GO2 (~81.8wt.% GO2). Figure 4.7 shows a row of inverted bottles containing the GO2/PVA/water mixture. When the PVA concentration is lower than 1 mg/ml, the mixture retains fluidity and is sol-like state. When it is higher than 1 mg/mL, the mixture loses its fluidity and becomes gel-like state.

4.3.2 Discussion

In the last chapter, we have demonstrated that the polymer-assisted 2D materials' dispersion can be divided into two steps: 1) 2D materials are exfoliated from raw materials; 2) polymers adsorb on nanosheets and stabilize them by steric forces. From PG flakes, the excess amount of graphene nanosheets can be obtained after ultrasonic sonication in PVA solutions with different concentrations. Graphene content is mainly governed by step 2, in which the nanosheets are stabilized to varying degrees according to their adsorption free energy of the whole system.

As we have just seen above, in this study, GO1 behaves much differently, since the GO1 content dramatically decreases and that GO1 nanosheets cannot be stabilized in most PVA solutions. One plausible reason is that GO1 flakes are hardly exfoliated at step 1. To corroborate this hypothesis, we have undertaken to characterize the sheets morphology after the dispersion. In that way, Figure 4.9 shows the digital and SEM images of the GO1 and PG sediments. Both are obtained by drying the bottom sediments separated from the PG or GO1/PVA/water mixture after 30 min tip sonication and 90 min centrifugation at 1500 RMP, respectively. PG sediments show a flake-destroyed morphology that proves that the nanosheets were well exfoliated even if they re-agglomerate after the drying. On the contrary, GO1 sediments keep a flaky form as if they have never been exfoliated. By comparing the size and the thickness of the GO1 sediment in Figure 4.9 b, c with the initial GO1 in Figure 4.1 e, f, we can see that their size is almost unchanged, whereas a part of flakes has increased in thickness, up to 300-400 µm (against 70-80 µm).

As conclusion, GO1 are non-exfoliated, only the thickness has increased after the LPE process. This could be attributed to the hydrogen bond that form between layers due to the oxygen-containing functional groups. In that case, the sonication energy cannot overcome the Van de Waals force as well as the stronger hydrogen bond between layers, demonstrating that GO1 is not relevant for dispersion by using the LPE process, which is limited by the step 1.
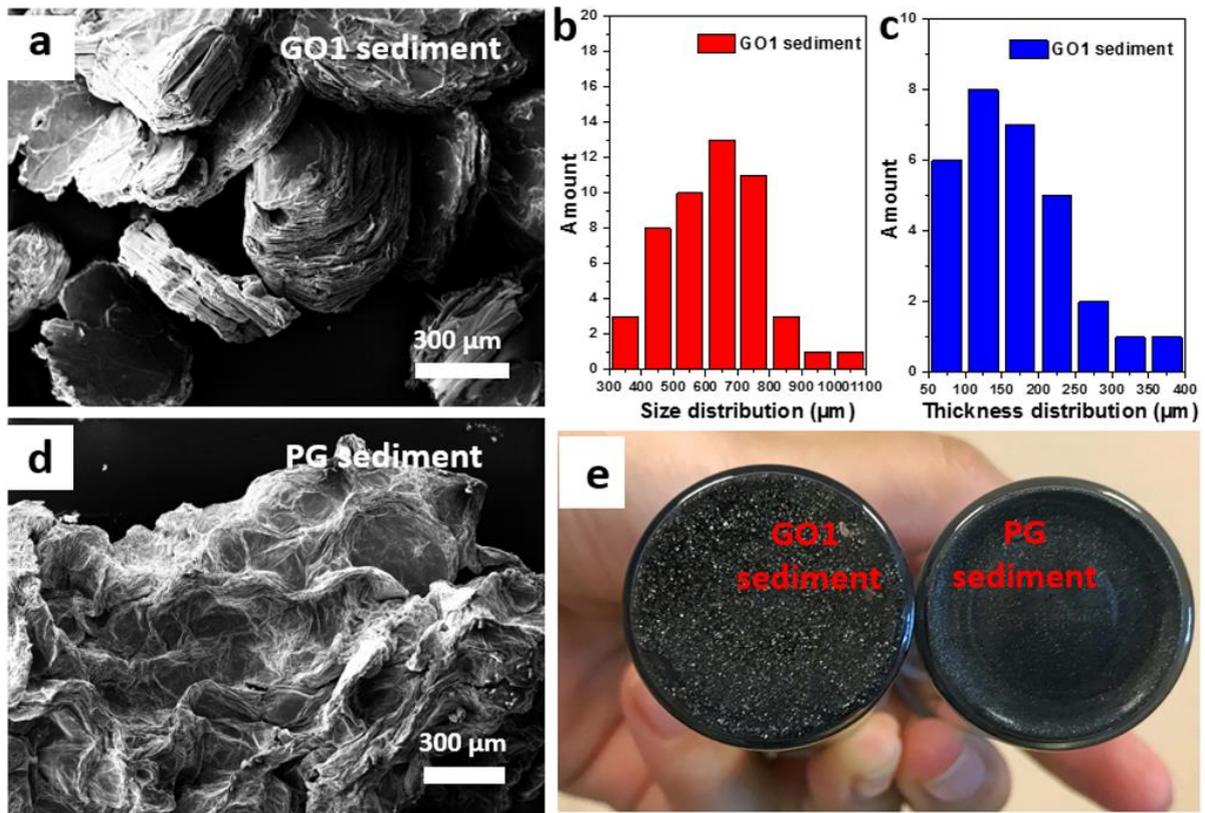
Figure 4.9 | SEM images of (a) GO1 sediment and (d) PG sediment. (b, c) The size and thickness distributions of GO1 sediment. (e) Digital image of GO1 and PG sediment.

Literature widely reports that GO with a high oxidation degree can be well dispersed in water without assistance of stabilizers, [20–23] In the case of exfoliation of GO2 in PVA solutions, we have shown that GO2 content is not affected by the PVA concentration anymore. Based on the theory proposed in the last chapter, we have shown that polymer can stabilize 2D materials thanks to the adsorption energy parameter, δ_e, which corresponds to the Hansen Solubility Parameters (HSP) of each specimen. In fact, the biggest difference of HSP between PG and GO2 is hydrogen bonding δ_h contribution. Table 4.2 listed HSP of GO2, PVA and water. Comparing with $\delta_h = 7.7$ of PG, δ_h of GO2 becomes 15.7.

Table 4.2 The Hansen solubility parameters of GO2, PVA and water. [5,24–26]

	δ_d	δ_p	δ_h
GO2	17.1	10.0	15.7
PVA	17.0	9.0	18.0
Water	15.5	16.0	42.3

$\delta_e = \chi_s - \chi$ is reported in section 3.5 of the last chapter, according to two equations as following:

$$\chi = \frac{v_o}{kT}(\delta_p - \delta_s)^2 \tag{4.2}$$

$$\chi_s = \frac{v_o}{kT}\left[(\delta_s - \delta_g)^2 - (\delta_p - \delta_g)^2\right] \tag{4.3}$$

If using Hansen solubility parameters, the formula is converted to the form as:

$$\chi = \frac{v_o}{kT}\left[\left(\delta_{d,p} - \delta_{d,s}\right)^2 - 0.25\left(\delta_{p,p} - \delta_{p,s}\right)^2 - 0.25\left(\delta_{h,p} - \delta_{h,s}\right)^2\right] \tag{4.4}$$

χ_s is also expressed in the same way. All the terms of these equations are defined section 3.5. Then it is possible to determine $\delta_e = 0.2$ for GO2/PVA/water ternary system. This value expresses the fact that it is harder to exchange a water molecule in contact with the GO2 surface in water reference by a PVA monomer with equivalent size from the pure PVA reference phase. The reason is that the hydrogen bond contribution δ_h of GO2 makes both the interaction of GO2-water and GO2-PVA stronger. Unfortunately, the adsorption model of PG/PVA/water built in the last chapter is not applicable to GO2/PVA/water system, because one PVA chain could interact with two or more GO2 nanosheets at the same time by forming cross-linking sites through hydrogen bonds. [27] Figure 4.10 represents the schematic representation of the interaction between specimens of GO2/PVA/water solution with different PVA concentration. In Figure 4.10a, only GO2 nanosheets dispersed in water presented a sol-like state, which indicates that 4.5 mg/mL GO2 is not enough to produce a completely cross-linked network structure through the hydrogen bond between the GO nanosheets. When GO2 dispersed in the PVA/water solution with a lower PVA concentration (0.05-0.5 mg/mL), these PVA chains could connect with GO2 nanosheets by forming hydrogen bonds, resulting in the increase of the mixture's viscosity. However, limited PVA chains are not enough to form 3D networks with the nanosheets, shown in Figure 10b, thereby it is still a sol-like state. Once PVA concentration is higher than 1 mg/mL, the 3D networks starts to be built, the mixture transited from sol-like to gel-like state, shown in Figure 10c.

Figure 4.10 | Schematic diagram of the interaction between specimen of GO2/PVA/water solution in different situation: (**a**) GO2/water, (**b**) GO2/PVA/water in the state of sol-like, and (**c**) GO2/PVA/water in the state of gel-like.

4.4 Conclusion

In this chapter, two GO with different oxidation degree have been prepared by the modified Hummers' method. By liquid-phase exfoliation, PG, GO1 and GO2 have been exfoliated in PVA/water solutions. Results have shown that GO1 with a lower oxidation degree is more difficult to exfoliate in PVA/water solution than PG. Actually, GO1 displaying in flaky form has formed hydrogen bond between layers, which cannot be overcome by ultrasonic energy. On the contrary, GO2 with a higher oxidation degree not only decorated by a large number of oxygen-containing functional groups but also lost its flaky form, thus they can be exfoliated easily in water. Furthermore, GO2/PVA/water has a transition from sol-like to gel-like state with PVA concentration increasing. When PVA concentration is over than 1 mg/mL, the amount of PVA chains is enough to connect to all GO2 dispersed nanosheets via hydrogen bonds, making the GO2/PVA/water begin to show a gel-like state.

References

1. Rubinstein, M. & Colby, R. H. *Polymer physics*. (Oxford Univ. Press, 2010).

2. Hernandez, Y. *et al.* High-yield production of graphene by liquid-phase exfoliation of graphite. *Nature Nanotechnology* **3**, 563–568 (2008).

3. O'Shaughnessy, B. & Vavylonis, D. Irreversible adsorption from dilute polymer solutions. *The European Physical Journal E* **11**, 213–230 (2003).

4. May, P., Khan, U., Hughes, J. M. & Coleman, J. N. Role of Solubility Parameters in Understanding the Steric Stabilization of Exfoliated Two-Dimensional Nanosheets by Adsorbed Polymers. *The Journal of Physical Chemistry C* **116**, 11393–11400 (2012).

5. *Hansen solubility parameters: a user's handbook*. (CRC Press, 2007).

6. Morimoto, N., Kubo, T. & Nishina, Y. Tailoring the Oxygen Content of Graphite and Reduced Graphene Oxide for Specific Applications. *Scientific Reports* **6**, 21715 (2016).

7. Hanifah, M. F. R. *et al.* Facile synthesis of highly favorable graphene oxide: Effect of oxidation degree on the structural, morphological, thermal and electrochemical properties. *Materialia* **6**, 100344 (2019).

8. Reynosa-Martínez, A. C. *et al.* Effect of the degree of oxidation of graphene oxide on As (III) adsorption. *Journal of Hazardous Materials* **384**, 121440 (2019)

9. Chen, Y. *et al.* Microbial reduction of graphene oxide by Azotobacter chroococcum. *Chemical Physics Letters* **677**, 143–147 (2017).

10. Guerrero-Contreras, J. & Caballero-Briones, F. Graphene oxide powders with different oxidation degree, prepared by synthesis variations of the Hummers method. *Materials Chemistry and Physics* **153**, 209–220 (2015).

11. Krishnamoorthy, K., Veerapandian, M., Yun, K. & Kim, S.-J. The chemical and structural analysis of graphene oxide with different degrees of oxidation. *Carbon* **53**, 38–49 (2013).

12. Xia, M., Su, Z. & Zhang, S. Raman spectra of bilayer graphene covered with Poly(methyl methacrylate) thin film. *AIP Advances* **2**, 032122 (2012).

13. Muzyka, R., Drewniak, S., Pustelny, T., Chrubasik, M. & Gryglewicz, G. Characterization of Graphite Oxide and Reduced Graphene Oxide Obtained from Different Graphite Precursors and Oxidized by Different Methods Using Raman Spectroscopy. *Materials* **11**, 1050 (2018).

14. Al-Gaashani, R., Najjar, A., Zakaria, Y., Mansour, S. & Atieh, M. A. XPS and structural studies of high-quality graphene oxide and reduced graphene oxide prepared by different chemical oxidation methods. *Ceramics International* **45**, 14439–14448 (2019).

15. Oh, Y. J. *et al.* Oxygen functional groups and electrochemical capacitive behavior of incompletely reduced graphene oxides as a thin-film electrode of supercapacitor. *Electrochimica Acta* **116**, 118–128 (2014).

16. Mohrig, J. R. *et al.* Techniques in Organic Chemistry. (W.H. Freeman. Press, 2010)

17. Cano, M. *et al.* Improving the mechanical properties of graphene oxide-based materials by covalent attachment of polymer chains. *Carbon* **52**, 363–371 (2013).

18. Cooper, A. J., Wilson, N. R., Kinloch, I. A. & Dryfe, R. A. W. Single stage electrochemical exfoliation method for the production of few-layer graphene via intercalation of tetraalkylammonium cations. *Carbon* **66**, 340–350 (2014).

19. Stobinski, L. *et al.* Graphene oxide and reduced graphene oxide studied by the XRD, TEM and electron spectroscopy methods. *Journal of Electron Spectroscopy and Related Phenomena* **195**, 145–154 (2014).

20. Konios, D., Stylianakis, M. M., Stratakis, E. & Kymakis, E. Dispersion behaviour of graphene oxide and reduced graphene oxide. *Journal of Colloid and Interface Science* **430**, 108–112 (2014).

21. Xu, Y., Bai, H., Lu, G., Li, C. & Shi, G. Flexible Graphene Films via the Filtration of Water-Soluble Noncovalent Functionalized Graphene Sheets. *J. Am. Chem. Soc.* **130**, 5856–5857 (2008).

22. Chen, L., Xu, C., Liu, J., Fang, X. & Zhang, Z. Optical absorption property and photo-thermal conversion performance of graphene oxide/water nanofluids with excellent dispersion stability. *Solar Energy* **148**, 17–24 (2017).

23. Zhao, L. *et al.* Investigation of dispersion behavior of GO modified by different water reducing agents in cement pore solution. *Carbon* **127**, 255–269 (2018).

24. O'Neill, A., Khan, U., Nirmalraj, P. N., Boland, J. & Coleman, J. N. Graphene Dispersion and Exfoliation in Low Boiling Point Solvents. *The Journal of Physical Chemistry C* **115**, 5422–5428 (2011).

25. Park, S. *et al.* Colloidal Suspensions of Highly Reduced Graphene Oxide in a Wide Variety of Organic Solvents. *Nano Letters* **9**, 1593–1597 (2009).

26. Hosseinpour, A., Abdizadeh, H. & Golobostanfard, M. R. Weighing Acetonitrile Against Water as Dispersing Media for Fabrication of Graphene Oxide Films via Electrophoretic Deposition. *Procedia Materials Science* **11**, 480–485 (2015).

27. Bai, H., Li, C., Wang, X. & Shi, G. A pH-sensitive graphene oxide composite hydrogel. *Chemical Communications* **46**, 2376 (2010).

Chapter 5

Electrochemical properties of PVA/GO2 hybrid aerogel for electrochemical capacitor application

Graphene-based aerogels are expected to be good candidates for electrode materials used for Electrochemical capacitor (EC). [1] In this chapter, a series of PVA/GO2 hybrid aerogels will be fabricated by a freeze-drying process directly using PVA/GO2 dispersions displaying different content of PVA (prepared in chapter 4). Then FTIR, XRD, SEM will be used to characterize their structure. Their electrochemical performance will be revealed by Cyclic Voltammetry (CV), Galvanostatic Charge Discharge (GCD), and Electrochemical Impedance Spectroscopy (EIS).

5.1 Introduction

Nowadays, with the development of global economy, problems induced by the exhausted source of fossil fuels and the environmental pollution become more and more serious. In order to meet human needs for clean energy, the environmentally friendly energy storage devices are being developed progressively. [2,3] Electrochemical capacitors (EC) are good candidates to be coupled with batteries for applications in portable devices and electrical vehicles because of their high power density and long-term cycle life. [4,5] GO decorated with oxygen-containing functional groups has low conductivity, thus it is theoretically considered not suitable for directly serving as electroactive material in EC. [6] However, Yang et al. have proved that the presence of oxygen-containing functional groups can provide to GO additional surface faraday reactions. Actually, GO displays a specific capacitance up to 189 F g^{-1}, as well as a great rate performance and outstanding cycle durability compared to graphene.[7] On the other hand, GO with large surface area has been expected to enhance the charge storage through an electric double layer capacitance (EDLC) mechanism.

Although, as it was shown in the last chapter, GO presents a better dispersibility in solvent than graphene and allows to considerably avoid the stacking of layers during its processability, trend that can usually weaken its electrochemical performance. [8] Polymer can play a role of spacer to expand the interlayer distance between graphene-based nanosheets. For instance, PVA, which presents many hydroxyl functions can form interfacial hydrogen bonds with the oxygen-containing functional groups of GO, resulting in a better homogenization when processed as composite. [9] Moreover, PVA/ GO hybrid composites have been considered to possess excellent mechanical properties. [10–12]

In the last chapter, we found that GO2 in PVA aqueous solution displayed a good dispersibility, and a transition phenomenon of sol-like to gel-like with PVA concentration increasing has been observed because of the cross-link forming between molecules and nanosheets. These as-obtained PVA/GO2 dispersions will be directly processed into PVA/GO2 hybrid aerogels by freeze-drying technique. The preparation process of aerogels has been presented in chapter 2. Their electrochemical properties for EC application will be studied.

5.2 Characterizations of PVA/GO2 hybrid aerogels

5.2.1 FT-IR

Figure 5.1 shows FT-IR spectra recorded on all PVA/GO2 hybrid aerogels samples as well on pure PVA.
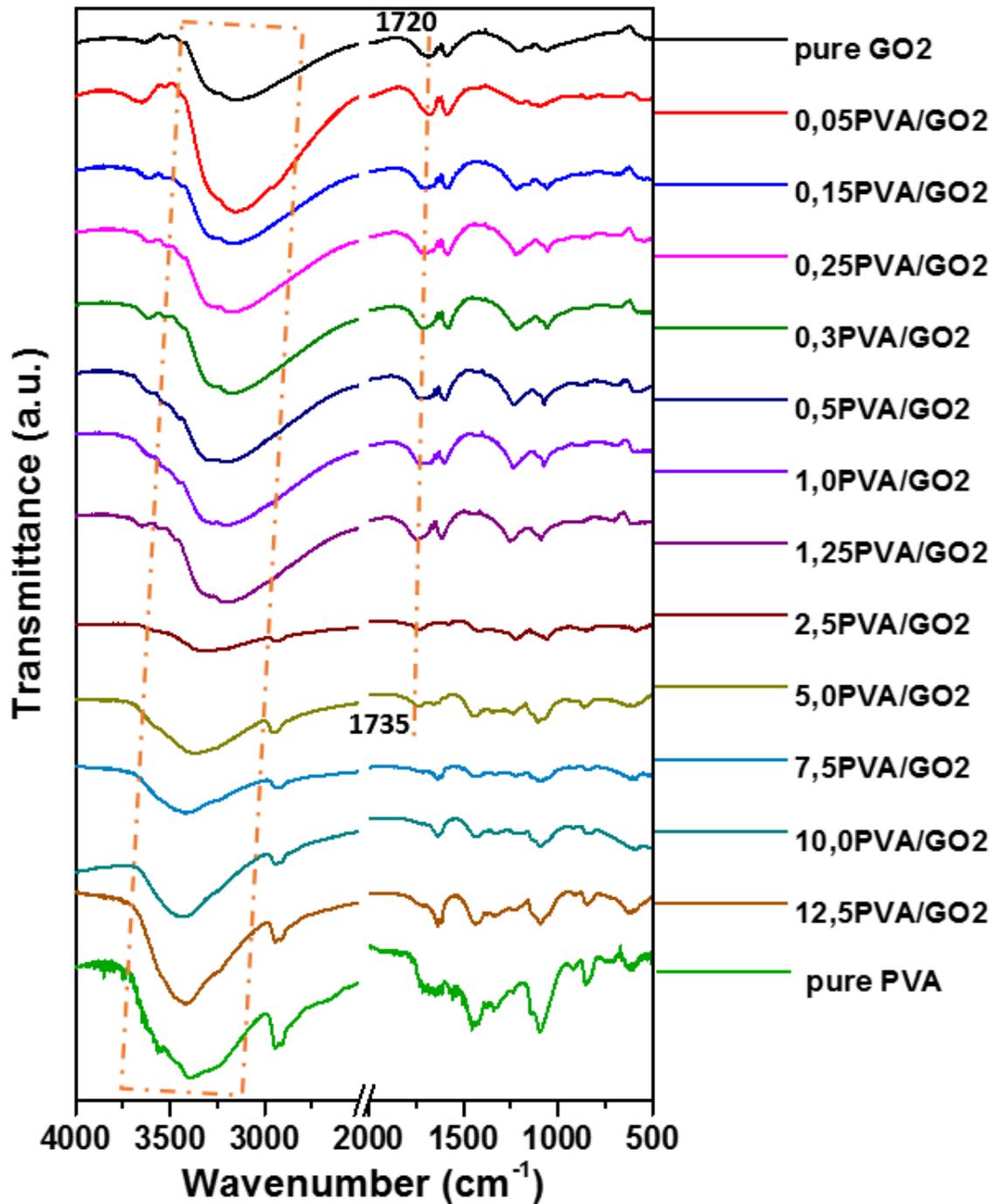
Figure 5.1| FT-IR spectra of PVA/GO2 hybrid aerogels with different content of PVA.

The broad and strong peak at ~3200 cm^{-1} belongs to O-H stretching vibration of carboxylic acid and absorbed water. [13,14] Vibrational bands at 1720 cm^{-1}, 1570cm^{-1}, 1210 cm^{-1} and 1045 cm^{-1} are attributed to C=O stretching mode of carboxyl/carbonyl, C=C skeletal stretching mode in graphite domains, C-O-C and C-OH stretching mode, respectively. [14–17] In pure PVA sample, the stretching vibration of -OH is characterized as a broad and strong absorption at 3000-3700

114

cm^{-1} due to the intermolecular and intramolecular hydrogen bonding. [18] The absorption peak at ~2920 cm^{-1} is attributed to the C-H stretching mode vibrations [19] Another two peaks at ~1465 cm^{-1} and ~1087 cm^{-1} represent -CH$_2$- bending and C-O stretching vibrations in PVA. [20–22]

Increasing the amount of PVA within the sample from beginning to 5.0PVA/GO2 leads to a shift of the C=O vibration band of GO2 from 1720 cm^{-1} to 1735 cm^{-1}, meaning that the presence of PVA causes a breakage of the intramolecular hydrogen bonds between GO2 nanosheets. [23] Over than 5.0PVA/GO2, the samples mainly exhibit the characteristic peaks of PVA, the peak of the C=O vibration band of GO2 almost disappears. As a rule of thumb, the O-H stretching vibration is sensitive to hydrogen bonding. As observed in Figure 5.1, the O-H stretching peak is overall shifted to a higher wavenumber when the PVA content increases within the sample, which furthermore indicates that the incorporation of PVA inhibits the hydrogen bond between GO2 nanosheets, as well as GO2 nanosheets break the hydrogen bonds between the hydroxyl groups of PVA molecules. The hydroxyl groups from PVA chains reform hydrogen bonds with oxygen-containing functional groups on the GO2 nanosheets. [13,18] With the increasing amount of PVA, the interaction between PVA and GO2 is enhanced, which is helpful for building 3D networks and enhancing external force in aerogels.

5.2.2 XRD

The phase structure of PVA/GO2 aerogels with different PVA content and pure PVA powder are analyzed through XRD. Patterns are shown in Figure 5.2.
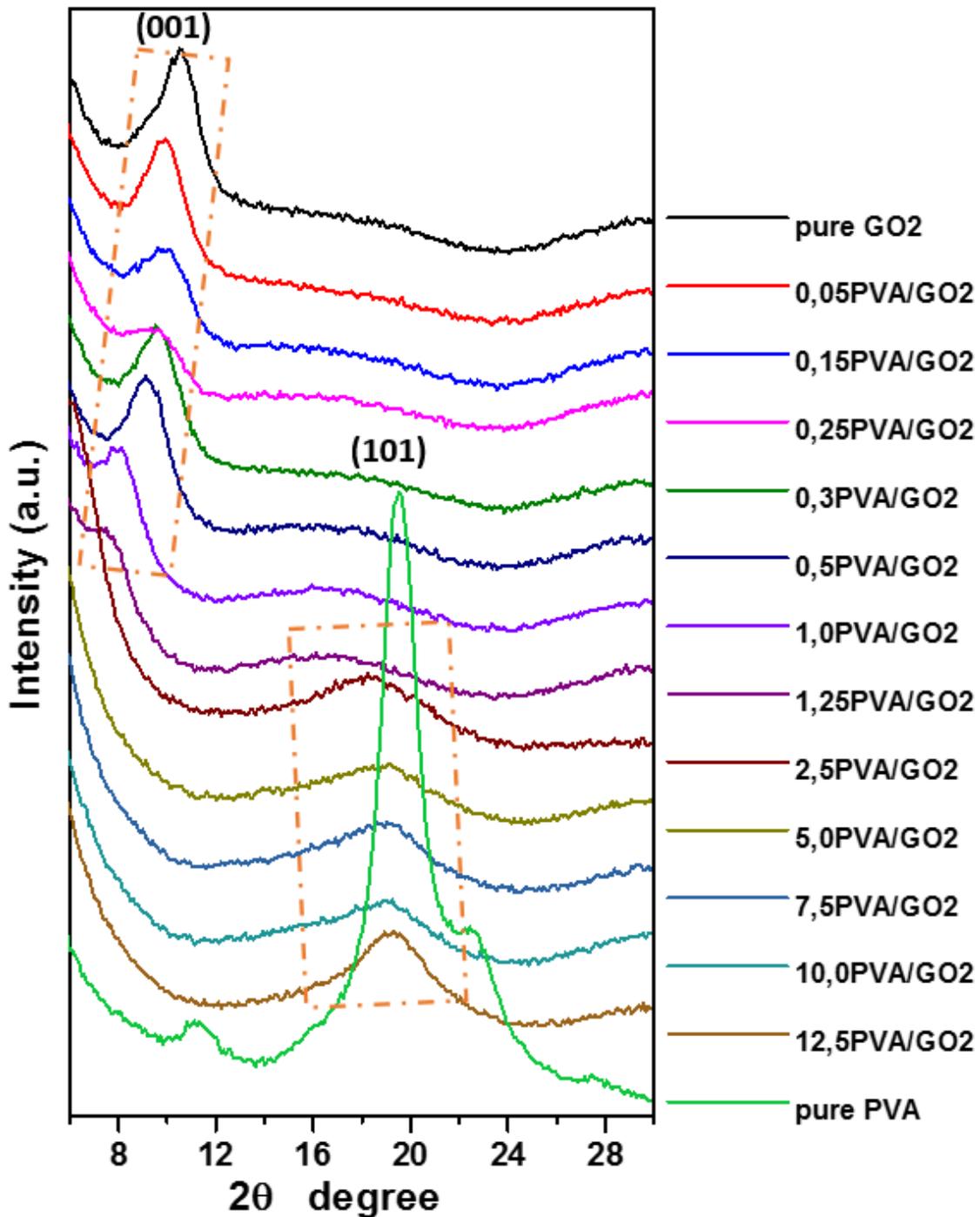
Figure 5.2 | XRD pattern of PVA/GO2 aerogels with different content of PVA.

Pure GO2 aerogel displays a diffraction peak at $2\theta = 10.5°$ identified as the (001) crystal planes with an interlayer spacing of 0.842 nm.[24] With the gradual increase in PVA within PVA/GO2 composites, the (001) diffraction peak is shifted to lower 2θ value until $2\theta = 7.5°$ for 1.25PVA/GO2. The corresponding interlayer spacing value increases from 0.842 nm to 1.177 nm. (all data are proposed in Table 5.1)

Table 5.1 XRD analysis of PVA/GO2 aerogels

Samples	(001) crystal face of GO2		(101) crystal face of PVA	
	2θ (°)	d-spacing (nm)	2θ (°)	d-spacing (nm)
Pure GO2	10.5	0.842	-	-
0.05PVA/GO2	9.8	0.901	-	-
0.15PVA/GO2	9.7	0.908	-	-
0.25PVA/GO2	9.6	0.919	-	-
0.30PVA/GO2	9.5	0.927	-	-
0.50PVA/GO2	9.0	0.973	-	-
1.0PVA/GO2	8.0	1.100	-	-
1.25PVA/GO2	7.5	1.177	-	-
2.5PVA/GO2	-	-	18.2	0.486
5.0PVA/GO2	-	-	18.9	0.469
7.5PVA/GO2	-	-	18.9	0.469
10.0PVA/GO2	-	-	19.0	0.467
12.5PVA/GO2	-	-	19.2	0.461
Pure PVA	-	-	19.5	0.454

This feature indicates the PVA polymer chains can successfully be intercalated between GO nanosheets, promoting the GO dispersion at a molecular level after freeze drying. With the further increase in PVA content, the interlayer spacing is further increased. Actually, the (001) diffraction peak is no longer visible , suggesting the absence of direct GO-GO packing mode in the hybrid aerogels due to the wrapping of nanosheets with PVA polymer chains. [25,26] On the opposite, the characteristic peak at $2\theta = 18.2°$ (d-spacing = 0.486 nm) of (101) crystal planes of the semi-crystalline PVA starts to appear in 2.5PVA/GO2 sample.[13] Furthermore, with the increase in PVA content, this peak is shifted to a higher value closing to that expected for pure PVA. The corresponding interlayer spacing value being decreasing from 0.486 nm for 2.5PVA/GO2 to 0.461 nm of 12.5PVA/GO2, reveals a stronger interaction among PVA macromolecules.

5.2.3 SEM

SEM images in Figure 5.3 show the morphology of PVA/GO2 hybrid aerogels with different PVA content.
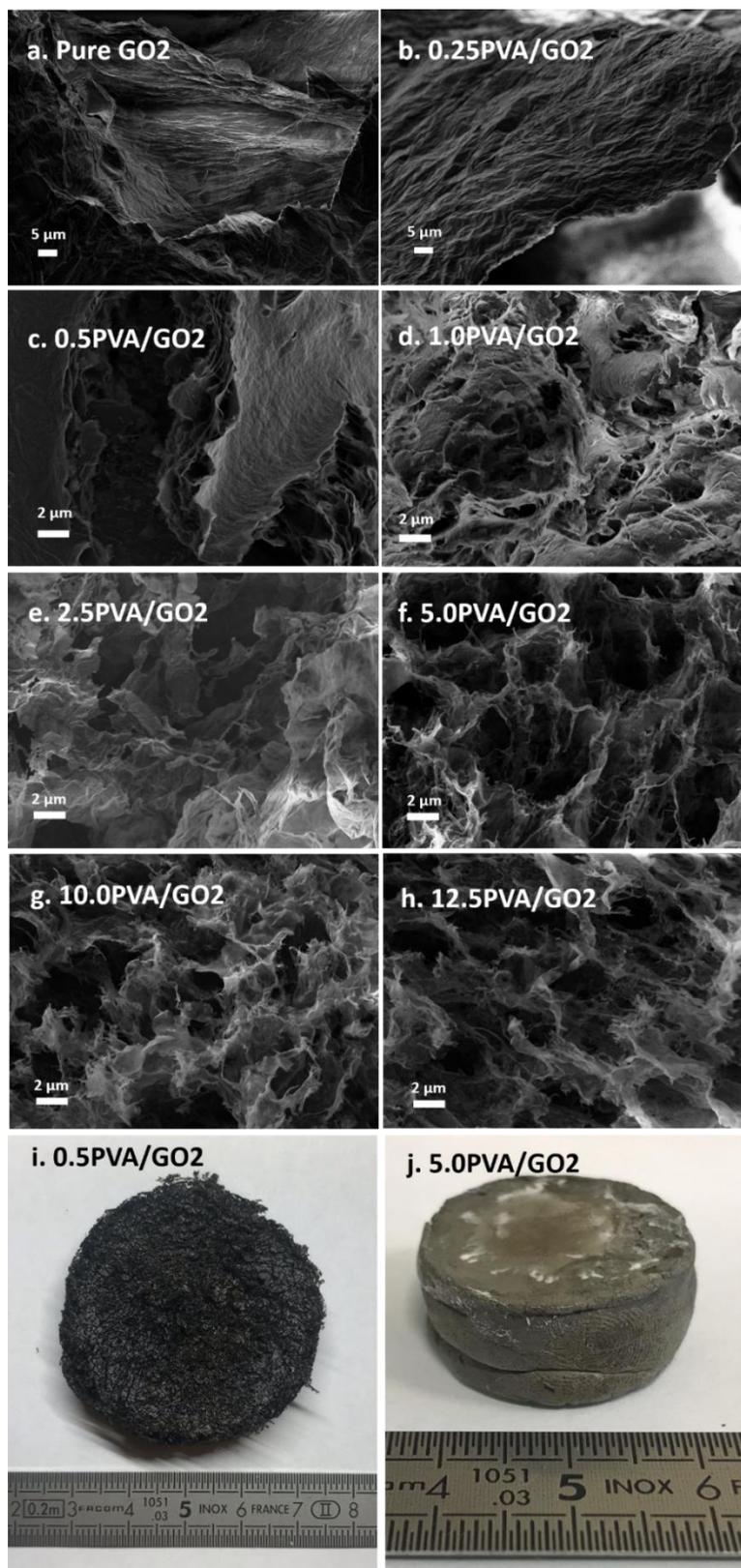
Figure 5.3 | SEM images of PVA/GO2 hybrid aerogels with different content of PVA. (a) pure GO2, (b) 0.25PVA/GO2, (c) 0.5PVA/GO2, (d) 1.0PVA/GO2, (e) 2.5PVA/GO2, (f) 5.0PVA/GO2, (g) 10.0PVA/GO2 and (h) 12.5PVA/GO2. Digital photos of two examples of (i) 0.5PVA/GO2 and (j) 5.0PVA/GO2

118

In Figure 5.3a, the pure GO2 aerogel displays the GO sheets stacked together without any expansion of layers. When a very small PVA incorporated into GO, the interlayer spacing is supposed to be larger, which was proven by XRD characterization. However, in SEM images of Figure 5.3b, this intercalation cannot be observed, the morphology of 0.25PVA/GO2 sample looks like that of pure GO2. This could be ascribed to that too small interlayer expansion cannot be displayed in SEM images. When PVA content increases to 0.5 mg/mL, in Figure 5.3c, it tends to show the expanded state of the nanosheets. Then, with the continuous increase in PVA content, the PVA/GO2 hybrid aerogels exhibit an interconnected 3D network with more PVA covering the nanosheets. (Figure 5.3 d-h) Figure i and j represent two digital photos of samples 0.5 PVA/GO2 and 5 PVA/GO2. Shaped with a small amount of PVA, aerogel maintains the characteristics of that prepared with GO, while by incorporating a large amount of PVA, aerogel shows the characteristics like those of the polymer.

To conclude on the characterization of this series of samples, FT-IR, XRD and SEM results provide a reliable explanation to prove the existence of hydrogen bonds between GO-GO, PVA-PVA, and GO-PVA. Samples containing a high content of PVA display a 3D network structure. Therefore, PVA polymer chains play a role of spacer in samples prepared with low PVA content, and a cross-linking intermediate in the samples synthesized with a higher PVA content.

5.3 Electrochemical performance

Since graphene-based aerogels are expected to be good candidates for electrode materials used in EC,[1] the electrochemical performance of the PVA/GO2 hybrid aerogels have been measured to confirm their interest in this application field. Figure 5.4 compares Cyclic Voltammetry (CV) curves recorded on all the sample with a scan rate of 50 mV s^{-1} with a potential window of -0.8-0.0V (vs. Ag/Ag/Cl). In general, a larger integrated CV area indicates a faster current response on potential reversal, thus demonstrating the faster carriers' transfer speed and the better electrochemical performances. In Figure 5.4a, the hybrid aerogels containing a small PVA content (0.05, 0.15, 0.25, 0.3, 0.5) display bigger loop areas compared with pure GO2, indicating a high specific capacitance. However, 1.0PVA/GO2 and 1.25PVA/GO2 show the area close to pure GO2, demonstrating that more PVA addition weakens their specific capacitance. On the second graph (Figure 5.4b) the area of the samples containing higher PVA contents (2.5, 5.0, 7.5, 10.0, 12.5) dramatically decrease, indicating a low specific capacitance.

In order to minimize experimental errors, measurements have been reproduced 5 times on each sample. They exhibit a variation of CV curves comparable to Figure 4a and b.
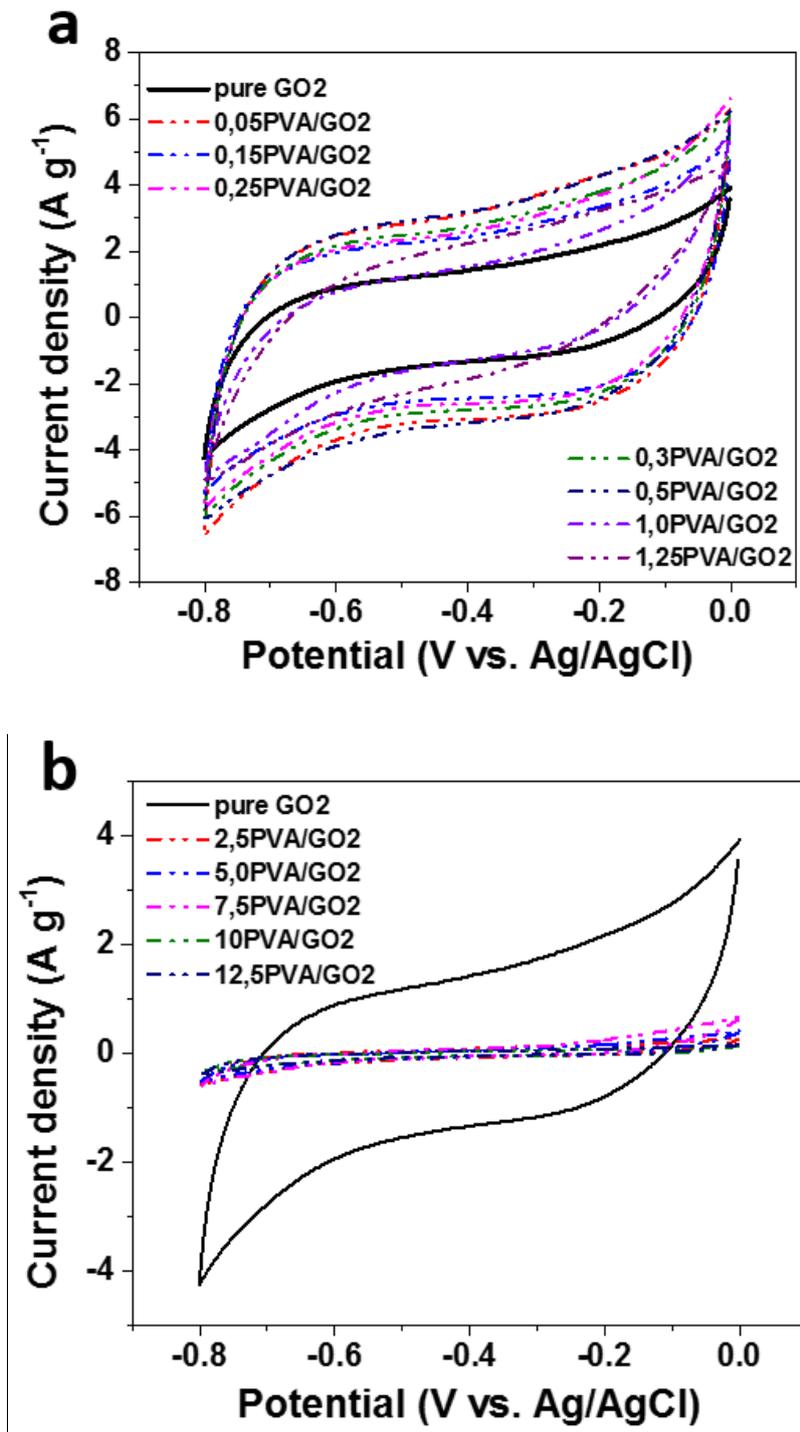
Figure 5.4 | CV curves of samples at scan rate of 50 mV s^{-1}: (a) pure GO2, 0.05PVA/GO2, 0.15PVA/GO2, 0.25PVA/GO2, 0.3PVA/GO2, 0.5PVA/GO2, 1.0PVA/GO2, and 1.25PVA/GO2, (b) pure GO2, 2.5PVA/GO2, 5.0PVA/GO2, 7.5PVA/GO2, 10.0PVA/GO2, and 12.5PVA/GO2

Moreover, the CV curves exhibit rectangular shape, illustrating typical of double layer charging. However, their shapes with distortion could be attributed to the following factors: *i)* Equivalent Series Resistance (ESR) for the real capacitors, and *ii)* the surface faradaic reactions due to the existence of abundant oxygen functional groups on GO2, shown in Scheme 1. [24, 27 ,35, 36]
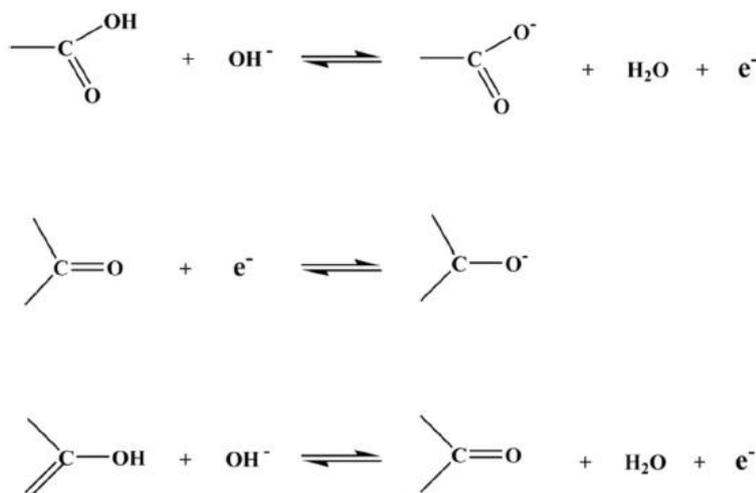
Scheme 1 | The proposed surface faradic redox reaction on the aerogels

Figure 5.5 displays the galvanostatic charge-discharge (GCD) measurements recorded on all hybrid aerogels in the potential window of -0.8-0.0 V (vs. Ag/Ag/Cl) at a current density of 1 A g^{-1}.
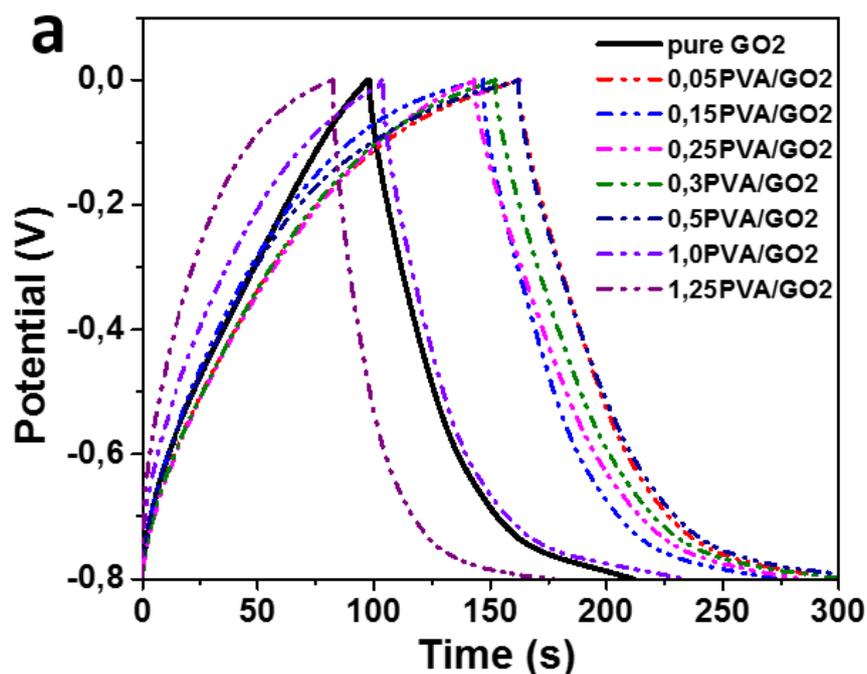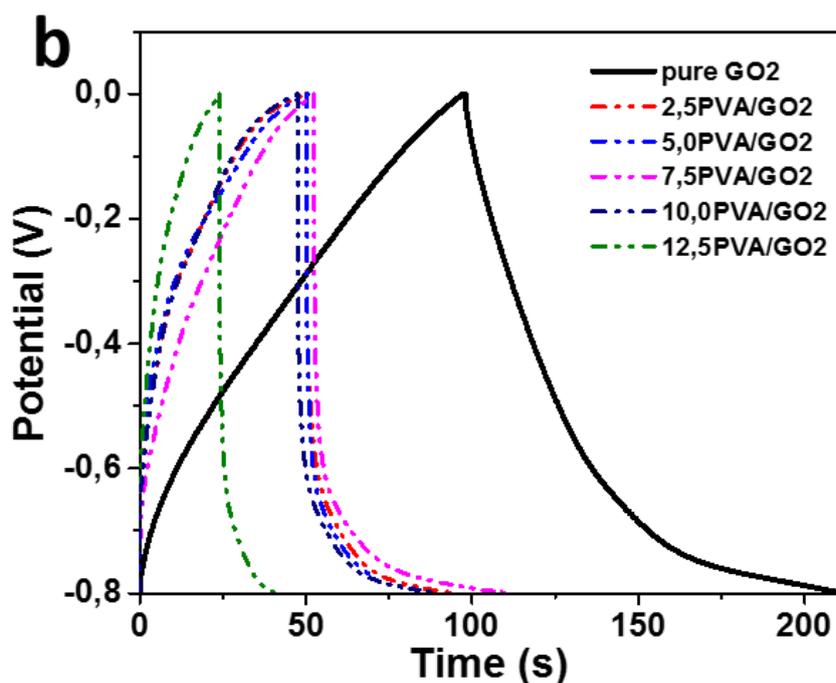
Figure 5.5 | The GCD behavior of electroactive materials at the same current density of 1 A g^{-1}. (a) pure GO2, 0.05PVA/GO2, 0.15PVA/GO2, 0.25PVA/GO2, 0.3PVA/GO2, 0.5PVA/GO2, 1.0PVA/GO2, and 1.25PVA/GO2, (b) pure GO2, 2.5PVA/GO2, 5.0PVA/GO2, 7.5PVA/GO2, 10.0PVA/GO2, and 12.5PVA/GO2.

The non-symmetric triangular shape is the sign of irreversible faradaic reactions (such as hydrogen evolution reaction). [28] As expected, incorporating a small PVA content (0.05, 0.15, 0.25, 0.3, 0.5 mg/mL) within GO makes discharging and charging time longer than that of pure GO2 sample. (see Figure 5.5a) However, 1.0PVA/GO2 and 1.25PVA/GO2 show that their discharging and charging time begins to close or be less than that of pure GO2 sample. When PVA content is increasing (2.5, 5.0, 7.5, 10.0, 12.5), Figure 5.5b, the discharging and charging time of the hybrid aerogels become shorter than for pure GO2 sample.

The specific capacitances (*C*, F g^{-1}) of working electrode can be calculated from galvanostatic discharge curves according to:

$$C = \frac{I \times \Delta t}{m \times \Delta V} \tag{5.1}$$

Where *I* (A) is the discharge current, *Δt* (s) is the discharge time, *m* (g) is the mass of electroactive materials on single electrode, and *ΔV* (V) is the total potential change. Figure 5.6 presents the averagely calculated specific capacitance of PVA/GO2 hybrid aerogels electrodes

as function of PVA content. 5 GCD measurements at a current density of 1 A g^{-1} for each sample have been carried out.
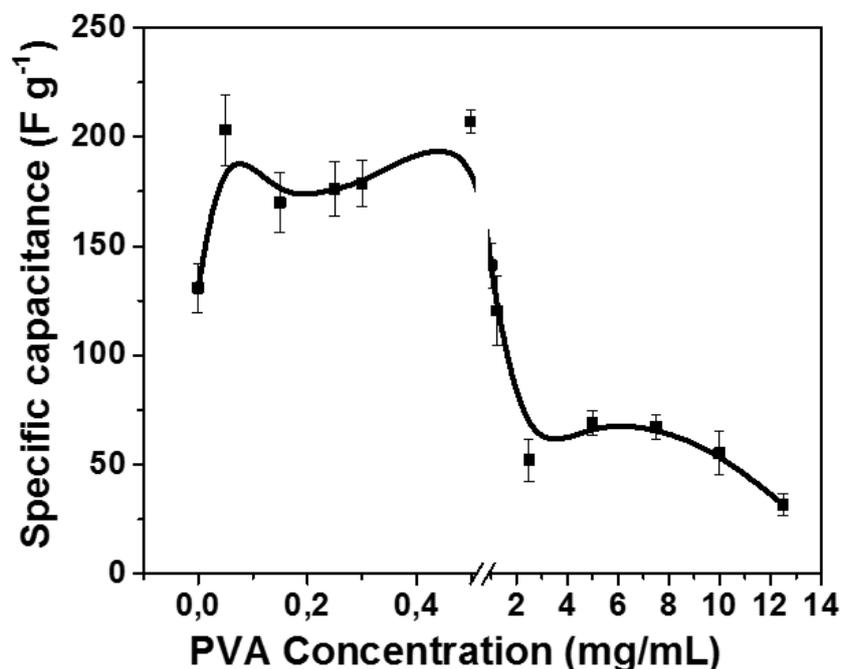
Figure 5.6 | The calculated specific capacitance of PVA/GO2 hybrid aerogels electrodes as function of PVA content.

Pure GO2 sample presents a specific capacitance of 131 ($\pm$11) F g^{-1}. With a small PVA's assistance, 0.05, 0.15, 0.25, 0.3, 0.5 mg/mL, the specific capacitance increases to 203 ($\pm$16), 170 ($\pm$14), 176 ($\pm$13), 179 ($\pm$10), 207 ($\pm$5) F g^{-1}, respectively. When PVA content is 1.0 and 1.25 mg/mL within samples, the specific capacitance is getting closer to that of pure GO2 sample, becoming 141 ($\pm$10) and 120 ($\pm$15) F g^{-1}. As soon as PVA content is over than 1.25 mg/mL in the hybrid material, its specific capacitance dramatically decreases lower than that of pure GO2 samples.

In order to better understand the rate performance of PVA/GO2 hybrid aerogels, the electrochemical impedance spectroscopy (EIS) is used to investigate the kinetic characteristic of the ions transport in electrodes.

Figure 5.7 | Impedance Nyquist plots of the pure GO2 aerogel and the PVA/GO2 hybrid aerogels containing a small PVA content of 0.05, 0.15, 0.25, 0.3, and 0.5 mg/mL

A Nyquist plot is a parametric plot of a frequency response used in automatic control and signal processing. The frequency is swept as a parameter, resulting in a plot per frequency. In our case, the Nyquist plots based on a frequency response from 100KHz to 0.1 Hz which is 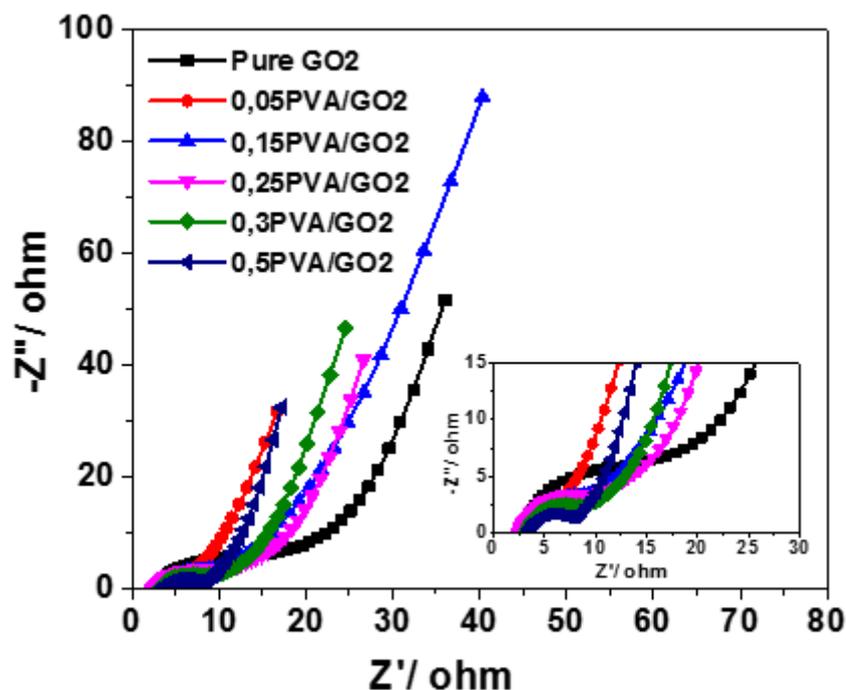recorded in Figure 5.7 are from right to left. All samples exhibit light arcs in the high frequency range and straight lines in the low frequency range. At high frequency range, the semicircle's diameter is related to the charge transfer resistance. [29,30] The hybrid aerogels with low PVA content exhibit smaller semicircle diameters than this measured on pure GO2 sample, indicating a lower ionic and electron charge transfer resistance at the electrolyte/ electrode interface. [31] The low quantity of PVA intercalated in GO nanosheets induces an increase in the distance between layers, facilitating the efficient transport of electrolyte ions within GO nanosheets surface and shorten the path of ions diffusion across. [32] At low frequency range, the straight lines of PVA/GO2 electrode are overall steeper than that of pure GO2 sample, implying faster ion migration and closer ideal capacitors' behaviors. [33,34]

The capacitive enhancement enabled by PVA can be attributed to a spacer effect. According to the structure characterizations of FTIR and XRD, the distance in GO layers gradually enlarges with increase in PVA content thanks to hydrogen bonds which interconnect GO nanosheets and

PVA molecules. Such PVA/GO2 hybrid aerogels provide bigger inner surface area for the transport and adsorption of electrolyte ions, and expose more oxygen-containing functional groups, which could result in a great contribution of EDLC and the capacitance from faradic reactions. Nevertheless, though excess amount of PVA presence can cause porous structure with obvious 3D network cross-link as shown in SEM images proposed in Figure 5.3, a large number of PVA molecules present on the GO surface weakens the contribution from GO's surface faradaic reactions, resulting in a lower capacitance. On the other hand, excess amount of PVA induces larger resistance, decreasing electron conductivity. [31]

5.4 Conclusion

A series of PVA/GO2 hybrid aerogels with different PVA contents have been prepared by a freeze-drying process. PVA can intercalate between GO layers by forming hydrogen bonds to expand the distance between the layers, even forming an interconnected 3D network when PVA content increases a lot. Using these samples as electroactive materials for electrochemical capacitor, we can prove that hybrid aerogels containing low PVA content, from 0.05 to 0.5 mg/mL, exhibit an electrochemical performance improvement compared to pure GO2 sample. The reason is that low amount of PVA induces a spacer effect on hybrid aerogels, facilitating the transport and the adsorption of electrolyte ions, and exposes more oxygen-containing functional groups. Furthermore, it improves the contribution of both EDLC and capacitance from surface faradic reactions. However, by introducing an excess amount of PVA, meaning over 1.25 mg/mL, electrochemical performances start to decrease. Actually, samples exhibit unsatisfactory performance because active oxygen functional groups are covered by PVA molecules inducing a larger resistance.

References

1. Ye, S., Feng, J. & Wu, P. Deposition of Three-Dimensional Graphene Aerogel on Nickel Foam as a Binder-Free Supercapacitor Electrode. ACS Applied Materials & Interfaces 5, 7122–7129 (2013).

2. Zhong, W. W., et al. New Prelithiated V2O5 Superstructure for Lithium-Ion Batteries with Long Cycle Life and High Power. ACS Energy Letters 5, 31-38 (2020)

3. Meng, L. et al. Simultaneous Manipulation of O-Doping and Metal Vacancy in Atomically Thin Zn10In16S34 Nanosheet Arrays toward Improved Photoelectrochemical Performance. Angewandte Chemie International Edition 57, 16882–16887 (2018).

4. Wu, Z. Y., et al. Novel Sub‐5 nm Layered Niobium Phosphate Nanosheets for High‐Voltage, Cation‐Intercalation Typed Electrochemical Energy Storage in Wearable Pseudocapacitors. Advanced Energy Materials 9, 1900111 (2019)

5. Pan, Z. et al. In Situ Growth of Layered Bimetallic ZnCo Hydroxide Nanosheets for High-Performance All-Solid-State Pseudocapacitor. ACS Nano 12, 2968–2979 (2018).

6. Wang, Y. et al. Supercapacitor Devices Based on Graphene Materials. J. Phys. Chem. C 113, 13103–13107 (2009).

7. Xu, B. et al. What is the choice for supercapacitors: graphene or graphene oxide? Energy & Environmental Science 4, 2826 (2011).

8. Zhang, X. & Samorì, P. Graphene/Polymer Nanocomposites for Supercapacitors. ChemNanoMat 3, 362–372 (2017).

9. Pawar, P. B., Shukla, S. & Saxena, S. Graphene oxide – Polyvinyl alcohol nanocomposite-based electrode material for supercapacitors. Journal of Power Sources 321, 102–105 (2016).

10. Liang, J. et al. Molecular-Level Dispersion of Graphene into Poly (vinyl alcohol) and Effective Reinforcement of their Nanocomposites. Advanced Functional Materials 19, 2297–2302 (2009).

11. Zhang, L. et al. High strength graphene oxide/polyvinyl alcohol composite hydrogels. Journal of Materials Chemistry 21, 10399 (2011).

12. Xu, Y., Hong, W., Bai, H., Li, C. & Shi, G. Strong and ductile poly (vinyl alcohol)/graphene oxide composite films with a layered structure. Carbon 47, 3538–3543 (2009).

13. Shi, Y., Xiong, D., Li, J. & Wang, N. The water-locking and cross-linking effects of graphene oxide on the load-bearing capacity of poly (vinyl alcohol) hydrogel. RSC Advances 6, 82467–82477 (2016).

14. Hanifah, M. F. R. et al. Facile synthesis of highly favorable graphene oxide: Effect of oxidation degree on the structural, morphological, thermal and electrochemical properties. Materialia 6, 100344 (2019).

15. Reynosa-Martínez, A. C. et al. Effect of the degree of oxidation of graphene oxide on As (III) adsorption. Journal of Hazardous Materials 384 121440 (2019)

16. Krishnamoorthy, K., Veerapandian, M., Yun, K. & Kim, S.-J. The chemical and structural analysis of graphene oxide with different degrees of oxidation. Carbon 53, 38–49 (2013).

17. Cano, M. et al. Improving the mechanical properties of graphene oxide-based materials by covalent attachment of polymer chains. Carbon 52, 363–371 (2013).

18. Qi, X., Yao, X., Deng, S., Zhou, T. & Fu, Q. Water-induced shape memory effect of graphene oxide reinforced polyvinyl alcohol nanocomposites. J. Mater. Chem. A 2, 2240–2249 (2014).

19. Snyder, R. G., Hsu, S. L. & Krimm, S. Vibrational spectra in the C-H stretching region and the structure of the polymethylene chain. Spectrochimica Acta Part A: Molecular Spectroscopy 34, 395–406 (1978).

20. Snyder, R. G., Hsut, S. L. & Krimm, S. Vibrational spectp in the C-H stretching region and the structure of the polymethylene chain. Spectrochimica Acta 12, (395-406) 1978

21. Prosanov, I. Yu. & Matvienko, A. A. Study of PVA thermal destruction by means of IR and Raman spectroscopy. Phys. Solid State 52, 2203–2206 (2010).

22. Kharazmi, A. et al. Structural, optical, opto-thermal and thermal properties of ZnS–PVA nanofluids synthesized through a radiolytic approach. Beilstein Journal of Nanotechnology 6, 529–536 (2015).

23. Lecaros, R. L. G. et al. Tunable interlayer spacing of composite graphene oxide-framework membrane for acetic acid dehydration. Carbon 123, 660–667 (2017).

24. Wei, N. et al. Superelastic active graphene aerogels dried in natural environment for sensitive supercapacitor-type stress sensor. Electrochimica Acta 283, 1390–1400 (2018).

25. Huang, J., Li, Z., Wu, X., Wang, J. & Yang, S. Poly (vinyl alcohol)-Mediated Graphene Aerogels with Tailorable Architectures and Advanced Properties for Anisotropic Sensing. The Journal of Physical Chemistry C 123, 3781–3789 (2019).

26. Bai, H., Li, C., Wang, X. & Shi, G. A pH-sensitive graphene oxide composite hydrogel. Chemical Communications 46, 2376 (2010).

27. Zhang, Y., Fan, S., Li, S., Song, Y. & Wen, G. 3D porous oxygen-enriched graphene hydrogels with well-balanced volumetric and gravimetric performance for symmetric supercapacitors. Journal of Materials Science 55, 12214–12231 (2020).

28. Lai, L. et al. Tuning graphene surface chemistry to prepare graphene/polypyrrole supercapacitors with improved performance. Nano Energy 1, 723–731 (2012).

29. Zhong, W. et al. Improved oxygen evolution activity of IrO 2 by in situ engineering of an ultra-small Ir sphere shell utilizing a pulsed laser. Nanoscale 11, 4407–4413 (2019).

30. Jiang, Y. C. et al. Charge Transfer in Ultrafine LDH Nanosheets/Graphene Interface with Superior Capacitive Energy Storage Performance. ACS Applied Materials & Interfaces 9, 37645-37654 (2017).

31. Chen, S. et al. Conductive, tough, hydrophilic poly (vinyl alcohol)/graphene hybrid fibers for wearable supercapacitors. Journal of Power Sources 319, 271–280 (2016).

32. Wu, Z. S. et al. Three-Dimensional Graphene-Based Macro- and Mesoporous Frameworks for High-Performance Electrochemical Capacitive Energy Storage. Journal of the American Chemical Society.134, 19532-19535 (2012)

33. Wang, H. et al. Three-dimensional macroporous graphene architectures as high-performance electrodes for capacitive deionization. J. Mater. Chem. A 1, 11778–11789 (2013).

34. Zeng, W. et al. Gas bubble templated synthesis of Mn3O4-embedded hollow carbon nanospheres in ethanol flame for elastic supercapacitor. Journal of Alloys and Compounds 731, 210–221 (2018).

35 Béguin, F., et al. "State of hydrogen electrochemically stored using nanoporous carbons as negative electrode materials in an aqueous medium." Carbon 44, 2392-2398 (2006)

36 Bleda-Martínez M J, Pérez J M, Linares-Solano A, et al. Effect of surface chemistry on electrochemical storage of hydrogen in porous carbon materials. *Carbon*, **46** (7), 1053-1059 (2008)

General conclusion and prospects

In this thesis, our objective was to prepare a high-concentration graphene aqueous dispersion incorporating a polymer by liquid-phase exfoliation technique, to be used as a starting material to fabricate composites applied in energetic storage fields. To date, it is still a challenge to disperse graphene in water because of its hydrophobic behavior. Strategies, like the use of a polymer as stabilizer or the introduction of oxygen-based groups within graphene, have been proven to be effective to increase the nanosheets' concentration and their dispersible stabilization in aqueous media.

Polymer can assist the pristine graphene dispersion in water. Developing a stable high concentration graphene dispersion with a minimal amount of polymer stabilizer needs considerable efforts to maximally preserve graphene properties. In chapter 3, we have demonstrated that pristine graphene dispersion in water could be obtained by using different PVA concentrations. Two maximum graphene contents at C_c and C^* in PVA solution have been observed. Especially at C_c, the ratio of graphene in polymer can reach up to 47 wt.% when left 24 h in a sonication bath and 85 wt.% if the duration is extended to one week. Based on Flory theory we have proposed a model to describe the process of polymer coils adsorption onto the graphene surface in a "dilute" regime of polymer solution. From this model, an equation has been developed to calculate the free energy variation brought by this process. This provides powerful tools to design graphene dispersion at the molecular level into polymer matrixes by noncovalent physisorption.

Graphite oxidation followed by LPE was the second considered route to allow the dispersion of large quantities of GO nanosheets in water. GO is typically defective, tailoring the oxygen content within graphene nanosheets is a way to optimize its properties and dispersibility. In chapter 4, we have found that a low oxidation degree treatment (GO1) would make GO more difficult to exfoliate than pristine graphite during the LPE process. This was attributed to the fact that hydrogen bonds occurring between the layers can be hardly overcame by ultrasonic energy. On the other hand, GO with a higher oxidation degree (GO2) can be exfoliated easily in water. Hence, it was possible to disperse 4.5 mg/mL of GO2 nanosheets in a PVA/water solution after 30 min sonication by using a tip. A deeper oxidation makes GO to lose its flaky form and to become hydrophilic. In solution, the hydroxyl groups from PVA chains can form hydrogen bonds with oxygen-containing functional groups on GO2 nanosheets, with PVA

concentration increasing, more PVA chains connect with GO2 nanosheets to build a 3D network. Therefore, there is a transition from sol-like to gel-like state, which happens when the PVA concentration is over than 1 mg/mL.

GO has been proved very useful in applications as composites. In chapter 5, we have directly used GO2/PVA/water mixtures obtained in chapter 4 to process a series of hybrid aerogels containing different PVA contents by a freeze-drying way, and as-obtained samples have been applied in electrode materials of electrochemical capacitors. Characterizations by means of FT-IR, XRD, and SEM recorded on the hybrid aerogels indicate that hydrogen bonds exist between GO-GO nanosheets, PVA-PVA chains, and GO nanosheet-PVA chain. PVA polymer chains play a role of spacer in the samples containing low PVA concentrations and can be considered as an intermediate to cross-link the nanosheets and chains forming a 3D network structure in samples containing high PVA concentrations. Furthermore, CV and GCD have been employed to explore hybrid aerogels' electrochemical performances. Results have shown that hybrid GO2/PVA aerogels containing a low PVA content, from 0.05 to 0.5 mg/mL, exhibit an electrochemical performance improvement compared to pure GO2 sample. Combining with EIS results, it was explained that a low amount of PVA induced a spacer effect on hybrid aerogels, facilitating the transport and the adsorption of electrolyte ions, and exposed more oxygen-containing functional groups, improving the contribution of both EDLC and the capacitance from surface faradic reactions. However, introducing an excess amount of PVA, over than 1.25 mg/mL, covers considerably GO nanosheets inducing a larger resistance, thereby they exhibit unsatisfactory electrochemical performance.

In the next decade, graphene will still find commercial applications in many fields, which require industrial-scale production of pristine graphene as liquid dispersion. Polymer as stabilizer can noncovalently attached to graphene surface preventing interlayers' stacking, thereby increasing graphene concentration. Such graphene exfoliated in the presence of a polymer represents an ideal starting material for composite preparation. To date, many studies have been reported on this strategy, however, the mechanism involved in the stabilization of graphene by polymer intermediates was for the first time exhaustively discussed in this thesis. The model of PVA adsorbed on graphene surface in chapter 3 can be easily extended to all types of 2D material/polymer/solvent systems if only physisorption happens on the absorbent. At the so-called critical concentration C_c, a high 2D material content in a low polymer concentration can be achieved, which is of interest for the fabrication of other 2D material/polymer composites to preserve 2D material's properties. Based on our model and theory, there is still a lot of room

for discussion and exploration. On the other hand, fully oxidized graphene destroys the structure of graphene, generally hindering its applications as conductive materials. Therefore, tailoring the oxygen content on graphene is important for graphene properties and dispersibility optimization. In chapter 4, only two kind of GO were prepared, which include 19.5% and 33.4% of oxygen. Finer tuning in the oxidation degree of graphene should be extended by modifying experimental conditions according to the literature, thus it is possibility to optimize the oxidation degree of graphene incorporating polymer to fabricate composites applied in specific fields. Finally, the hybrid aerogels containing a low amount of PVA have been well used as electrode material for electrochemical capacitor in chapter 5. However, for those containing a large amount of PVA, according to the literature, such porous graphene-based aerogels really have a great potential to be used as adsorption materials in the field of wastewater treatment.

Appendix

<u>Definitions of Terms and Symbol Used in the Text</u>

C_p	Polymer concentration
C_c	Critical concentration defined by us
C^*	Overlap concentration
C_s	Boundary concentration that divides the "dilute" solution into the "very dilute" solution
k	Boltzmann constant
T	Temperature
b	Length of Kuhn monomer (1.5 nm for PVA)
N	Number of Kuhn monomers of one coil
v	Excluded volume between two Kuhn monomers, and $v \approx b^3$
R_{end}	End-to-end distance of a polymer coil
$R_{//}$	Longitudinal size of adsorbed polymer chain
N^*	Number of adsorbed Kuhn monomers for partial adsorption chain
N_A	Avogadro constant
M	Molar weight of polymer
D	Thickness of the adsorbed part of polymer chain
$\delta_e kT$	Energy gain per Kuhn monomer on absorbent
δ_e	Adsorption energy parameter
χ	Flory-Huggins' polymer-solvent interaction parameter
χ_s	Polymer-surface interaction parameter
l	Length of one repeating unit
n	Number of repeating units in one Kuhn monomer
ΔF_{tot}	Free energy change of whole system during adsorption process
$F_{a, p}$	Free energy of adsorbed part
$F_{p, p}$	Free energy of protruding part
F	Free energy of the coil in free-standing state before adsorption
$[\eta]$	Intrinsic viscosity of polymer
$u_{pp,}$	Potential-energy for polymer-polymer contact
u_{ss}	Potential-energy for solvent-solvent contact
u_{ps}	Potential-energy for polymer-solvent contact

v_0 Solvent molecular volume, $v_0 = 30 \, Å^3$ for water

δ_d Dispersion solubility parameter

δ_p Polar solubility parameter

δ_h Hydrogen bonding solubility parameter

z Coordination number

C Specific capacitances

I Discharge current

Δt Discharge time

m Mass of electroactive materials

ΔV Total potential change

Abstract

In the past decades, graphene and graphene-based two-dimensional (2D) materials have received increasing interest for various applications such as energy storage, conductivity materials, catalytic reactions, biotechnology, *etc*. Liquid-phase exfoliation (LPE) is one of the most promising techniques at the industrial scale. The resulting nanosheets colloidal solution can be easily applied as a starting material to the preparation of nanocomposites. Commonly, graphene can be slightly dispersed in specific organic solvents which are generally harmful to environment and difficult to be removed. However, due to its hydrophobic behavior, it is hardly dispersed in water. To circumvent this issue, the polymer assisting LPE has been investigated within this thesis. Using a polymer, like PolyVinyle Alcohol, as stabilizer not only helps graphene dispersion but allows at the same time to get a wearable and biocompatible composite matrix. Here, it was aimed to optimize the graphene/ polymer ratio via polymer concentration control. Understanding the assistance mechanism paths the way for any other 2D material/ polymer/ solvent system application. Besides, the oxidation degree of the graphene is another important factor impacting on the graphene dispersibility in water media. The affinity between the polymer coils and the graphene oxide forms a 3D network, causing the gelation with the increasing polymer concentration. By using a freeze-drying process, the resulting graphene oxide/ polymer aerogel can be obtained that shows interesting properties to be used as electrochemical capacitor electrode.

Key words: graphene, graphene oxide, polymer, liquid-phase exfoliation, nanocomposite

Résumé

Au cours des dernières décennies, le graphène et ses dérivés, en tant que matériaux 2D, ont suscité un intérêt croissant pour diverses applications telles que le stockage de l'énergie, la catalyse, l'électronique ou encore la biotechnologie. Les solutions colloïdales de graphène exfolié représentent des « précurseurs » de premier choix pour la préparation de nanocomposites à base de graphène. L'exfoliation en phase liquide (LPE) reste l'une des techniques les plus prometteuses à l'échelle industrielle pour la production de telles solutions. Cependant, le caractère hydrophobe du graphène ne permet pas une exfoliation en solvant aqueux et ce n'est qu'en présence de solvants organiques, potentiellement nocifs et difficiles à éliminer qu'on arrive actuellement à le disperser en faible concentration. Pour contourner ce problème, nous avons étudié dans cette thèse un procédé d'exfoliation en phase liquide assisté par la présence d'un polymère, l'alcool polyvinylique (PVA). Le PVA utilisé comme stabilisateur, aide non seulement à la dispersion du graphène mais permet, dans le même temps, d'obtenir un matériau nanocomposite. Afin d'optimiser le rapport graphène/polymère et obtenir une dispersion fortement chargée en graphène il a été mené une étude sur la compréhension du mécanisme d'adsorption du polymère sur ces feuillets. Les résultats fondamentaux présentés en fonction de la concentration en polymère, permettent d'envisager la synthèse et l'utilisation de tout autre système matériau 2D / polymère/ solvant. Par la suite, le degré d'oxydation du graphène étant un autre facteur d'importance, son impact sur la dispersabilité du graphène dans l'eau a été étudié. L'affinité accrue des chaines polymères pour le graphène oxydé provoque la gélification du réseau 3D avec l'augmentation de la concentration en polymère. Enfin, au moyen d'un procédé de lyophilisation, la préparation de plusieurs aérogels graphène oxydé/polymère ont été élaborés et il a été montré l'intérêt de ces matériaux comme électrode de supercondensateur.

Mots clés : graphène, graphène oxydé, polymère, L'exfoliation en phase liquide, nanocomposite